Long Wavelength InGaAsP/InP Lasers and Optoelectronic Integration

Thesis by

Paul Kit-Lai Yu

In Partial Fulfillment of the Requirements

for the degree of

Doctor of Philosophy

California Institute of Technology

Pasadena, California

1984

(Submitted June 17, 1983)

ACKNOWLEDGMENTS

I like to express my deepest appreciation to my thesis advisor Prof. Amnon Yariv, for his support and encouragement throughout my graduate studies at Caltech. His ingenious insights and unlimited patience are most helpful to me. His image of a good teacher will stay with me throughout my life.

I am also indebted to both Dr. Shlomo Margalit and Dr. Pei Chuang Chen for their very helpful suggestions and ideas. I would like to thank Dr. Nadav Bar-Chaim, Dr. Uziel Koren, and Dr. TiRong Chen for their help and collaboration at different stages of my graduate studies. I am also thankful to Dr. Liew Chuang Chiu, Dr. Abraham Hasson, Dr. Eli Kapon and Dr. Kam Yin Lau in participating in some of the work described in this thesis. I would like to thank Dr. Joseph Katz for helpful suggestions and for his generosity in making available his finite element programs. In addition, I thank the other members of the group, past and present, for enlightening discussions. In particular, I appreciate the encouragement and company of my colleaques: Dr. Henry Blauvelt, Dr. Christoph Harder, Mr. Chris Lindsey, Mr. Steve Smith and Mr. Kerry Vahala. I am especially indebted to Mr. Desmond Armstrong for his skill in overcoming technical difficulties, Mrs. Jana Mercado for her kind assistance and friendship and Dr. Berken Chang for reading the early drafts of this thesis.

I am thankful for the financial support received from the California Institute of Technology, the National Science Foundation and the Office of Naval Research.

ABSTRACT

The light sources for optical communications in the 1.3-1.5 μm range are the quaternary InGaAsP/InP lasers which emit in this low loss region of optical fibers. The structure and properties of some lasers fabricated in this material system as well as their integration into optoelectronics are treated in this thesis.

Lasers exhibiting low threshold, high power and stable far field are extremely desirable in communication systems. Selective epitaxial growth offers an elegant yet powerful technique of fabricating laser structures with these properties. Its application to, as well as properties of, the resulting laser structures are presented. In particular, a laser with high output power is demonstrated.

To further extend the operating power of index guided laser diodes in a stable fundamental mode, gain stabilization is proposed as an effective means of discriminating against higher order transverse mode operation. The optimal design for gain stabilized fundamental mode operation is formulated theoretically and verified experimentally.

Precipitous increase of threshold current with temperature has been observed in some InGaAsP/InP lasers. Electron leakage over the heterobarrier has been identified as the cause of this abnormality. The origin as well as the control of these leaked carriers is studied.

Advances in optoelectronic integration consisting of diffraction coupled arrays and the demonstration of Laser-MISFET devices and the technique of microcleaved mirrors are described in detail.

The microcleavage technique is applied to the fabrication of very short cavity lasers. The advantages of short cavities are presented.

CONTENTS

Page

Chapter 1 : Introduction 1

1.1 Introduction 1

1.2 Outline of the thesis 4

Chapter 2 : Low threshold InGaAsP/InP Lasers fabricated using Selective Epitaxy 7

2.1 Introduction 7

2.2 Selective epitaxy 11

2.3 Embedded Laser on n-InP 13

2.3a Fabrication 13

2.3b Characteristics 15

2.4 Groove Laser on semi-insulating InP 18

2.4a Fabrication 18

2.4b Characteristics 22

2.4c Waveguiding in the Groove Laser 23

2.5 Terrace Laser 27

2.5a Fabrication 27

2.5b Characteristics 30

2.5c Large optical cavity Terrace Lasers 30

2.6 Conclusion 32

Appendix 2-1 : Perturbative effective index Method in waveguide analysis 36

Chapter 3 : Mode stabilization mechanism of Buried-waveguide lasers with Lateral Diffused Junctions. 45

3.1 Introduction 45

3.2 Lasers with lateral diffused junction--Theory 46

3.2a Boundary conditions 48

3.2b Analytical solution to the buried waveguide with lateral junction 50

3.2c Results and discussion 51

3.3 Lasers with lateral diffused junction--Experiment I 62

3.3a Groove TJS Lasers 62

3.3b Comparison with theory 66

3.4 Lasers with lateral diffused junction--Experiment II 66

3.4a Terrace TJS Lasers 66

3.5 Conclusion 72

Appendix 3-1 : Computational scheme solving steady state rate equations with known mode profiles 73

Appendix 3-2 : Validity of the real-index guiding assumption 75

Chapter 4 : Carrier Leakage and Temperature Dependence of InGaAsP Laser threshold current 78

4.1 Introduction 78

4.2 Experimental measurement of carrier leakage 79

4.2a The laser-bipolar-transistor structure for leakage measurement 79

4.2b Electron leakage measurement 81

4.2c Temperature behavior of electron leakage 84

4.2d Hole leakage measurement 88

4.3 Carrier leakage in Heterojunction -- Theory 88

4.3a Field enhanced electron leakage 91

4.3b Hot carrier induced leakage 96

4.4 P-doping effect on leakage -- Experimental studies 100

4.4a Experiment I 100

4.4b Experiment II 103

4.4c Application to high T_o lasers 103

4.5 Conclusion 103

Appendix 4-1 : Hole injection across a heterobarrier 105

Chapter 5 : Optoelectronic Integration in InGaAsP/InP system 110

5.1 Introduction 110

5.2 Integration of a Groove Laser with InP MISFET 111

5.2a Fabrication 111

5.2b Characteristics 112

5.3 Microcleaved mirrors for integration 116

5.3a Fabrication 118

5.4 Integrated phase-locked laser array 122

5.4a Fabrication 125

5.4b Diffraction coupling in phased array 125

5.4c Characteristics 126

Appendix 5-1 : Diffraction coupling in laser array 129

Chapter 6 : Short Cavity InGaAsP/InP Lasers 134

6.1 Introduction 134

6.2 Longitudinal mode selection 134

6.3 High frequency designs 135

6.4 Short cavity lasers with coated mirrors 140

6.5 Conclusion 140

Appendix 6-1 : Small signal analysis of rate equations 144

Chapter 1

Introduction

1.1 Introduction

Semiconductor materials such as $Al_xGa_{1-x}As$ on GaAs and $In_xGa_{1-x}As_yP_{1-y}$ on InP are chosen in high data-rate optical communication systems because their direct bandgap and good quality heterojunctions permit the fabrication of high speed optical and microwave devices. Communication systems based on these semiconductor components can thus interface purely electronic media with analog microwave systems. Monolithic designs in which electrical and optical devices are integrated fall under the general classification of integrated optoelectronic circuits (IOECs). This integration was first suggested by Yariv [1]. A block diagram (figure 1.1) of an IOEC shows three sections: a detector section, an electronic processing section, and a transmission section. This IOEC has been first demonstrated in the GaAlAs-GaAs material system due to the early recognition of GaAs for lasers and devices fabrication. However, InP devices such as field effect transistors (FETs) are also potentially important in the microwave region because InP has a peak electron velocity which is higher than that of GaAs [2]. Moreover, since present GeO_2 doped silica fibers have low loss (figure 1.2) in the 1.2-1.6 μm range [3-6], quaternary lasers (1.0-1.7 μm) have become prime candidates in optical communication systems. Compared with the well developed AlGaAs/GaAs system, the quaternary system is less affected by oxygen during growth and the laser facets are more resistant to oxidation. Current data also suggest that the life-expectancy of quaternary lasers is expected to be longer than that of GaAs lasers. For these reasons, extensive efforts have begun to focus on the technological advancement of devices based on the InGaAsP-InP material system.

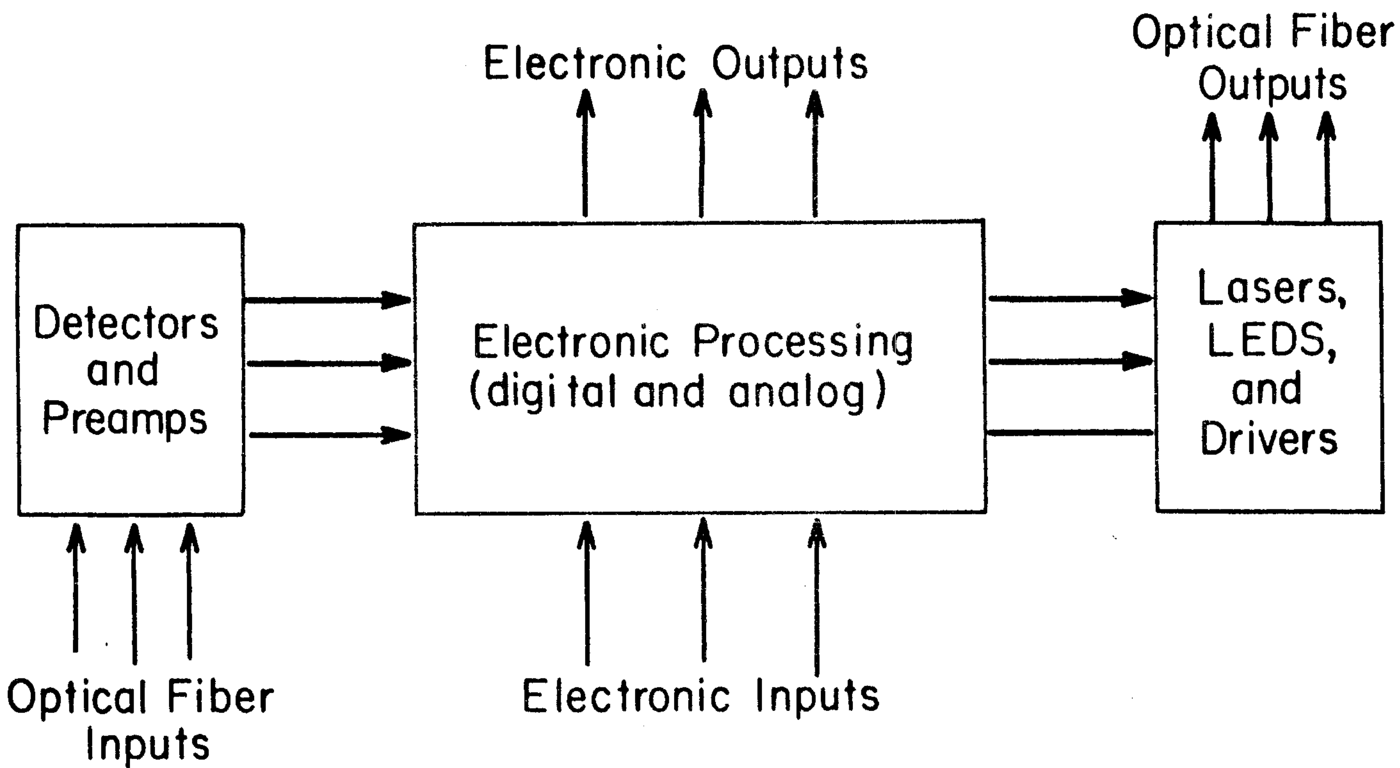

Fig. 1.1 A block diagram of an integrated optoelectronic circuit (IOEC).

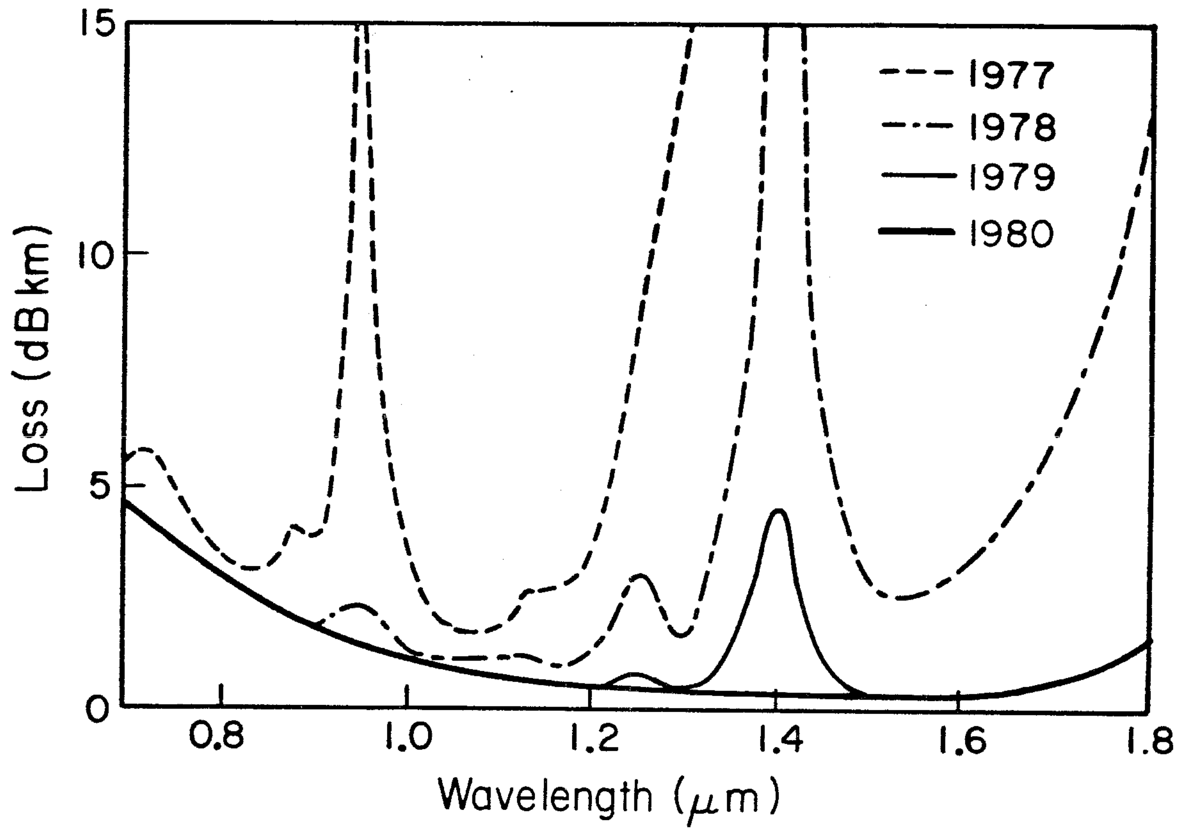

Fig. 1.2 Loss spectrum of a graded index fiber. The thick solid line (1980) shows an almost horizontal spectrum around 1.2-1.6 μm.

1.2 Outline of the thesis

Throughout this thesis, a familiarity with both semiconductor devices and double heterostructure lasers is assumed.

Five subjects in the field of quaternary InGaAsP/InP lasers will be presented. Chapter 2 begins with the discussion of selective epitaxy and its advantages in laser fabrication and optoelectronic integration. These advantages include the simplicity of fabrication steps as well as the use of heteroepitaxy to achieve lateral carrier and modal confinement. Three laser structures -- the Embedded Laser, the Groove Laser and the Terrace Laser -- fabricated with this method are described. The Embedded Lasers are fabricated on n-InP while the other two lasers are fabricated on semi-insulating InP substrates. The fabrication and the performance of each of these devices are described.

Chapter 3 consists of an analysis of the buried waveguide with lateral p-n junction. Mode stabilization of this waveguide is studied both experimentally and theoretically. The theory predicts an optimal design for gain stabilized fundamental mode operation and this is compared experimentally in both the Groove Transverse Junction Stripe (TJS) Lasers and Terrace Transverse Junction Stripe Lasers. Of particular interest is the relatively simple computational scheme for incorporating the injection current profiles, the waveguide shapes and the boundary conditions in the solution of the rate equation.

Chapter 4 is concerned with current leakage across InGaAsP-InP heterojunction. An experiment is devised to measure directly the electron and hole leakage in a laser using a novel lasing-bipolar-transistor structure. A model incorporating current continuity equations, transport equations and the heterojunction injection is described. The nature of the field enhanced leakage is studied theoretically and verified experimentally. The study suggests adding a low

p-doped buffer layer in a conventional laser structure to decrease the temperature sensitivity. This is verified experimentally.

Chapter 5 is concerned with opto-electronic integration in the InGaAsP/InP system. The first InP laser-MISFET integrated circuits and the first InGaAsP/InP micro-cleaved laser are described. The useful features of micro-cleavage in opto-electronic integration are discussed. The first integrated InGaAsP laser phased array is presented.

In chapter 6, the microcleavage technique is applied to obtain short cavity lasers. The advantages of stable single longitudinal mode operation and high frequency capability of the resulting short cavity lasers are analysed and noted.

References

1. A. Yariv, "Active integrated optics," in Proc. of 1971 Esfahan Conference on Pure and Applied Physics. Cambridge, MA. MIT Press (1972).

2. Especially since the introduction of a large InP cover wafer to provide sufficient phosporus overpressure thereby solving the problem of substrate decomposition at high temperature; see G. A. Antypas, Appl. Phys. Lett., vol 37, 64 (1975).

3. D. B. Keck, R. D. Manrer, and P. C. Schultz, Appl. Phys. Lett., vol 22, 307 (1978).

4. T. Miya, Y. Terunuma, T. Hosaka, and T. Miyashita, Electron. Lett., vol 15, 106 (1979).

5. D. Marcuse, Appl. Optics, vol 19, 1653 (1980).

6. Koichi Inada, IEEE Trans. Microwave Theory and Tech. vol MTT-30, pp. 1412 (1982).

Chapter 2

Low threshold InGaAsP/InP Lasers fabricated using Selective Epitaxy

2.1 Introduction

In the design of low threshold semiconductor lasers, an essential consideration is the confinement of both the injected carriers and the optical modes. For a given laser structure operating at a certain injection level, the condition of carrier confinement requires that carrier injection occur mainly in the active region with negligible leakage into the surrounding regions. A fraction of the injected carriers recombine radiatively in pairs (electrons with holes) during the stimulated emission process providing the optical gain. The condition of optical mode confinement demands that guided modes of the laser do not spread extensively into regions where no gain exists since that portion of the mode outside the gain region does not enjoy amplification. By optimizing both carrier and optical mode confinement, lasers with good performance can be obtained.

The condition of optical confinement can be easily met in laser cavities where the active region is surrounded by dielectrics with smaller refractive indices. The degree of optical confinement for a given optical mode, usually represented by the factor Γ (defined as the fraction of energy of the optical mode within the active region), is a function of the dielectric constant difference between the active and the surrounding region and of the active region thickness. An increase in the refractive index difference and/or the thickness leads to better confinement and thus larger Γ [1]. Thicker active layers, however, require more current to achieve the transparency condition [2] and thus threshold. Therefore an optimal thickness giving the lowest threshold current exists. For the InGaAsP/InP system, this thickness has been found to be around 0.1-0.2 μm.

The condition of electrical confinement is more complicated. In practice, good electical confinement has been achieved with a double heterostructure (DH) in which the active region is sandwiched between materials with larger energy bandgaps. It is generally believed [2,3] that potential barriers formed at the heterointerfaces will prevent leakage of injected carriers from the active region. In the quaternary system, this is accomplished by the cladding layers of InP which have a larger bandgap (see figure 2.1) than InGaAsP. In spite of this, we have found evidence of a considerable amount of leakage current over the InGaAsP-InP heterobarrier. This is the subject of discussion in chapter 4.

Among the various designs of semiconductor lasers, the buried heterostructure (BH) stands out for its ability to achieve both optical and carrier confinement [4]. Among the several ways to achieve buried waveguide structure, the most straightforward way is to employ two-step liquid phase epitaxial growths (see figure 2.2) where the particular shape of the active region can be formed by etching after the first epitaxial step. The sides of the active region are "buried" in larger bandgap materials during the second epitaxy. However, such processing introduces complications. As grown layers undergo prolonged periods of high temperature treatment, undesirable circumstances such as dopant diffusion and substrate thermal damage will emerge. Also, the complicated processing leads to a low yield of these lasers. Selective epitaxy offers an elegant yet powerful alternative to the above growth processes of BH lasers. Similar growth techniques can also be applied to other laser designs.

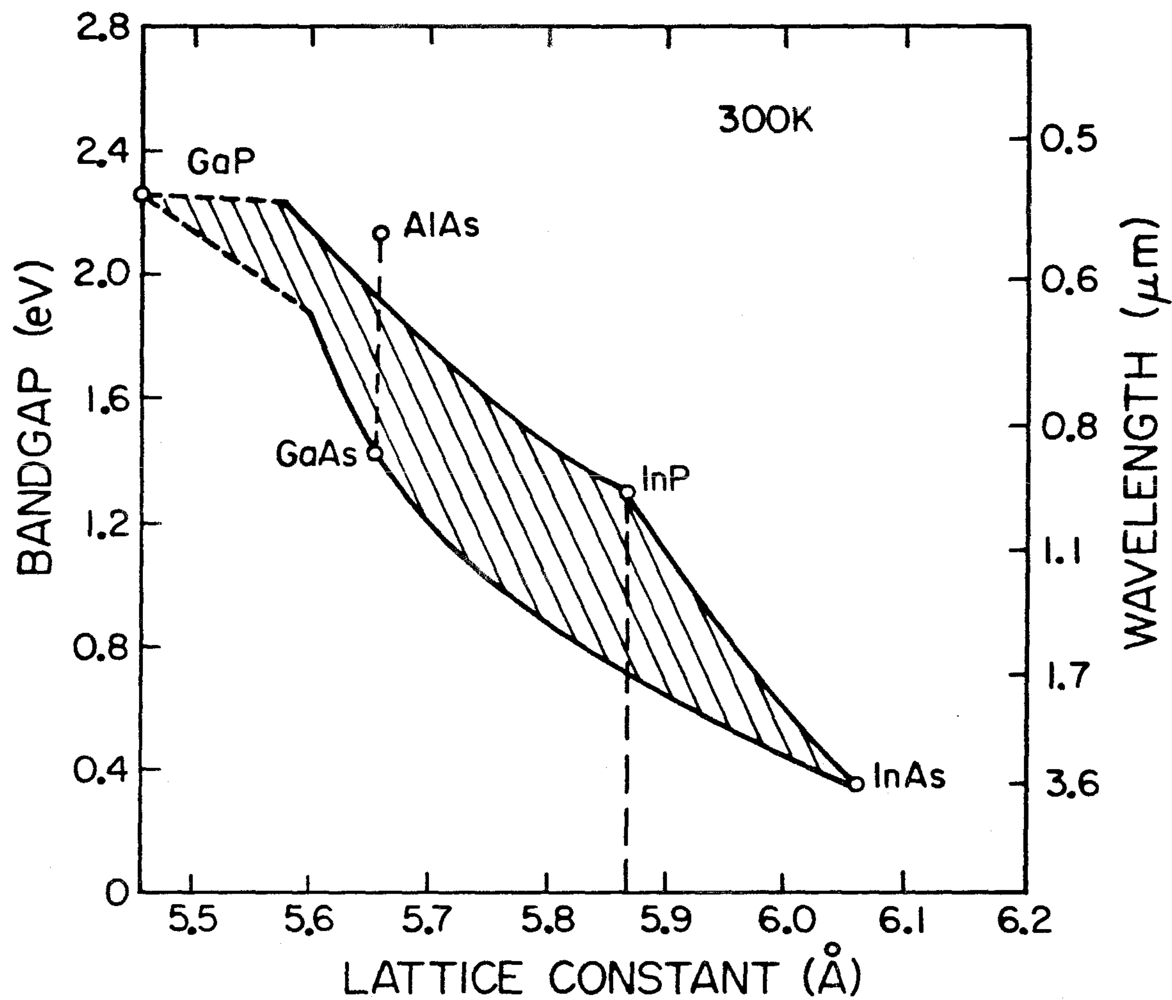

Fig. 2.1 Bandgap vs lattice-constant plot of the quaternary InGaAsP material system.

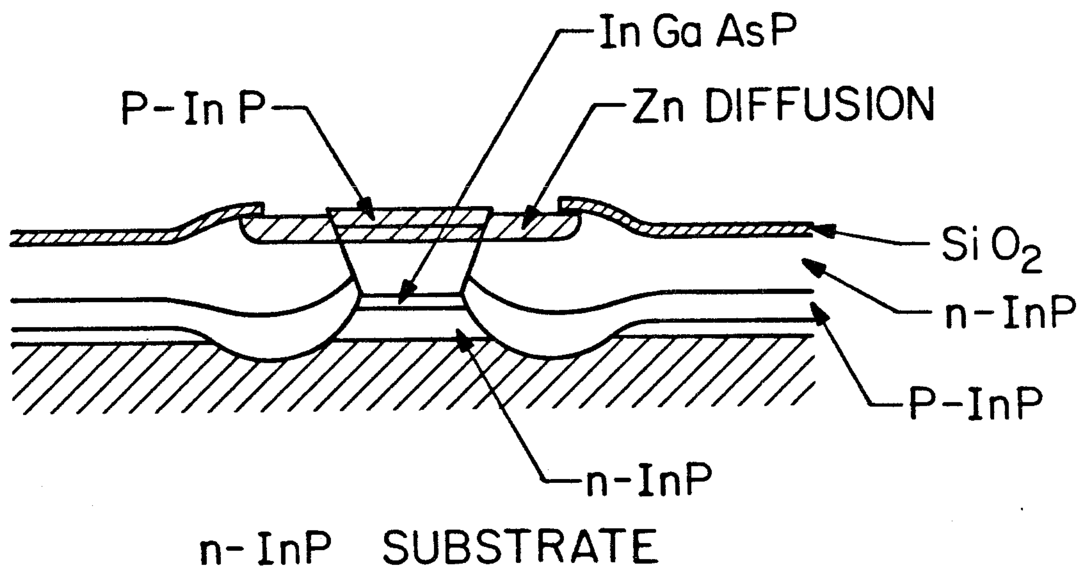

Fig. 2.2 A schematic diagram of a InGaAsP/InP Buried-Heterostructure Laser on conductive substrate.

2.2 Selective epitaxy

Selective epitaxy, as its name suggests, is a technique whereby the growth of epitaxial layers is restricted exclusively to certain portions of the wafer. An important advantage of this growth technique is that confined active regions can be formed automatically as a result of the growth. This advantage is exploited in the structures to be described in sections 2.3, 2.4 and 2.5. An equally significant advantage of this technique is that, for some laser structures, the usual two step LPE growth process can be accomplished by a single epitaxial step.

The method is usually first effected with the deposition of a layer of dielectric, such as silicon dioxide or silicon nitride, over the entire wafer [5,6]. Subsequently the dielectric is patterned by photolithography to form a growth mask on the wafer. Over the part where the layer of the dielectric remains, no growth can take place during the liquid phase epitaxy. However, on the unmasked portions, growth can proceed in various ways depending on the boundary orientation. If, for instance, stripe openings are made in the [011] direction on a (100) InP substrate, the layers are grown as shown in figure 2.3a (cross section view). If, instead, the stripes are made in the orthogonal $[01\bar{1}]$ direction, the layers are grown as shown in figure 2.3b.

Selective epitaxy will, furthermore, ease the achievement of the monolithic integration of lasers with other electronic devices. By selectively growing InP and quaternary layers on the semi-insulating InP, we can obtain spatially and electrically isolated devices on the same wafer. This feature is further exploited in the monolithic integration of a laser and metal-insulator semiconductor field effect transistor [7] to be presented in detail in chapter 5.

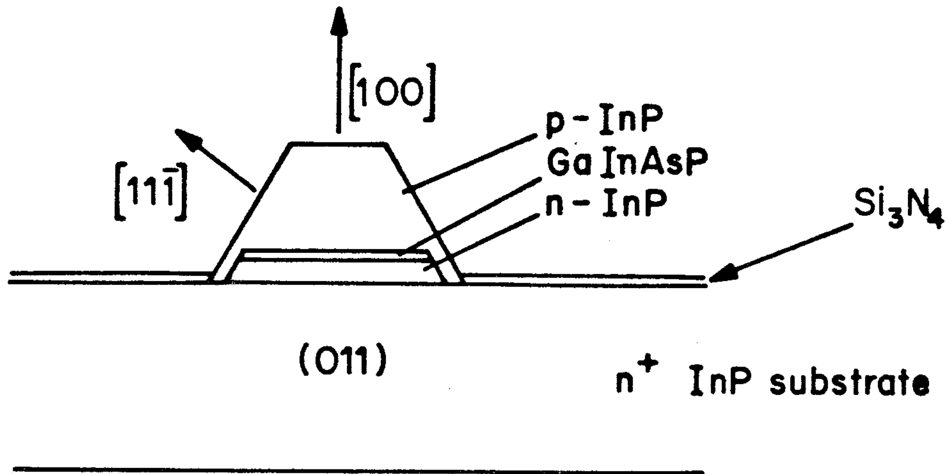

Fig. 2.3a Growth of a DH structure on a stripe opening along [011] direction.

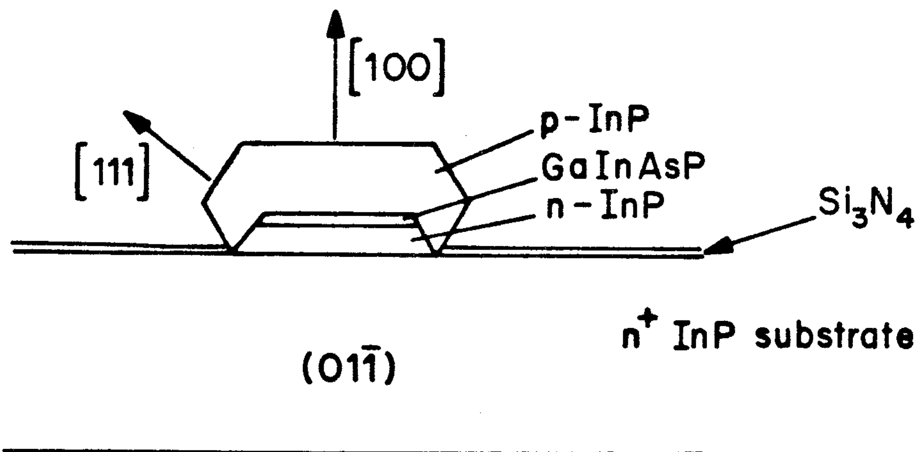

Fig. 2.3b Growth of a DH structure on a stripe opening along [01$\bar{1}$] direction.

2.3 Embedded Laser on n-InP

2.3a Fabrication

We first applied the technique of selective epitaxy in the fabrication of a low threshold laser on conductive n-InP substrate -- the Embedded Laser [8]. The processing of the lasers is described as follows (figure 2.4 summarizes the fabrication steps). First, the substrate is immersed in acetone to dissolve any organic compounds, such as wax, left from the polishing of the wafer. Then, a layer of silicon nitride is deposited on the wafer using chemical vapor deposition (CVD). With conventional photolithography, a pattern of silicon nitride double stripes, each 5-7 μm wide and with a 5-7 μm separation is left on the wafer. The substrate is then cleaned again before being loaded for epitaxy. All the layers are grown from two phase solutions. Two-phase means there always exists some excess, undissolved InP floating on the solution during the growth. With the usual cooling rate of $\sim 0.7°$ C/min, the deposition rate can be very high, especially on narrow stripe openings. Two methods are devised to slow down the growth rate so that the thickness of each layer can be controlled. One method is to make use of the redundant growth on the wide openings next to the silicon nitride double stripes (figure 2.4). Such growth will reduce the deposition rate in the central opening. The other method is to slow down the cooling rate to 0.1-0.2 °C/min so that there is little supersaturation inside the solution. The first method is used in the fabrication of the present laser while a combination of both methods is used in the growth of the Groove Laser (section 2.4).

The wafer is then loaded into the graphite boat. The boat is placed within a quartz tube which is flushed with palladium purified hydrogen gas. During the solution soaking time which usually lasts one hour, the furnace is heated up to 675 °C. Thus, in order to prevent the thermal decomposition of the InP wafer, a

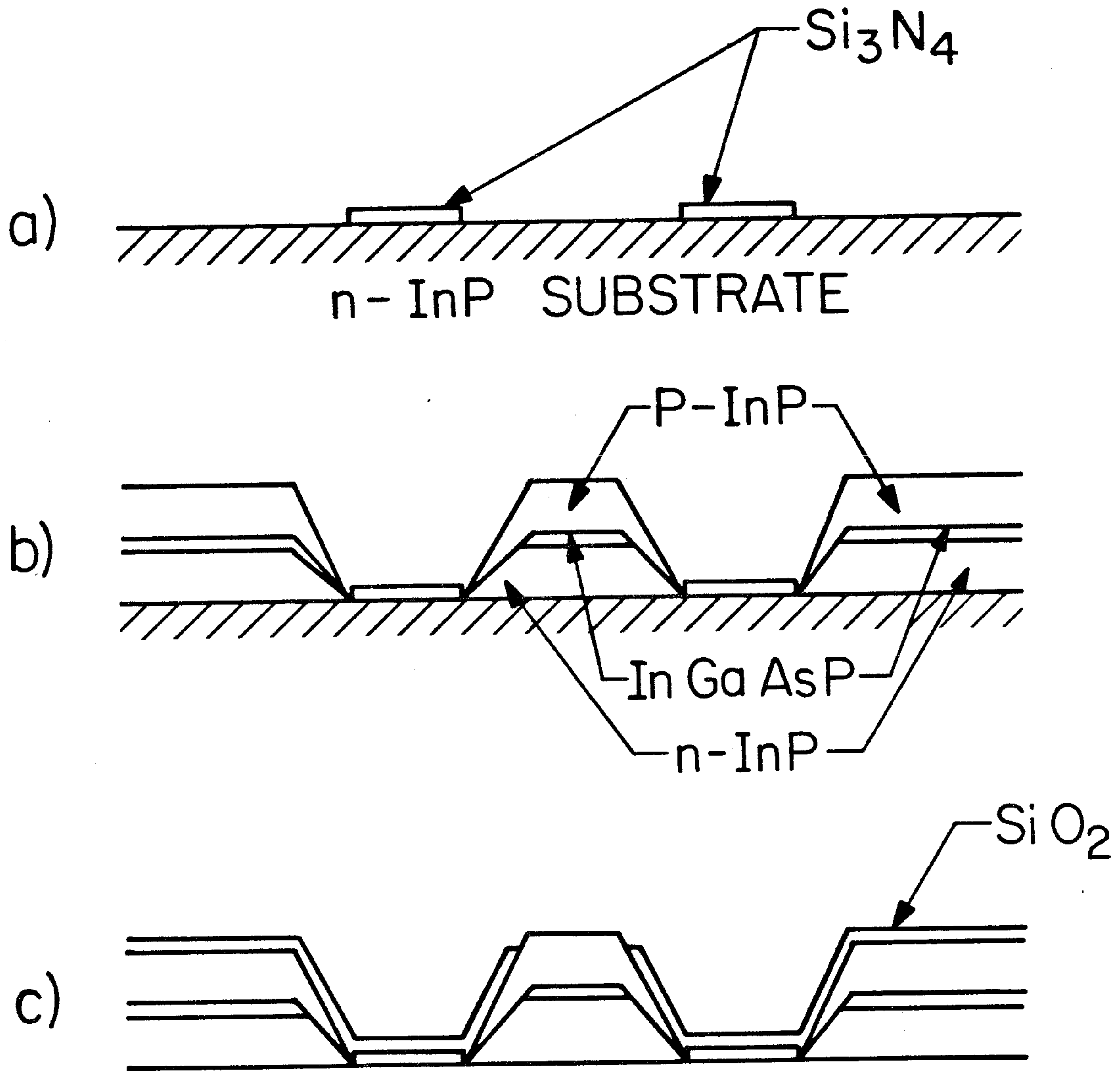

Fig. 2.4 Processing steps for an Embedded Laser.

cover wafer is used to cover the substrate to supply sufficient phosporus over-pressure [9]. Three epitaxial layers are grown: n-InP ($2\times10^{18}cm^{-3}$), InGaAsP(undoped), and p-InP ($\sim 1\times10^{18}cm^{-3}$). The p-InP layer is intentionally heavily doped so that good ohmic contact can easily be made on top of the mesa. Cross section views of the grown layers with stripe openings made along the [011] and [01$\bar{1}$] directions are shown in figures 2.3a and 2.3b respectively. We note that structures with stripes made in the [01$\bar{1}$] direction do not have the sides of quaternary layer embedded in the InP. Low threshold lasers are obtained for layers grown on [011] stripes.

After epitaxy, a layer of CVD silicon dioxide is deposited over the entire wafer and contact stripes are opened over the top of the laser mesa. A shallow Zn diffusion can be performed on the exposed surface to eliminate electrical short. AuZn/Au is evaporated on the top side and alloyed at 420 °C for 30 sec to 1 min. The wafer is lapped down to about 60-70 μm on the substrate side. Subsequently AuGe/Au is evaporated on the substrate side and alloyed at 280 °C. The wafer is then cleaved into bars of lasers for measurements.

2.3b Characteristics

For lasers with an active layer 3-5 μm wide, 0.2 μm thick and 250 μm long, the pulsed threshold current ranges between 50-70 mA with the lowest one being 45 mA. Typical light versus current characteristics are shown in figure 2.5 and a spectrum of the laser is shown in figure 2.6. When compared to oxide stripe lasers of similar width [10], this laser possesses lower threshold current and higher external quantum efficiency ($\sim$ 30-40 %). This is due to the superior carrier and modal confinement of this laser. A threshold current versus ambient temperature measurement (figure 2.7) of the laser shows the threshold current

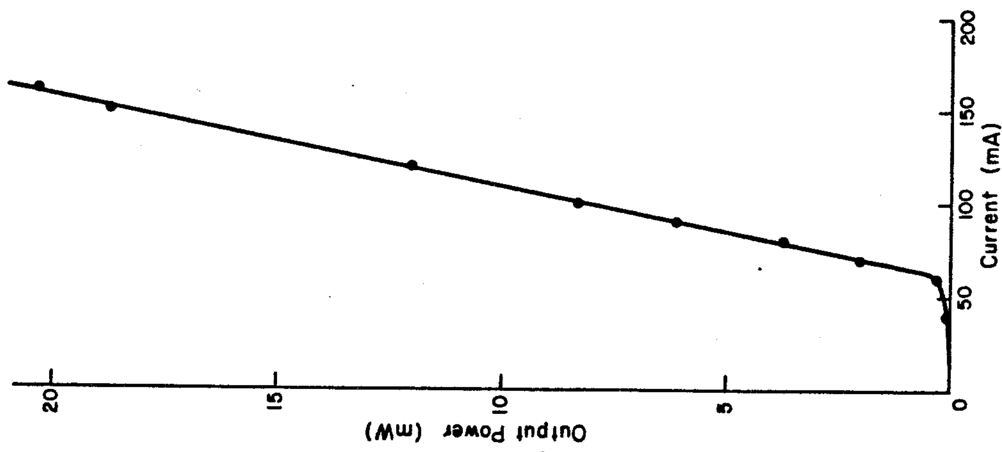

Fig. 2.5 L-I characteristics of an Embedded Laser.

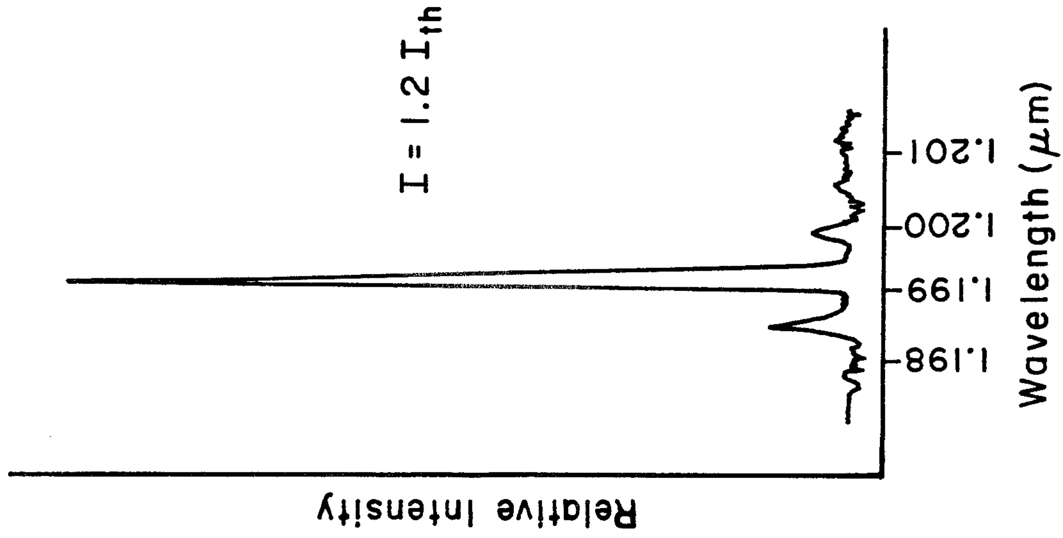

Fig. 2.6 Spectrum of an Embedded Laser.

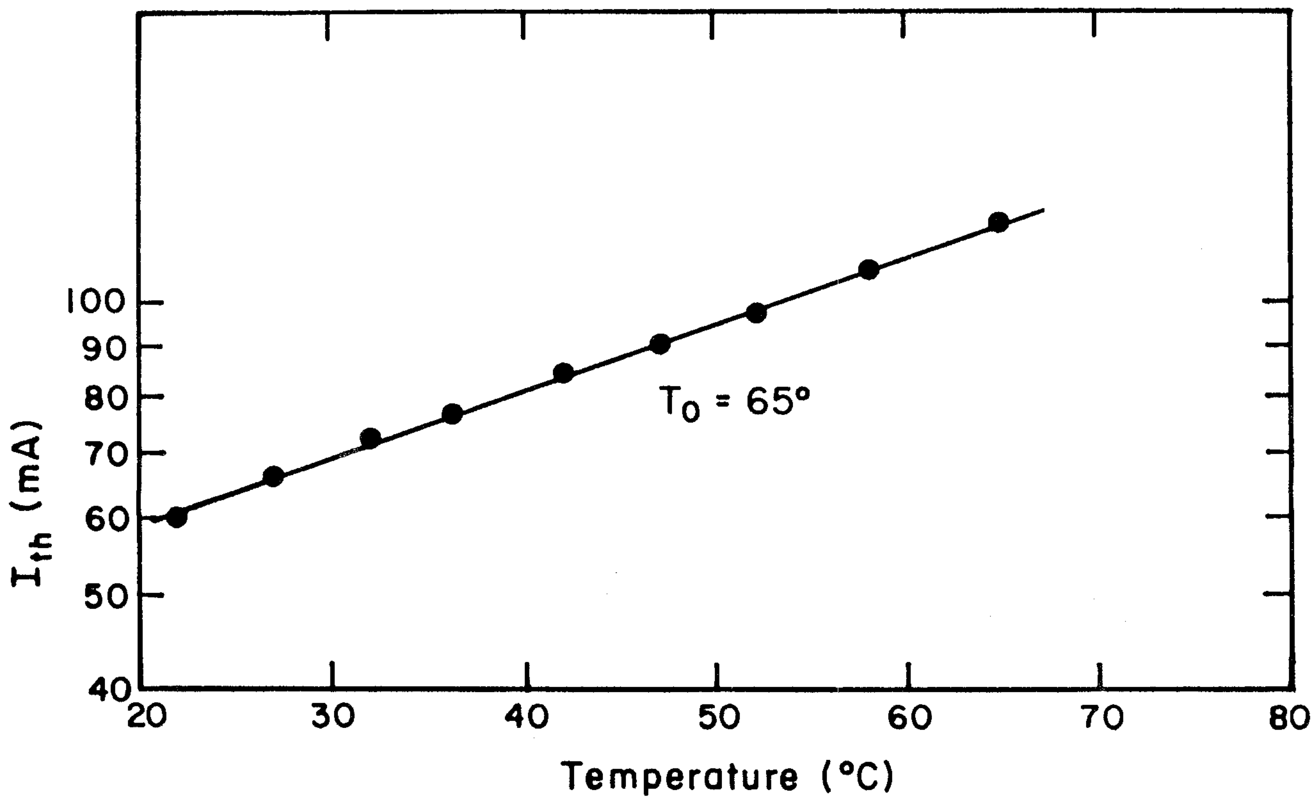

Fig. 2.7 Threshold current versus temperature plot for an Embedded Laser.

goes like ~ $\exp(T/T_0)$ with T_0 approximately 65°K.

2.4 Groove Laser on semi-insulating InP

For the purpose of optoelectronic integration, we are interested in developing simple, low threshold lasers on semi-insulating substrates. As is the case with lasers on conductive substrates, lasers with good electrical and optical confinement can be obtained with buried heterostructure (BH) on semi-insulating InP. We have developed the Groove Laser on semi-insulating InP [11] to minimize lateral current leakage, and to simplify the fabrication procedure. A schematic diagram of the laser is shown in figure 2.8. Instead of the n-p-n current blocking layers in conventional BH lasers (figure 2.2), we employ semi-insulating InP to provide the lateral current confinement. Due to the high specific resistivity(10^7 Ω-cm) of the semi-insulating InP, carrier injection can only appear across the p-InP/quaternary and the n-InP/quaternary heterojunctions and no sideway leakage flows via the semi-insulating InP. In comparison with BH lasers, this laser is simpler to fabricate since it requires only a one-step epitaxial growth. The active region is crescent shaped and it will be shown in section 2.4c that these crescent shaped waveguides provide good optical confinement. As a result, low threshold operation is obtained with this laser. Furthermore, the semi-insulating InP reduces the stray capacitance of the laser structure and this is important for high speed modulation [12].

2.4a Fabrication

The fabrication of the laser begins with the deposition of a CVD Si_3N_4 layer on semi-insulating InP. Subsequently, dovetail shaped groove channels are etched through CVD Si_3N_4 stripe openings. The stripes are made in the [011] direction

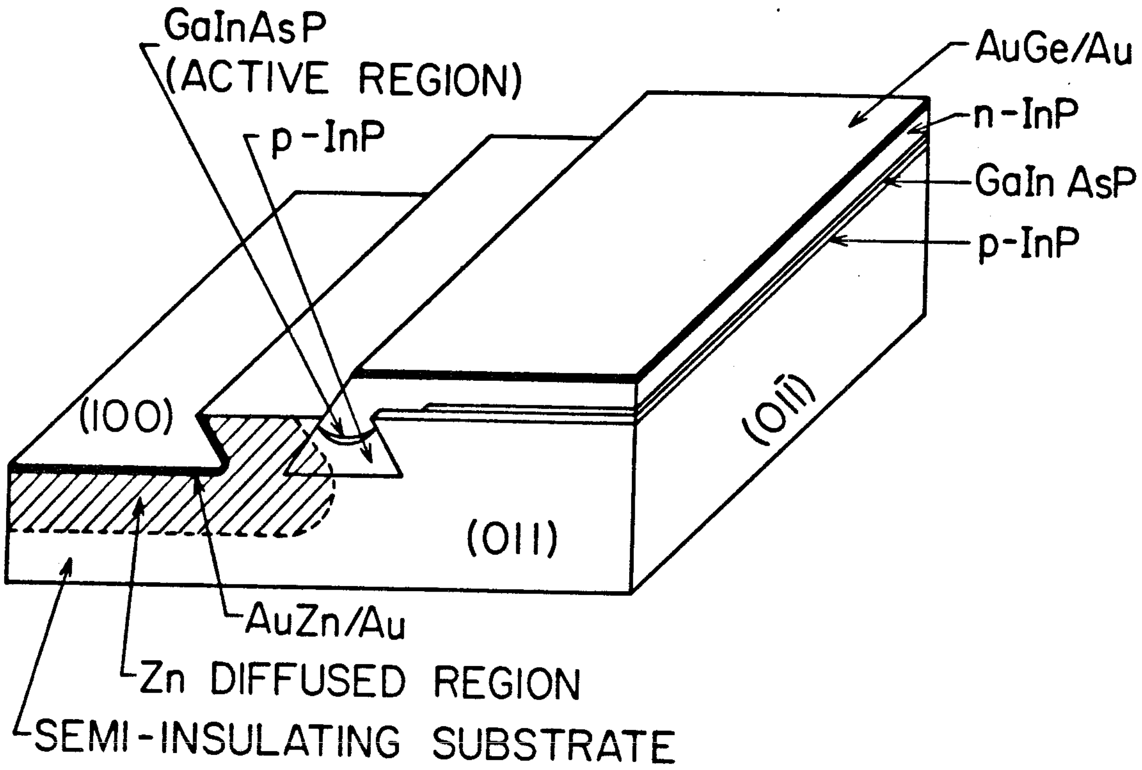

Fig. 2.8 A schematic diagram of a Groove Laser with lateral diffusion.

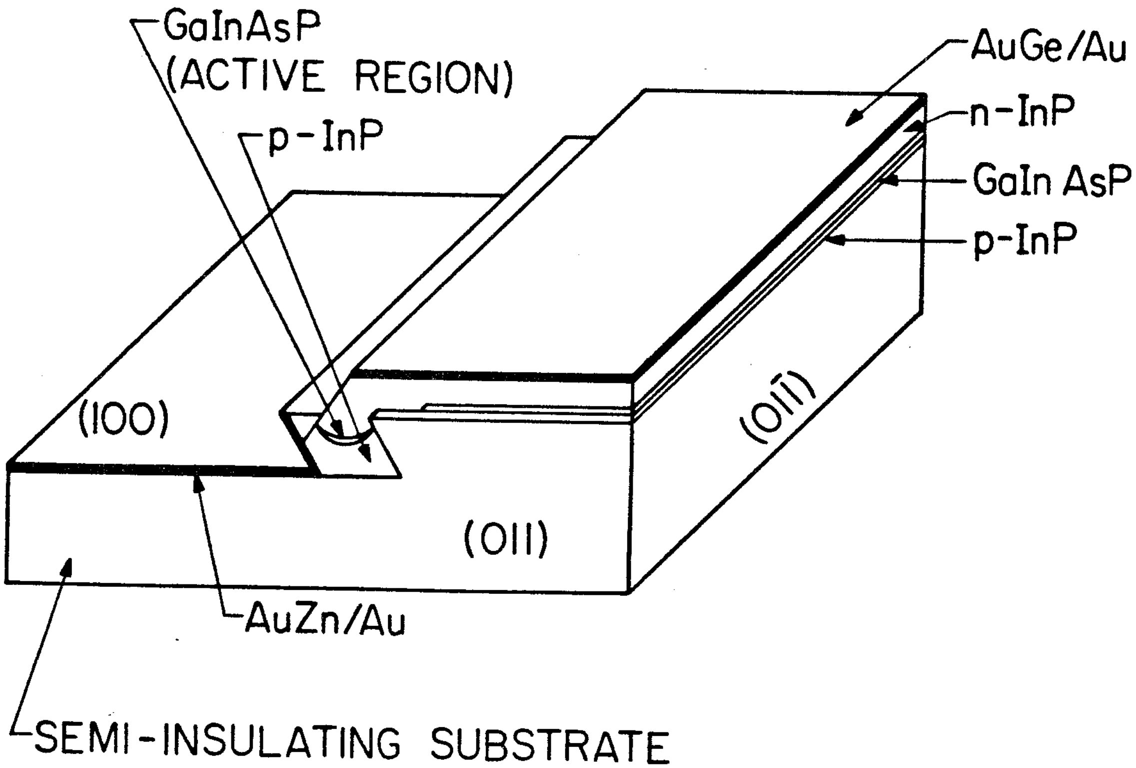

Fig. 2.9 A Groove Laser with etched side channel for p-contact.

and are 3.5 μm wide. The etchant, 10% aqueous solution of iodic acid, produces groove channels with smooth surfaces, an important feature required for good crystal growths. The etching rate is slow but reproducible (~1200Å /min at 22 °C). As some compounds such as iodine and indium iodate are formed during etching, it is necessary to rinse the wafer with dilute nitric acids and methanol to remove them.

As mentioned in section 2.2, the shape of the etched channels is direction dependent. For stripe openings made in [011] direction dovetail shape channels are obtained, while for those in the $[01\bar{1}]$ direction, V-groove channels are formed. We note that growth can proceed quite differently for different channel shapes (and thus wall orientations). Within the V shape channels, sometimes planar layers are grown, while at the other times growth only appears near the bottom of the channel with no growth on channel walls. Growth in the $[01\bar{1}]$ channels is therefore not as controllable as that in the [011] channels, which are thus preferred for the present laser.

After the etching of the dovetail shape groove channel, the Si_3N_4 is selectively removed from one side of the groove channel. The remaining Si_3N_4 on the other side acts as a growth mask. The wafer is further cleaned with oxygen plasma and is finally immersed in a solution of H_2SO_4, H_2O_2, and H_2O (3:1:1) for several minutes before being loaded for growth. Growth can take place within the channels as well as on the surface where the silicon nitride has been removed. This bare surface serves two different purposes: firstly, it slows down the channel growth rates, especially the quaternary growth rate; secondly, it can be used for the fabrication of other devices such as FET's. Three LPE layers are grown on the wafer: p-InP ($2-4\times10^{17}cm^{-3}$ Zn doped), InGaAsP (undoped), and n-InP ($2\times10^{18}cm^{-3}$ Sn doped). An SEM cross-section of layers grown inside a dovetail channel is shown in figure 2.10. The first layer is grown from a solution with 5 °C

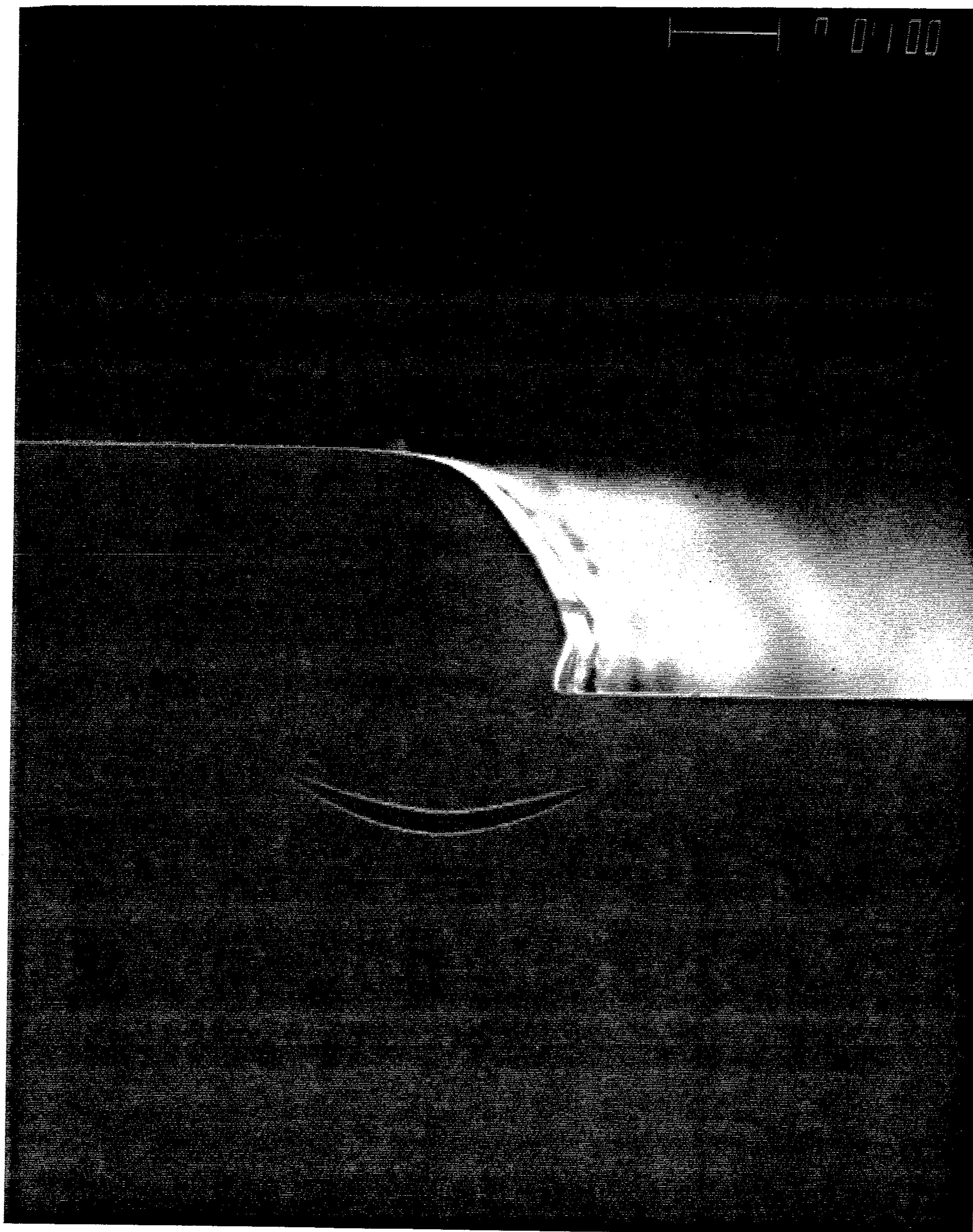

Fig. 2.10 An SEM view of a Groove Laser after LPE growth. The scale is 1 μm.

supersaturation which promotes the growth. The active layer and the third layer are grown from two-phase solutions. The quaternary layer is grown at 635 °C. The cooling rate is 0.1–0.2 °C/min throughout the growth of the first two layers and is rapidly increased to 1 °C/min during the last layer growth. The first layer growth is critical since it determines the width and the curvature of the active layer (and thus its height above the bottom of the etch channel); both are important parameters for optimizing the optical confinement of the resulting waveguide.

There are two methods to make p-contact to the p-InP layer within the groove which is still surrounded by semi-insulating InP. The first method employs a lateral Zn diffusion to touch the p-InP. Following the LPE, a new Si_3N_4 layer is deposited and wide stripes are opened (see figure 2.8). The exposed InP is etched with a 0.5% solution of Br_2 (in methanol), until one channel wall is about 3-4 μm from the p-InP. Subsequently Zn is diffused laterally to reach the p-InP. The p-contact is completed with AuZn/Au evaporated and photolithographically defined on the wide, etched channel. In the second method, a new Si_3N_4 layer is again deposited after LPE, and stripes are opened and etched until one side of the p-InP inside the groove is exposed laterally [13] (figure 2.9). AuZn/Au is directly evaporated onto this part to form a p-contact. The other contact on the n-InP is made by an AuGe/Au evaporation and this contact is separated from the p-contact by employing the standard lift-off technique.

2.4b Characteristics

For lasers with an active layer 3.5 μm wide and 0.3 μm thick (at the center of the crescent), threshold current ranges from 20 to 40 mA with the lowest pulsed threshold being 17 mA. Typical light current characteristics of the laser are

shown in figures 2.11,2.12. The characteristics for pulsed operation are linear up to five times the threshold current. CW operation is achieved with lasers mounted with substrate side down on gold plated copper block and threshold current is typically about 20% higher than that for pulsed operation. The external differential quantum efficiency for both facets is 40%. Single longitudinal mode is observed at up to 1.3 threshold current and multi-modes appear at higher currents. The emission wavelength of the lasers is 1.2 or 1.3 μm depending on the active layer composition. The threshold current versus temperature characteristics of a laser shows a T_0 (see figure 2.13) of ~72°C around room temperature. The external differential efficiency of the same laser (figure 2.14) drops as the ambient temperature is increased and this is related to the carrier leakage over the heterobarrier (details to be discussed in chapter 4).

2.4c Waveguiding in the Groove Laser

In Appendix 2.1, a perturbative effective index method is described to treat the waveguides with slow lateral index variation. We apply the results to a Groove Laser with an active region width w and approximate the active region thickness t(y) by a parabola :

$$t(y) = t_o(1 - \frac{4y^2}{w^2}) \qquad -w/2 < y < w/2 \tag{1}$$

where t_o is the thickness at center (y=0) of the waveguide. Equation 1 gives, according to equation A-17 (Appendix 2-1), the following effective lateral index profile :

$$n_{eff}^2(y) = n_{eff}^2(0) - 8(n_2^2 - n_{eff}^2(0))\frac{t_o}{t_{eff}(0)w^2}y^2 \tag{2}$$

This index profile indicates increasing negative index values outside the active region, while the actual effective index should be constant for $|y| \geq w/2$

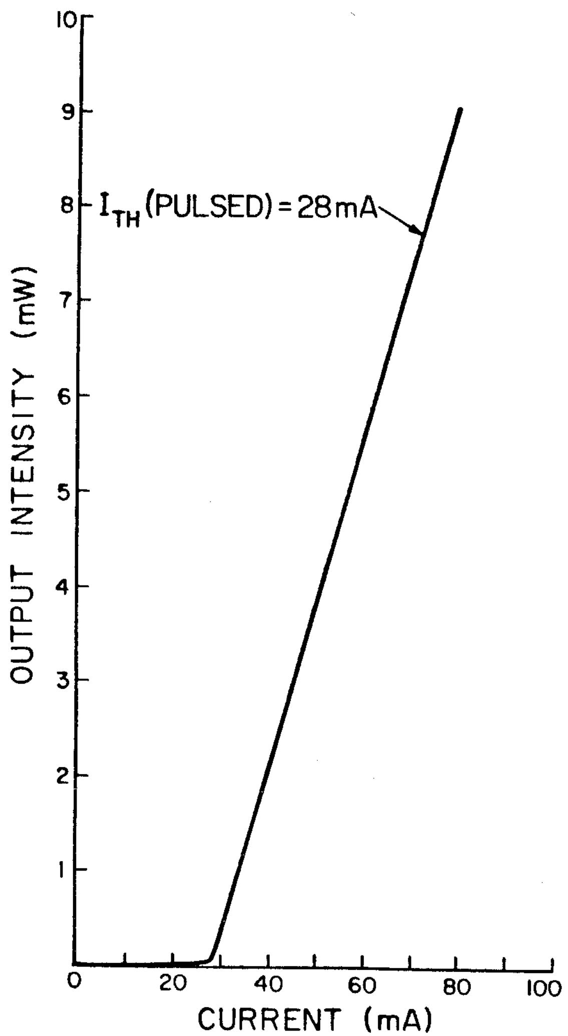

Fig. 2.11 L-I characteristics of a Groove Laser at pulsed operation.

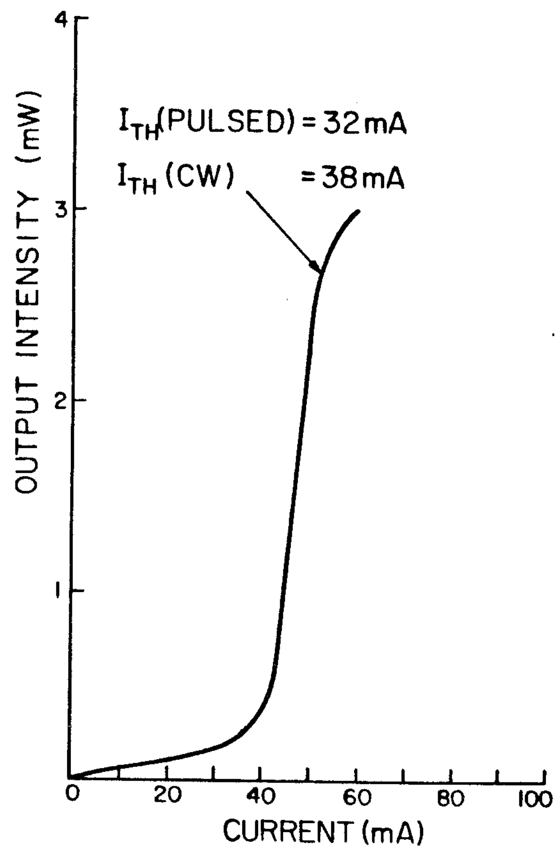

Fig. 2.12 L-I characteristics of a Groove Laser at CW operation.

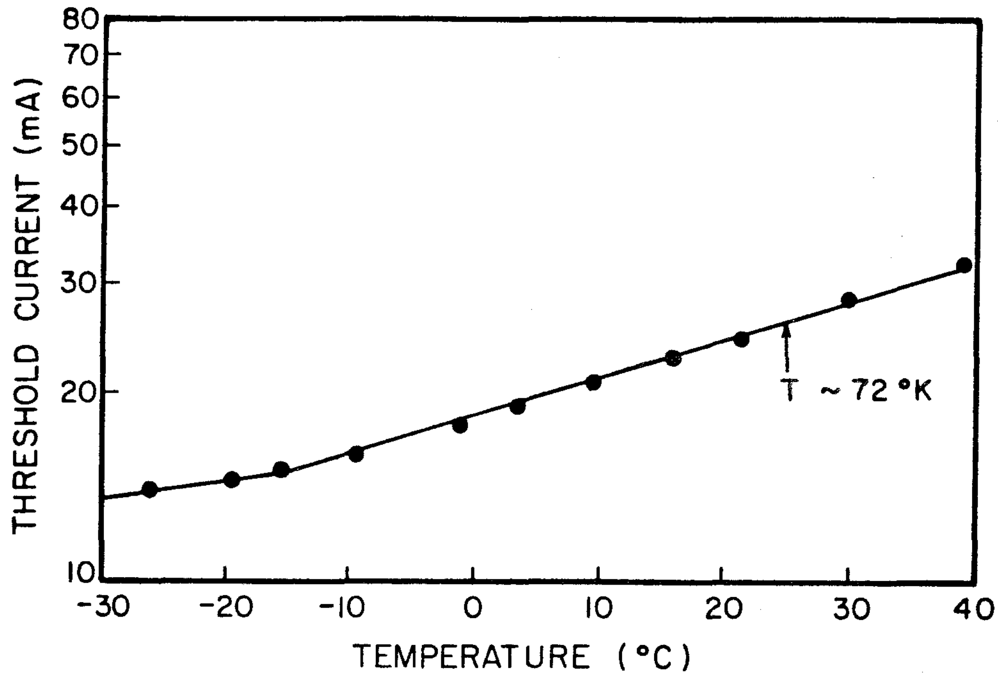

Fig. 2.13 Threshold current versus temperature plot of a Groove Laser.

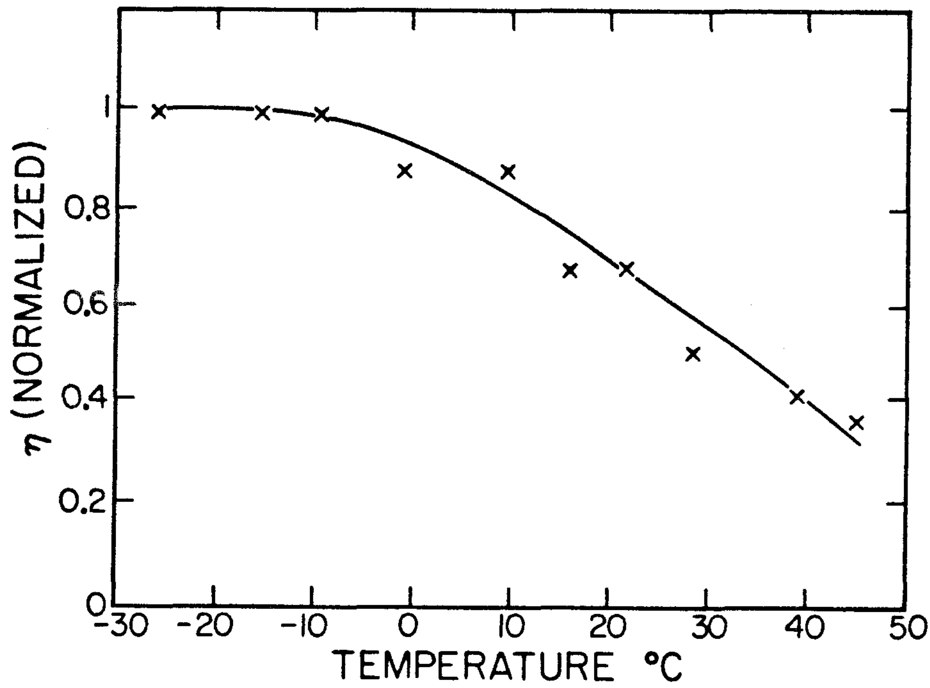

Fig. 2.14 External quantum efficiency (normalized) versus temperature plot of the same laser.

(where only the index of InP contributes) and nearly parabolic for $|y| \leq w/2$. For modes which are tightly confined within the central part of the active region (i.e. near y=0), the index at large y has negligible effect on the resultant mode shape and the analytical solution is applicable. With this index profile, we obtain the modal (equation A-6 in Appendix 2-1) profile $G_{\mu,\nu}(y)$:

$$G_{\mu,\nu}(y) = H_\nu(k^{\frac{1}{2}} P_\mu^{\frac{1}{4}}) e^{-\frac{k\sqrt{P_\mu}\, y^2}{2}} \tag{3}$$

and the corresponding propagation constant :

$$\beta_{\mu,\nu}^2 = \beta_{\mu,\nu}^2(0) - (2\nu + 1)k\sqrt{P_\mu} \tag{4}$$

where $P_\mu = 8(n_2^2 - n_{eff,\mu}^2(y_0))\frac{t_o}{t_{eff,\mu} w}$, H_ν's are Hermite polynomials, ν is the lateral mode index and μ is transverse mode index. In this case, the fundamental lateral mode has a Gaussian profile with a near field spot size (FWHP), S_o :

$$S_o = \left\{\frac{4\log 2}{k\sqrt{P_\mu}}\right\}^{\frac{1}{2}} \tag{5}$$

and the far field intensity profile, $I(\Theta)$, for the fundamental and first order mode are :

$$I_o(\Theta) \approx \cos^2\Theta\, e^{-\frac{k^2 \sin\Theta}{2b}} \tag{6}$$

$$I_1(\Theta) \approx \sin^2 2\Theta\, e^{-\frac{k^2 \sin\Theta}{2b}} \tag{7}$$

where $b = \frac{k\sqrt{P_\mu}}{2}$. With a 5 μm wide crescent waveguide which is 0.5 μm thick in the middle, and values of n_{InP} = 3.52 and $n_{InGaAsP}$ = 3.61 (for active layer with emission wavelength at 1.18 μm), we obtain $n_{eff,o}$ (0) = 3.56 and $t_{eff,o}$ = 1.16 μm. From these values, we obtain a far field beam divergence (FWHP) for the fundamental mode of 18.8 ° and the peak to peak separation of the first order mode as 16.4 °. These agree with the experimental results for the Groove Laser, where

a far field beam divergence of $18\pm 2\,^{\circ}$ is observed for the fundamental mode. At higher injection level, the first order appears and the peak to peak separation is measured to be $15\pm 2\,^{\circ}$.

2.5 Terrace Laser

The Groove Lasers possess many desirable characteristics. However, they are limited in optical output due to the small volume of the active waveguide. Our next design is a structure which allows the optical modes to spread out to a volume larger than that defined by injection. This structure -- the Terrace Laser on semi-insulating InP -- is fabricated with layers grown on the side of an etched terrace [14]. This laser and the Groove Laser have similar waveguiding mechanisms but slightly different lateral current confinement. The Terrace Lasers operate in a stable single transverse mode even when the injection current is more than five times the threshold current. A schematic of the lasers is shown in figure 2.16. The quaternary region is crescent shaped and is terminated on one side by the terrace wall while the other side narrows towards a uniformly thin cross section. An SEM photograph of the laser is shown in figure 2.16.

2.5a Fabrication

The fabrication of the lasers is summarized as follows. A 4-5 μm high terrace is etched into a semi-insulating InP with Si_3N_4 as etching mask and is then loaded for epitaxy. With Si_3N_4 as growth mask, growth can only take place within the terrace and the resulting layers, two InP cladding and one quaternary layer, are grown as shown in figure 2.15. The typical doping concentration and thickness of these layers are : p-InP current confinement layer (Zn-doped, $2-5\times 10^{17}cm^{-3}$; 0.5 μm thick), InGaAsP layer (undoped; 0.2-0.3 μm thick at the

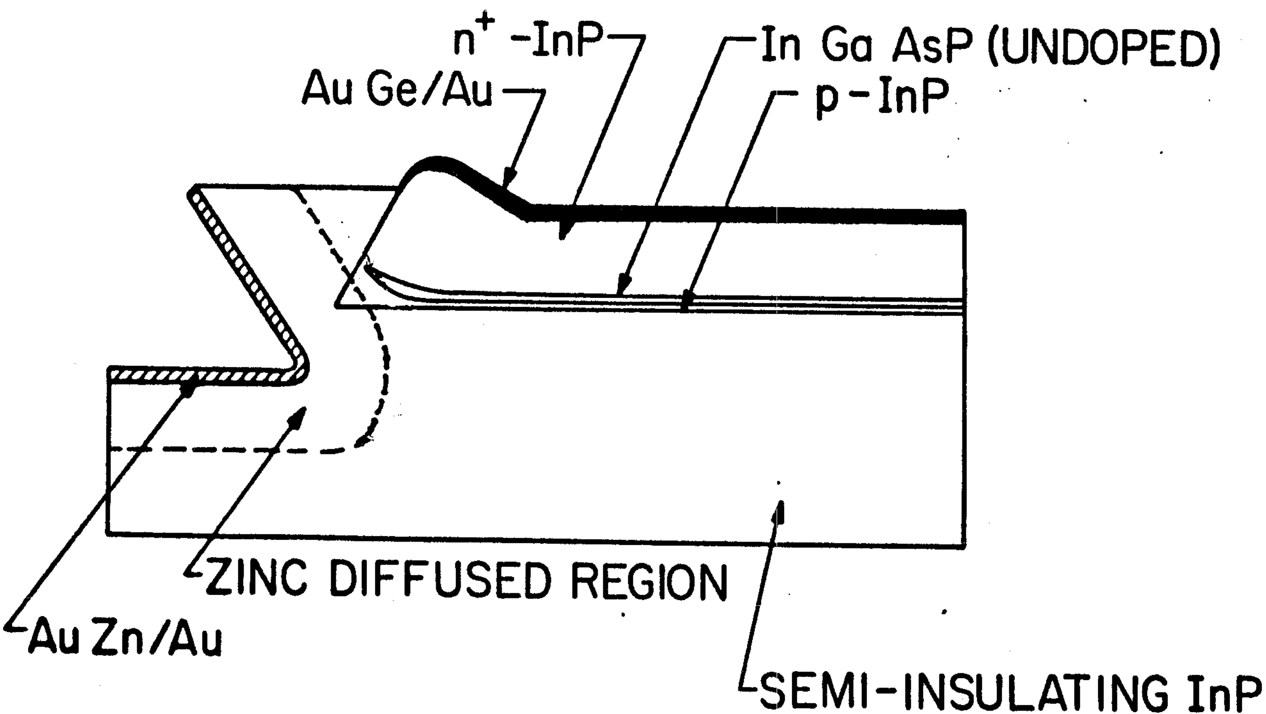

Fig. 2.15 A schematic diagram of a Terrace Laser on semi-insulating InP. The p-contact is achieved with a lateral Zn diffusion.

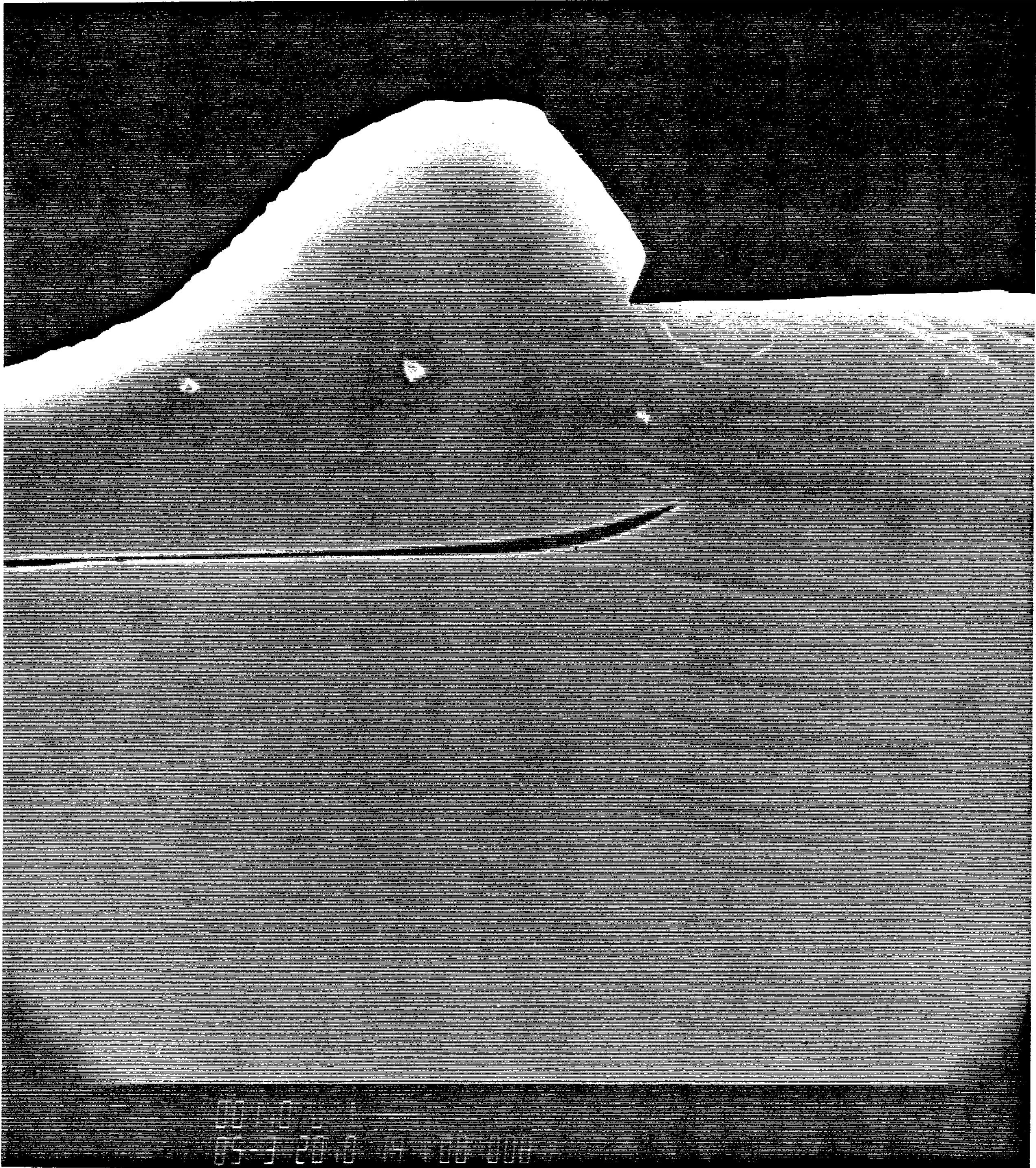

Fig. 2.16 An SEM photograph of a Terrace Laser after LPE.

thickest part), n^+-InP cladding layer (Sn-doped, $2\times10^{18}cm^{-3}$; 2-3 μm thick). The growth time of the p-InP is minimized such that InP only grows near the terrace corner. p-contact to the p-InP layer is done with a lateral Zn diffusion similar to that made on the groove lasers, and with the diffusion front almost touching the middle of the crescent. Since the low doped p^--InP has high electrical resistance, the hole injection mainly occurs from Zn diffused region (lower resistance) into the closeby quarternary region thus minimizing the current spreading and reducing the effective injection stripe width. This is responsible for the low laser threshold currents.

2.5b Characteristics

The lasers are tested with 50 ns pulses. The threshold current ranges from 35-50 mA. Typical light versus current characteristics are shown in figure 2.17. The external differential quantum efficiency is about 45 % for both facets. Single fundamental mode operation is maintained up to high injection current level. High optical power output (~ 170 mW/facet at pulsed operation) is obtained with this laser as the optical mode can spread out to a large waveguiding region. A typical far field pattern is shown in figure 2.18.

2.5c Large optical cavity Terrace Lasers

We have furthermore exploited the high power output characteristics of this laser by enlarging the optical cavity to increase the volume for guided modes [15]. In the large optical cavity (LOC) structures, the lasing mode acquires gain from a thin (0.05-0.2 μm) active layer, before spreading into a thicker (0.5-1.5 μm) guiding layer. The mode is still confined within these layers due to the dielectric index step between these layers and the cladding layers. The mode

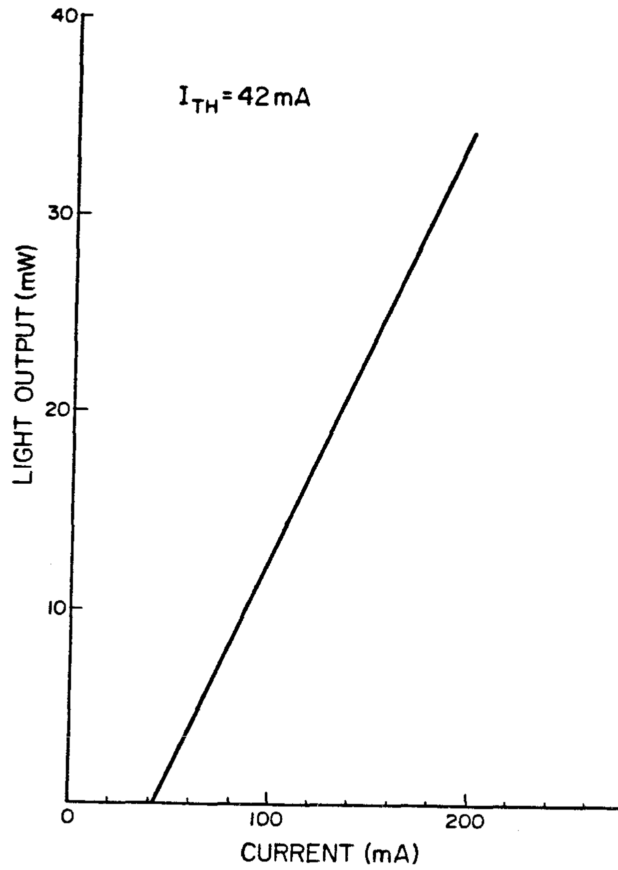

Fig. 2.17 L-I characteristics of a Terrace Laser.

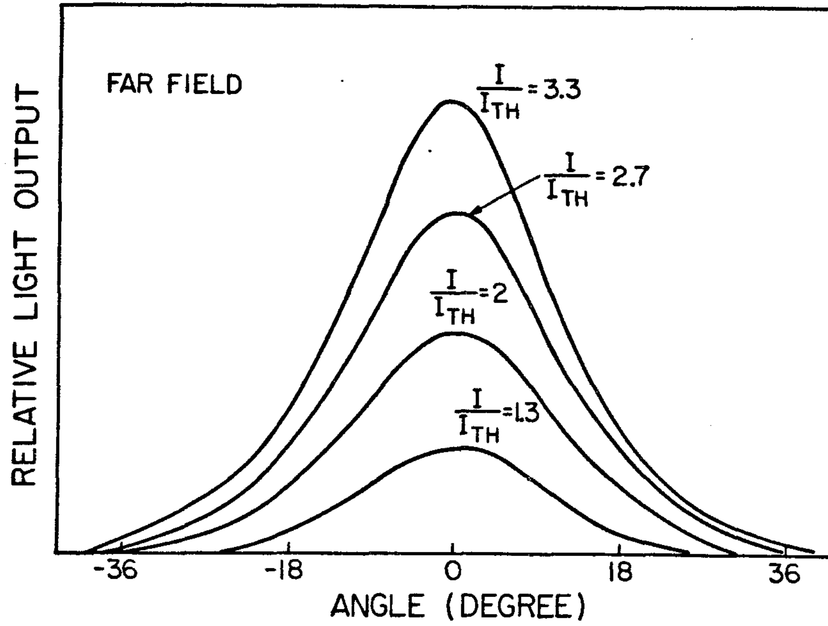

Fig. 2.18 Far field patterns of a Terrace Laser.

spreading leads to a narrowing of the output beam divergence, thus easing the laser coupling to optical fibers. The peak power output is limited by mirror heating and can increase correspondingly, as the lateral area for light emission is increased by a factor of 2 to 4.

The layers are grown as shown in figure 2.19. For this terrace structure, the extra quaternary guiding layer leads to an increase in both the thickness and the effective width of the waveguide. The thickness and composition of the active (corresponds to 1.27 μm emission) and the waveguiding (corresponds to 1.16 μm) layers are optimized such that energy gap difference (0.17 eV) between the two layers is adequate for active layer carrier confinement, while the small refractive index difference allows the optical mode to spread out into the guiding layer. With a 0.1 μm thick active layer and a 0.5-0.7 μm thick guiding layer, the threshold current ranges from 50 to 70 mA and the maximum pulsed output power (at 50 ns pulsewidth) is 300 mW per facet (at 2.2 A injection current). The differential quantum efficiency is about 50 % for both facets (at 10 mW power output). Typical light versus current characteristics are shown in figure 2.20 and are linear up to 5 times threshold current. The far field pattern, as shown in figure 2.21, is very smooth and regular indicating stable fundamental mode operation even up to five times threshold current. The laser beam divergence, which is 20 ° parallel and 30 ° perpendicular to junction plane, is considerably smaller than the width of the Terrace Lasers with no guiding layer.

2.6 Conclusion

In conclusion, single-step LPE InGaAsP lasers on both conductive and semi-insulating InP have been fabricated with selective epitaxy. Low threshold CW operation is obtained using novel semi-insulating structure for current

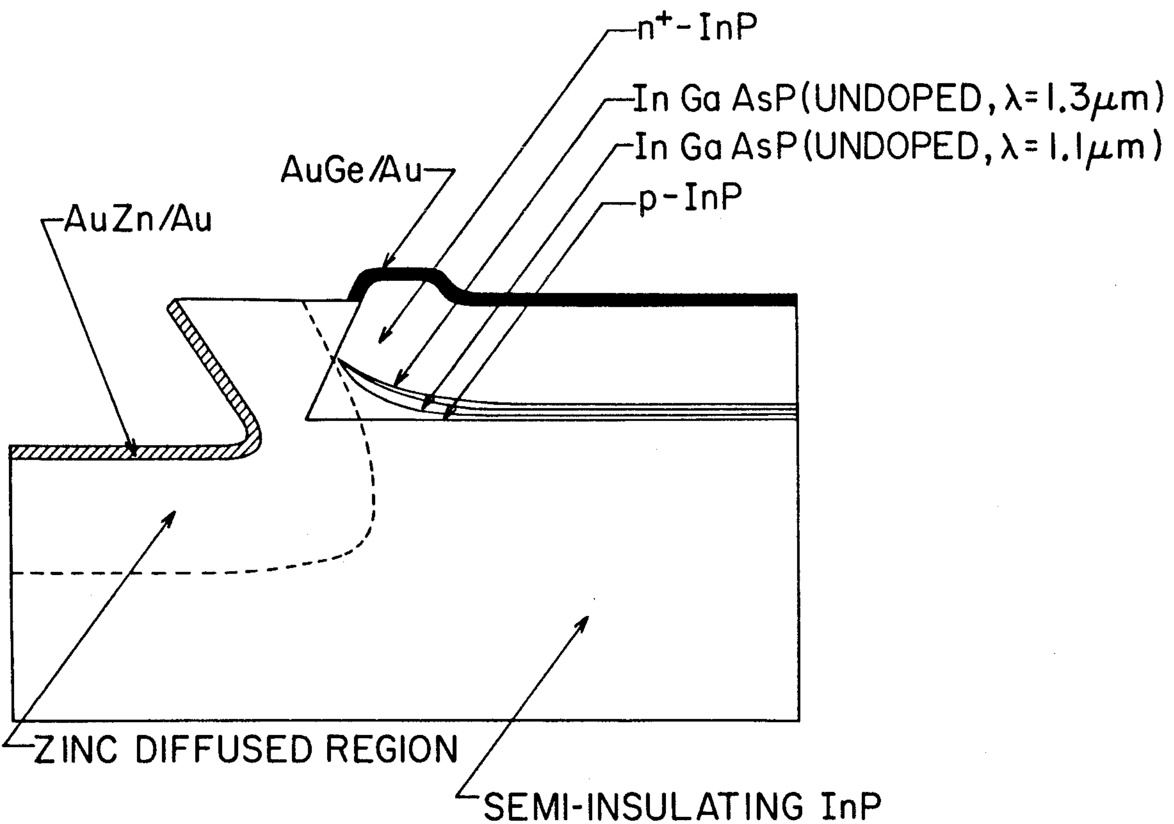

Fig. 2.19 A schematic cross-section of a Large Optical Cavity Terrace Laser.

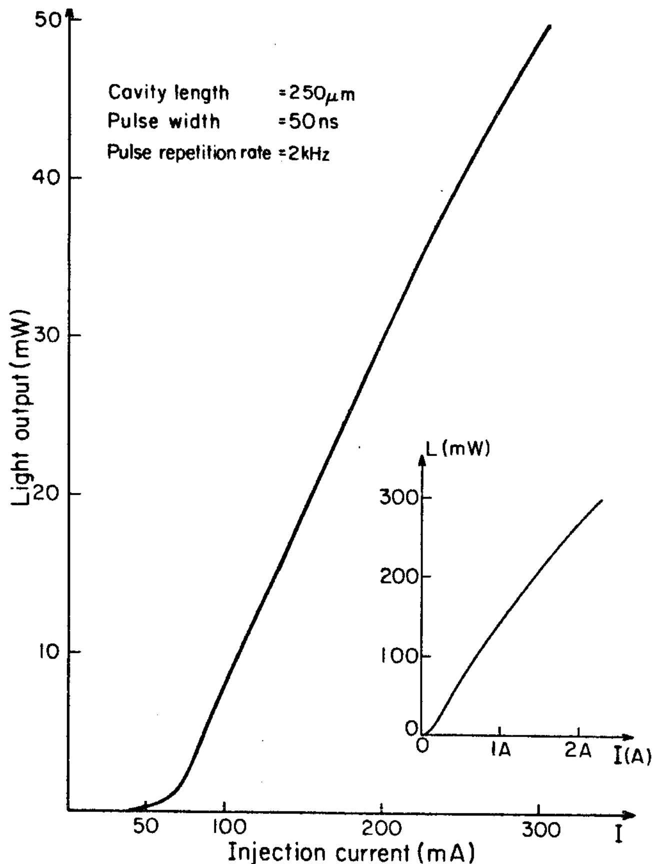

Fig. 2.20 L-I characteristics of a Large Optical Cavity Terrace Laser. I_{th} is 65 mA.

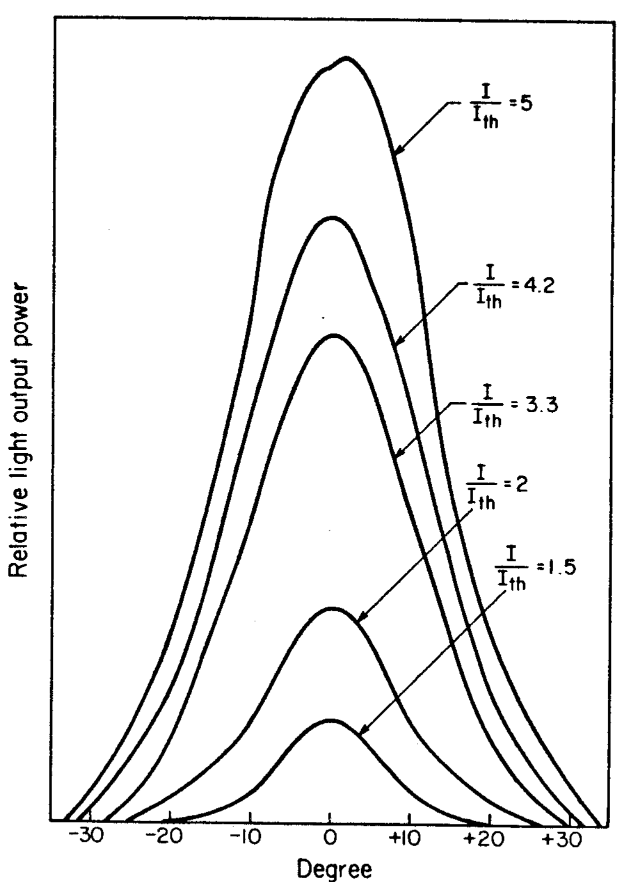

Fig. 2.21 Far field patterns of a Large Optical Cavity Terrace Laser at pulsed operation.

confinement in the Groove Lasers. High output power is obtained with the large optical cavity Terrace Lasers.

Appendix 2-1 : Perturbative effective index method in waveguide analysis

In optical waveguide analysis, the effective index method [16,17] is a powerful technique for solving the wave equation. It is particularly useful for waveguides where strong optical guiding occurs in one transverse (normal to direction of propagation) direction (namely in the x direction) while weak optical guiding obtained along the other perpendicular direction (say, the y direction). The method involves the calculation of the lateral waveguide effective-index distribution which can then be employed to evaluate the lateral field variation and thus the modal propagation constants. For waveguides with weak lateral index variation, the optical modes can usually be divided into pseudo TE and pseudo TM modes. TE modes have a vanishing electric field component in the propagating direction, while pseudo TE modes have a small but nonvanishing component. Similarly, pseudo TM modes have dominant transverse magnetic field components. In what follows, we consider only pseudo TE modes as they usually dominate over pseudo TM modes in laser oscillation due to their larger mode mirror reflectivities.

Consider the wave equation for the electric field $\overline{E}(r,t)$ [18]:

$$\nabla^2\overline{E} + \nabla\left(\overline{E}\cdot\frac{\nabla\varepsilon}{\varepsilon}\right) = \frac{\varepsilon(x,y)}{c^2}\frac{\partial^2\overline{E}}{\partial^2 t} \qquad \text{(A-1)}$$

in which $\varepsilon(x,y)$ is the complex permitivity of the medium. If ε varies slowly in a wavelength, the second term on the left hand side can be dropped. Furthermore, consider a mode propagating in the z direction with transverse electric field component polarized in the y direction:

$$E_y(r,t) = E_{0y}(x,y)e^{-i(\omega t-\beta z)} \qquad \text{(A-2)}$$

Now, with assumed step x and slow y variations of $\varepsilon(x,y)$, the modes are more strongly guided in the x direction than in the y direction, thus E_{0y} can take the

form :

$$E_{0y}(x,y) = F(x,y)\,G(y) \tag{A-3}$$

With these assumptions, the wave equation in (1) becomes :

$$G(y)\frac{\partial^2 F}{\partial x^2} + F(x,y)\frac{\partial^2 G}{\partial y^2} + k^2(n^2(x,y) - \beta^2)FG + G\frac{\partial^2 F}{\partial y^2} + 2\frac{\partial F}{\partial y}\frac{dG}{dy} = 0 \tag{A-4}$$

where $n^2(x,y) = \varepsilon(x,y)$ and $k = \omega/c$. The last two terms are usually taken to be small and are dropped, thus we have the following equations :

$$\frac{\partial^2 F}{\partial x^2} + (k^2 n^2(x,y) - \beta_{xo}{}^2(y))F = 0 \tag{A-5}$$

$$\frac{d^2 G}{dy^2} + (\beta_{xo}{}^2(y) - \beta_o{}^2)G = 0 \tag{A-6}$$

Equation A-5 is solved first for $F(x,y)$ and $\beta_{xo}{}^2(y)$. It is a one dimensional equation with appropriate boundary conditions for the TE modes. With calculated $\beta_{xo}{}^2(y)$, equation 6 can be solved to get the modal propagation constant β_o. In general, β_o is complex accounting for real index waveguiding as well as gain guiding in the medium. In cases where the last two terms in equation A-4 are small but not negligible, we can use the perturbation to calculate their contribution to β_o. We can first include the term $\frac{d^2F}{dy^2}G$ as a perturbation in equation A-5 :

$$\frac{\partial^2 F}{\partial x^2} + k^2 n^2(x,y)F + \frac{\partial^2 F}{\partial y^2} = \beta_x{}^2 F \tag{A-7}$$

where

$$\beta_x{}^2(y) = \beta_{xo}{}^2(y) + \Delta\beta_x{}^2(y) \tag{A-8}$$

with β_{xo} the eigenvalue of equation A-5 and the $\Delta\beta_x{}^2(y)$ approximated by first order perturbation theory :

$$\Delta\beta_x^2(y) = \frac{\int_{-\infty}^{+\infty} F^* \frac{\partial^2 F}{\partial^2 y} dx}{\int_{-\infty}^{+\infty} |F|^2 dx} \tag{A-9}$$

where F^* is the complex conjugate of F. Assuming the modes considered are guided modes with the boundary condition $F(\pm\infty)=0$, equation A-9 becomes :

$$\Delta\beta_x^2(y) = -\frac{\int_{-\infty}^{+\infty} \left|\frac{\partial F}{\partial y}\right|^2 dx}{\int_{-\infty}^{+\infty} |F|^2 dx} \tag{A-10}$$

Therefore, this correction can account for waveguides with abrupt index change in the lateral direction, provided the abrupt change of index takes place in a distance which is a fraction of a wavelength.

Similarly, $\frac{dF}{dy}\frac{dG}{dy}$ gives rise to a small correction to $\beta_{xo}^2(y)$:

$$\Delta\beta_x^2(y) = \frac{\int_{-\infty}^{+\infty} F^* \frac{\partial F}{\partial y} dx}{\int_{-\infty}^{+\infty} F^* F dx} \frac{1}{G}\frac{dG}{dy} \tag{A-11}$$

Since this expression involves G(y), it has to be solved self-consistently with equation A–6 to obtain the lateral index profile. For waveguides having vertical symmetry, that is $\varepsilon(x,y)=\varepsilon(-x,y)$ about the y-axis, this correction term is zero.

In some laser waveguide designs, it is desirable to obtain explicit expressions relating the waveguide parameters and the resulting index profile and thus waveguiding characteristics. Although the effective index method discussed above can be applied point by point to obtain the lateral index profile, it is also possible to extend the method to express the modes explicitly. This extended method has the further advantage of efficiency while giving an index profile closely approximating the actual one. As shown below, this method employs

first order perturbation theory. For simplicity, consider a three layer slab waveguide with the index in each layer slowly varying in the y direction (figure 2.22) :

$$n_i^2(y) = n_i^2(y_o) + \Delta n_i^2(y) \tag{A-12}$$

where i=1,2,3 corresponding to the three layers and y_o is an appropriate origin for the generally complex n_i^2's. First of all, the effective index method is used to solve the effective index n_{eff} at y_o $\left[n_{eff}(y_o)=\frac{\beta_{xo}(y_o)}{k}\right]$ and the corresponding $F(x,y_o)$. This is done by solving equation A-5 for a waveguide shown in figure 2.23. Next, the first order perturbation theory is used to calculate $n_{eff}(y)$ for $y \neq y_o$, with $\Delta n_i^2(y)$ as the perturbation in equation A-5 :

$$n_{eff}^2(y) = n_{eff}^2(y_o) + \Delta n_{eff}^2(y) \tag{A-13}$$

where

$$\Delta n_{eff}^2(y) = \frac{\int_{-\infty}^{+\infty} F^*(x,y_0)\Delta n^2(x,y)F(x,y_o)dx}{\int_{-\infty}^{+\infty} F^*(x,y_0)F(x,y_o)dx} \tag{A-14}$$

This method is justified if the correction term $\Delta n_{eff}^2(y)$ is much smaller than the unperturbed value of n_{eff} at y_o, which is usually the case for waveguides with slow lateral index variation. With this $\Delta n_{eff}^2(y)$, we have a new equation for G(y) :

$$\frac{d^2G(y)}{dy^2} + k^2\Delta n_{eff}^2(y)G(y) = \beta^2 G(y) \tag{A-15}$$

where

$$\beta^2 = \beta_o^2 - k^2 n_{eff}^2(y_o)$$

and β_o is defined in equation 2 to be the modal propagation constant. As seen from equation A-15, the general shape of the eigenfunction G(y) is determined

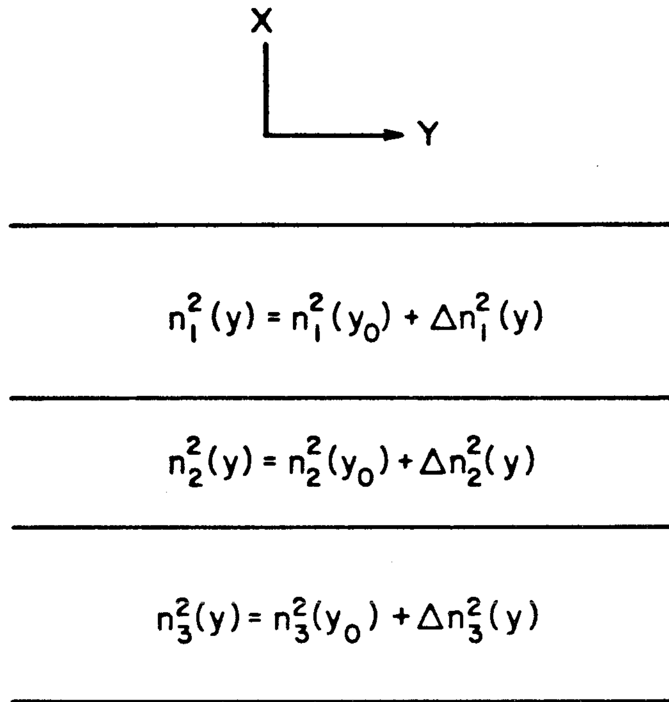

Fig. 2.22 A three layer slab waveguide with slow lateral index variation.

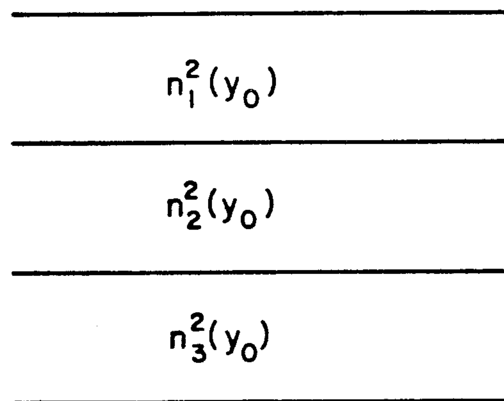

Fig. 2.23 A three layer slab waveguide with constant index in each layer.

by the relative lateral index difference and not by the absolute index value at each lateral position. Equation A-15 has analytic solutions for some explicit forms of $\Delta n_{eff}^2(y)$. For complex n_i^2 's, this perturbative approach provides a means for analyzing gain guiding as well as real index guiding.

This method can also be applied to waveguides in which the active region varies in thickness. For instance, the waveguide structure shown in figure 2.24 has a middle layer thickness variation $\delta(y)$ which can be related to index variation by :

$$\Delta n_2^2(y) = n_2^2 - n_1^2 \qquad 0 < x < \delta(y) \tag{A-16}$$

$$= 0 \qquad \text{elsewhere}$$

For simplicity, the y_o is chosen to correspond where the middle layer (t_o) is thickest. Then from equation A-14, it is found that for TE modes :

$$\Delta n_{eff}^2(y) = 2(n_2^2 - n_{eff}^2(y_0))\frac{\delta(y)}{t_{eff}(y_o)} \tag{17}$$

where t_{eff}, the effective modal thickness in the x direction, is :

$$t_{eff}(y_0) = t(y_o) + k_{10}^{-1} + k_{30}^{-1}$$

with $k_{jo}=k(n_{eff}^2(y_o) - n_j^2)^{\frac{1}{2}}$, j=1,3. As can be seen from equation A-17, for structures with tapering lateral thickness (i.e $\delta(y)< 0$), this $\Delta n_{eff}^2(y)$ profile provides either guiding or anti-guiding depending on whether n_2 is greater or less than $n_{eff}(y_o)$. Similarly, for waveguides with n_2 greater than $n_{eff}(y_o)$, $\delta(y) > 0$ give anti-guiding. Since $\Delta n_{eff}^2(y)$ is proportional to the thickness variation, the guiding or antiguiding effect is more prominent where the thickness variation $(\frac{d\delta(y)}{dy})$ is greater.

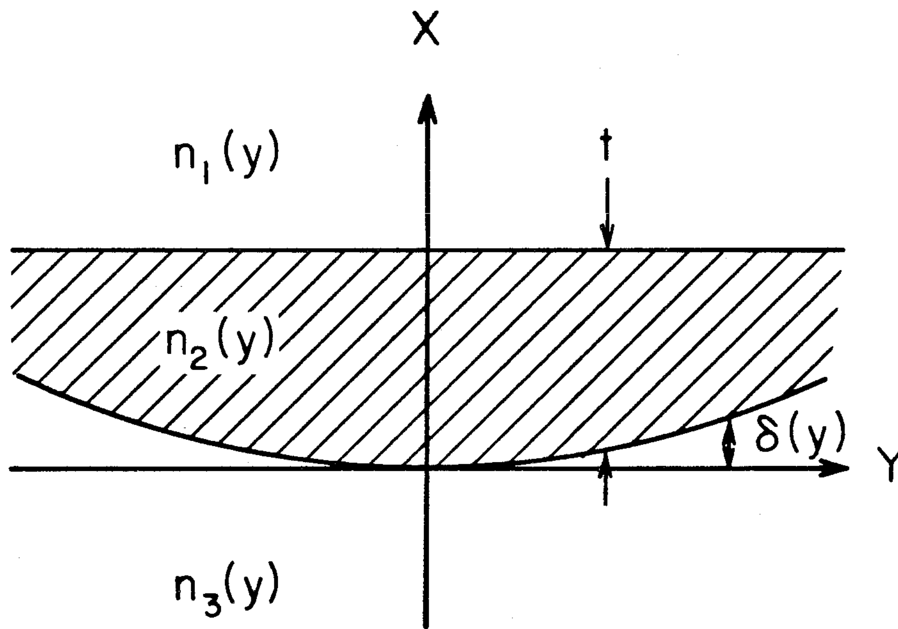

Fig. 2.24 A cross section of a three layer waveguide showing the thickness (t) variation of the middle layer.

References

1. R. E Nahory and M. A.Pollack, Elect. Lett., vol 14, pp728-729 (1978).

2. G. H. B. Thompson,'Physics of Semiconductor Laser Devices," Chapter 2, John Wiley and Sons (1980).

3. H. C. Cassey, Jr. and M. B. Panish, "Heterostructure Lasers," Part A, Acadamic Press (1978).

4. N. Bar-Chaim, J. Katz, I. Ury, and A. Yariv, Elect. Lett., vol. 17, pp. 108-109, (1981).

5. I. Samid, C. P. Lee, A. Gover, and A. Yariv, Appl. Phys. Lett., vol 27, pp. 405-407, (1975).

6. C. P. Lee, I. Samid, A. Gover, A. Yariv, Appl. Phys. Lett., vol 29, pp 365-367, (1976).

7. U. Koren, K. L. Yu, T. R. Chen, N. Bar-Chaim, S. Margalit, and A. Yariv, Appl. Phys. Lett., vol 40, pp. 643-645, (1982).

8. P. C. Chen, K. L. Yu, S. Margalit, and A. Yariv, Appl. Phys. Lett., vol 38, pp. 301-303, (1981).

9. G. A. Antypas, Appl. Phys. Lett., vol 37, 64 (1980).

10. T. Yamamoto, K. Sakai, S. Akiba, Y. Suematsu, IEEE, J. Quant. Electron., QE-14, pp. 95-98 (1978).

11. K. L. Yu, U. Koren, T. R. Chen, P. C. Chen, and A. Yariv, Electron. Lett., vol 17, pp. 790-792 (1981).

12. S. Margalit and A. Yariv, to be published in Metal and Semimetals, (1983).

13. U. Koren, A. Hasson, K. L. Yu, T. R. Chen, S. Margalit, and A. Yariv, Appl. Phys. Lett., vol 41, 791 (1982).

14. T. R. Chen, K. L. Yu, U. Koren, A. Hasson, S. Margalit. and A. Yariv, J. Appl. Phys., vol 53, pp. 7215-7217 (1982).

15. T. R. Chen, K. L. Yu, U. Koren, S. Margalit, and A. Yariv, Jpn. J. Appl. Phys., vol 21, L595-596 (1982).

16. G. B. Hocker, W. K. Burns, Appl. Opt., vol 16, pp. 113-116 (1977).

17. W. Streifer, R. D. Burnham, D. R. Scrifres, Appl. Phys. Lett., vol 37, pp. 121-123 (1980)

18. D. Marcuse, IEEE, J. Quant. Electron., QE-9, pp. 958-960 (1973).

Chapter 3

Mode Stabilization Mechanism of Buried-waveguide Lasers with Lateral Diffused Junctions.

3.1 Introduction

Application of semiconductor lasers, such as long distance fiber-optics communications, video-disk recording and readout, laser printing, etc., require high power operation of injection lasers combined with a stable single mode. Hence, it is important to understand the mechanisms which affect the transverse modal behavior, especially under high power operation.

For dielectric waveguides that support multiple transverse modes where injection is vertical (that is, the p-n junction is parallel to the wide dimension of the waveguide), such as in buried heterostructure (BH) lasers, it is very difficult to obtain fundamental transverse mode operation when the effective waveguide width is larger than the carrier diffusion length [1]. At higher powers, spatial hole burning [2] due to strong local stimulated emission would eventually give rise to a dip in the gain profile at the center of the waveguide, which leads to preferred lasing at higher order transverse modes. In contrast to this, an increasing stabilizing effect can take place (especially when the injection level is raised) in transverse junction injection lasers with real index guiding. In the next section, it will be shown how the gain profile favors lasing in the fundamental mode for a wide buried waveguide with a transverse p-n junction located near the middle of the guide. It will become clear that as the optical power increases, the gain profile becomes progressively narrower due to the decreased stimulated lifetime and thus the effective carrier diffusion length thereby offsets the spatial hole burning effect. For simplicity, the analysis is carried out on buried rectangular waveguide with a lateral diffused junction. Since the lateral mode sta-

bilization depends mainly on the lateral diffusion of injected carriers, the results of the analysis can be applied to waveguides of other shapes.

3.2 Lasers with lateral diffused junction—Theory

In this analysis [3], we study in detail the gain stabilizing mechanism for a laser with a dielectric slab waveguide structure and with a lateral p-n junction as shown in figure 3.1. The waveguide width is 2W, and the junction is located at x=a, where $-W \leq a \leq W$. Since guiding is due to a real index profile, we take the optical transverse mode intensity profile S(x) as independent of the injection level (see appendix 3-2 for validity):

$$S(x) = S_0 \sin^2 \frac{\pi(m+1)(x+b)}{2b} \qquad |x| \leq b \tag{1}$$

$$S(x) = 0 \qquad |x| \geq b$$

$$b = W - \xi \qquad \xi/W << 1 \tag{2}$$

where S_0b is the total optical power in the mode, and m=0,1,2,3,... is the mode order. ξ is a width parameter accounting for the real geometrical shapes of some non-rectangular waveguides. In particular, for the crescent waveguide which has a thick central region, this approximation works very well. The steady state lateral distribution of the photon density and the excess carrier densities inside the active region are described by the following equations :

$$D_{eff} \frac{d^2\Delta}{dx^2} = \frac{\Delta(x)}{\tau_s} + A(\Delta(x) - n_{om})S(x) \qquad -W \leq x \leq W \tag{3}$$

$$\frac{\int_{-W}^{+W} S(x)\, dx}{\tau_{ph}} = \int_{-W}^{+W} A(\Delta(x) - n_{om})S(x)\, dx \tag{4}$$

where $\Delta(x)$ denotes the excess carrier densities, Δ_n on the n side, and Δ_p on the p side. In equations 3 and 4, $D_{eff}(x)$ is diffusion coefficient, n_{om} is the minimal

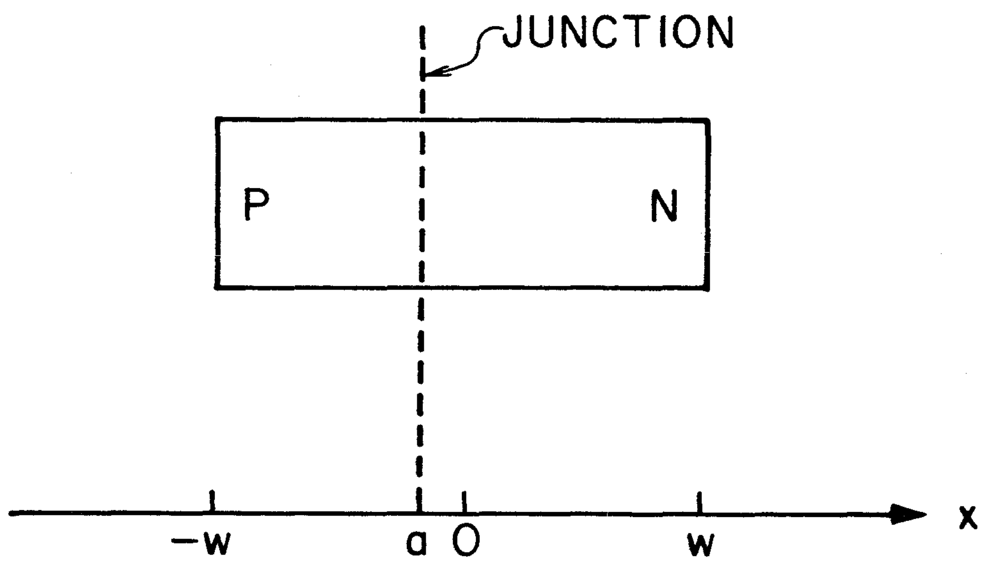

Fig. 3.1 A schematic diagram of the active waveguide with a lateral diffused junction at x=a.

carrier density to achieve positive gain, A is the optical gain constant, τ_{ph} is the photon lifetime, and τ_s is the spontaneous carrier lifetime. For simplicity, we neglect the contribution of spontaneous emission in equation 4.

With a given photon distribution S(x), we can solve for the carrier density profile $\Delta(x)$ from equations 3 and 4 and from this $\Delta(x)$ we can calculate the injection current density near the p-n junction at x=a,

$$J_p(a_+) = -qD_{eff}(x)\frac{d\Delta(x)}{dx} \tag{5}$$

$$J_n(a_-) = +qD_{eff}(x)\frac{d\Delta(x)}{dx}$$

$$J = J_p(a_+) + J_n(a_-) \tag{6}$$

where J_p is the injected hole current density on the n side, J_n is the injected electron current density on the p side, and J is the total current density.

3.2a Boundary conditions

The boundary condition is considered at x=W and at x=-W. Since the active waveguide is completely surrounded by higher bandgap material, the minority leakage current across these lateral heterobarriers is assumed to be negligible when compared to the injection current, thus:

$$J_p(+W) = 0 \tag{7a}$$

$$J_n(-W) = 0 \tag{7b}$$

Assuming thermal equilibrium is maintained throughout the waveguide, the Fletcher boundary condition [4] can be applied at the junction x=a, to relate the carrier densities on both sides:

$$\frac{n_n + \Delta_n}{n_p + \Delta_p} = \frac{n_n}{n_p} e^{-\frac{qV}{kT}} \tag{8}$$

$$\frac{p_p + \Delta_p}{p_n + \Delta_n} = \frac{p_p}{p_n} e^{-\frac{qV}{kT}} \tag{9}$$

In equations 8 and 9 n_n, p_p are the majority carrier densities, with p_n, n_p the corresponding minority carrier densities, on the n side and p side respectively. Δ_n is the excess carrier density on the n side, and Δ_p is that on the p side. V is the applied forward bias voltage.

Two injection cases are examined. In the first case, a p-n junction is located at x=a with high level injection into both p and n side. From equations 8 and 9, we have, at x=a,

$$\Delta_n(a_+) = \Delta_p(a_-) \tag{10a}$$

Also, due to the high level injection, D_{eff} in equation 1 is equal to the ambipolar diffusion coefficient D_a on both sides where on the n side :

$$D_a = \frac{(n_n + p_n + \Delta_n)D_n D_p}{(n_n + \Delta_n)D_n + (p_n + \Delta_n)D_p} \approx 2D_p \tag{11a}$$

and $D_n >> D_p$, $\Delta_n > n_n >> p_n$ are assumed. Similarly on the p side :

$$D_a = \frac{(p_p + n_p + \Delta_p)D_n D_p}{(n_p + \Delta_p)D_n + (p_p + \Delta_p)D_p} \approx 2D_p \tag{11b}$$

In the second case, a p^+-n junction at x=a produces high level hole injection into the n side, and low level electron injection into the p side. At x=a, from equations 8 and 9 we have:

$$[\Delta_n(a_+)]^2 = p_p \Delta_p(a_-) \tag{10b}$$

In this case, D_{eff} represents the ambipolar diffusion coefficient ($\approx 2D_p$) on the n side, and D_{eff} equals the diffusion coefficient of the n type carriers on the p side.

In Appendix 3-1, a self-consistent method is outlined to solve equations 3 and 4 for the carrier density profiles, with assumed photon profiles (such as that given in equation 1), subjected to the boundary conditions of equations 7a and 7b, and the junction boundary condition given in equations 8 or 9.

3.2b Analytical solution to the buried waveguide with lateral junction

We study a special case of the above waveguide. The lasers are assumed to operate predominantly in the fundamental mode (m=0) which has an inverted parabolic intensity mode profile:

$$S(x) = S_0\left(1 - \frac{\pi^2 x^2}{12W^2}\right) \qquad |x| < W \tag{1'}$$

$$S(x) = 0 \qquad |x| > W$$

where $8w/\sqrt{3}\pi$ is the total optical power in the mode and $2\sqrt{6}w/\pi$ is the width (FWHM) of the mode. The case of a lateral p-n junction located at the middle of the waveguide (x=0) is considered. The steady state distribution of excess carriers $\Delta(x)$ on either side of the junction, in the presence of the fundamental mode is governed by the diffusion equation with point injection at x=0 :

$$D_{eff}\frac{d^2\Delta}{dx^2} = \frac{\Delta(x)}{\tau_s} + A\Delta(x)S(x) \qquad -W \leq x \leq W \tag{3'}$$

where we have neglected the transparent term n_{om} and the contribution of spontaneous emission. Equation (3') is solved in the region $|x| < W$ with the boundary condition $\frac{d\Delta}{dx}(x=\pm W)=0$ and $\frac{d\Delta}{dx}(x=0)=I$, where I is the normalized pump current density injected across the transverse junction at x=0. These boundary conditions hold if the waveguide width (2W) is at least two diffusion lengths wide. Anticipating that the carriers are almost entirely concentrated near the center of the waveguide under high optical powers, solution range can be extended to

$|x| < \infty$ and thus the solution to (3') with the optical intensity distribution (1') is given by the Parabolic Cylinder Functions $U(x,y)$;

$$\Delta(x) = K\,U(a, \pm bx) \qquad x > 0$$

where

$$a = \left(\frac{3}{AS_0\tau^2 D_{eff}}\right)^{\frac{1}{2}} \frac{W}{\pi}(1 + A\tau_s S_0)$$

$$b = \left(\frac{AS_0}{3D_{eff}}\right)^{\frac{1}{4}} \left(\frac{\pi}{W}\right)^{\frac{1}{2}}$$

where K is a normalization constant determined from the gain (see equation 12 below). Assuming $W = 2\pi l_d/\sqrt{12}$ where l_d is the carrier diffusion length, we obtain the carrier distributions shown in figure 3.2 for different optical power levels S_0. Figure 3.2 shows that the width(FWHM) of the carrier profile decreases as the injection current increases. It is this localization of the carrier profile (and thus of the gain profile) at the center which discriminates against higher order transverse modes. The gain stabilization effect is enhanced at higher optical powers. More accurate results including the effects of the transparent term (n_{om}) and the higher order mode gains will be discussed below.

3.2c Results and discussion

We consider the following two cases :

Case 1: Figure 3.3 shows the calculated carrier profile for a p-n junction (i.e low doping levels on both sides), with high level injection into both sides, assuming that lasing takes place predominantly in the fundamental mode (m=0). The carrier density profiles are shown for different injection current densities. The S_0 's given in figure 3.3 are in units of $1/(A\ \tau_s)$ which takes the value of 1.3×10^{14}cm^{-2}. The value of n_{om} is taken as 1.2×10^{18}cm^{-3}. τ_s and τ_{ph} are taken as

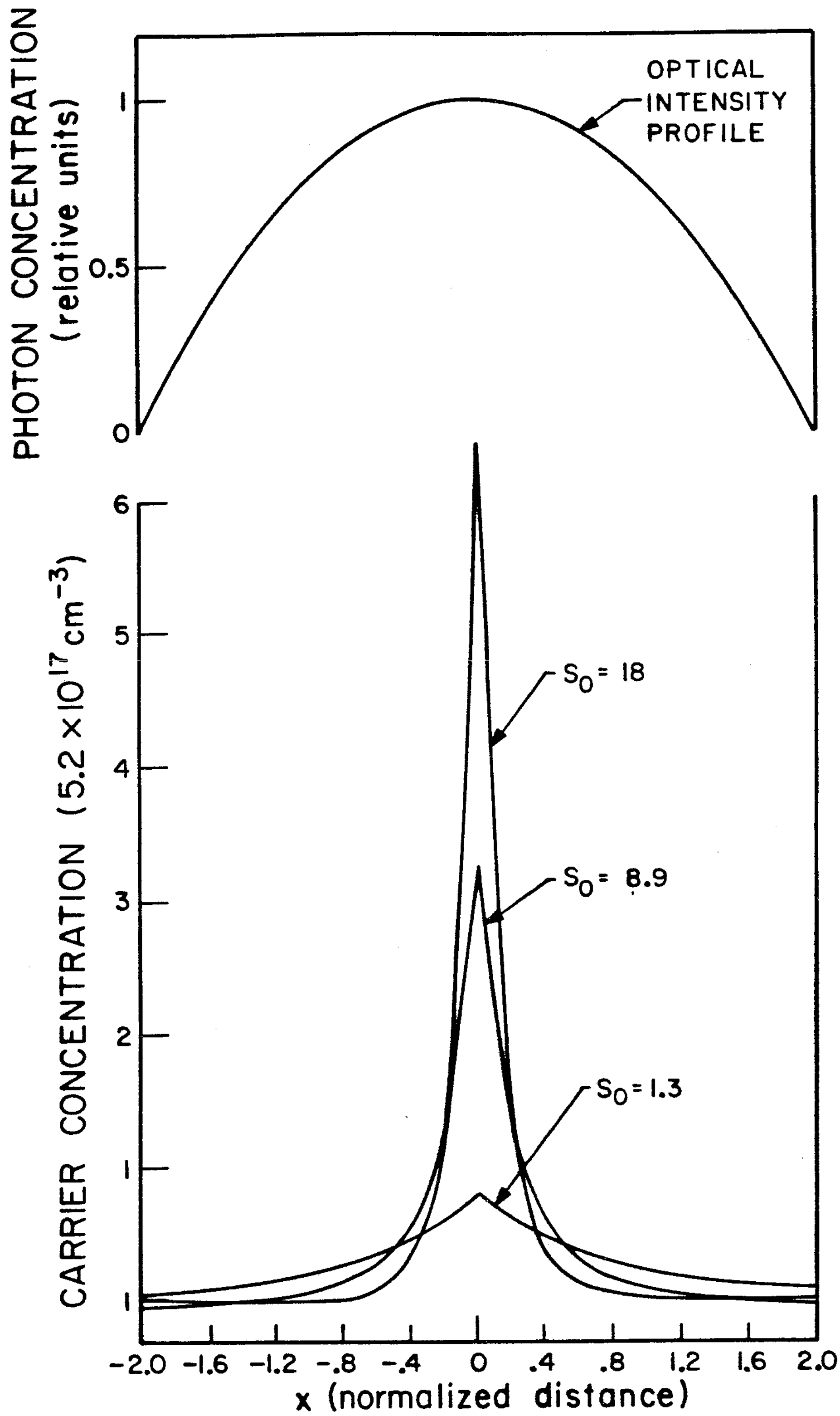

Fig. 3.2 Calculated carrier concentration for three values of optical power S_o. The fundamental mode intensity profile is shown in the upper part of the figure.

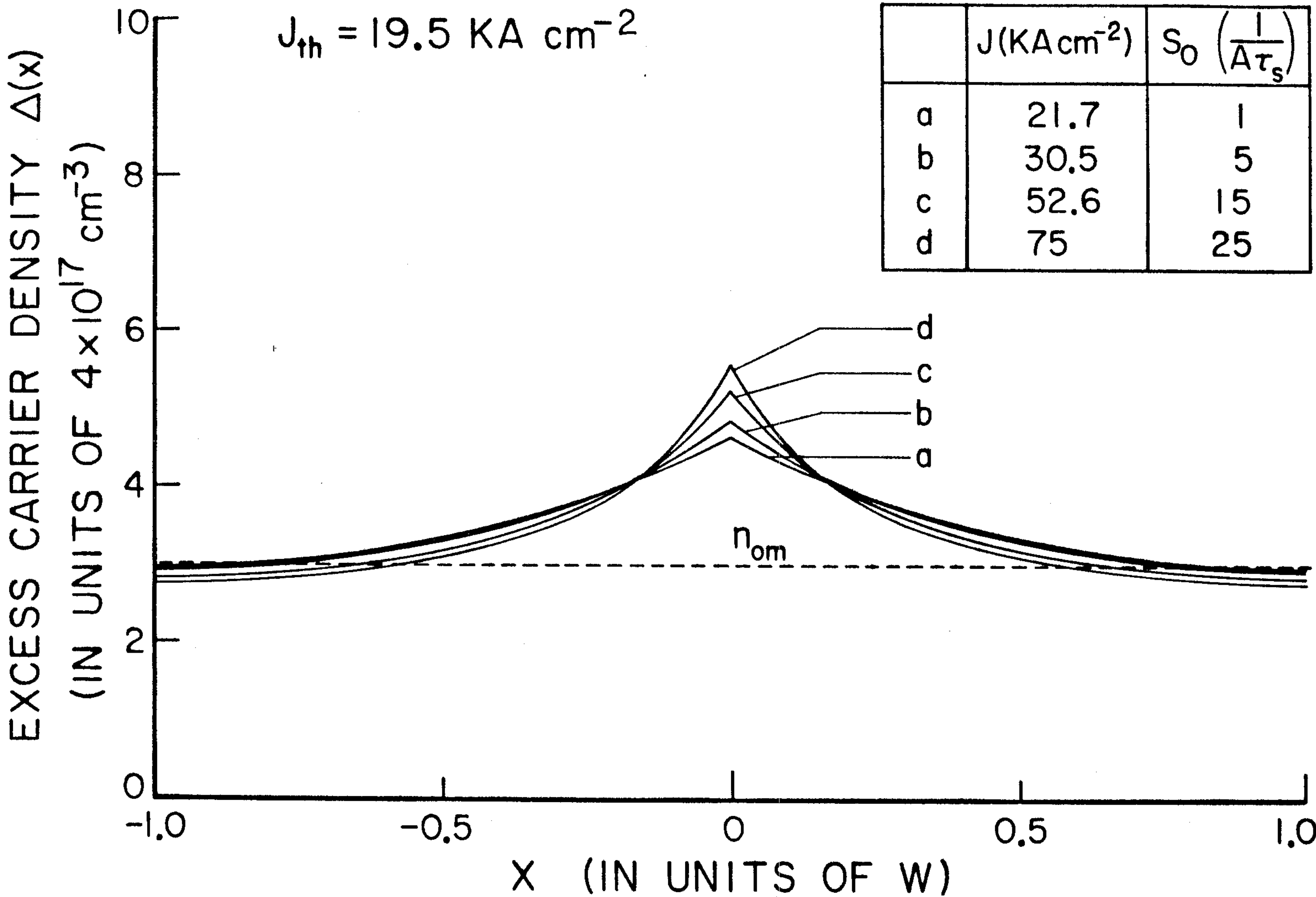

Fig. 3.3 Calculated excess carrier density profiles for a p-n junction at x=0. W is 2.6 μm. The dashed line shows the n_{om}.

6 ns. and 2 ps. respectively. The width of the waveguide is twice the ambipolar diffusion length ($\sim 2.6\ \mu m$), and ξ is taken to be W/5. Figure 3.3 shows how the width (FWHM) of the carrier profile decreases as the injection current increases. An increase in the injection current causes an increase in the optical power, which results in a decrease in the stimulated lifetime and hence a decrease in the effective carrier diffusion length. As a result, the injected carrier profile narrows. To study the effect of the location of the junction on the threshold current density, the carrier density profiles with the junction located at $x=-3W/4$ are shown in figure 3.4. At a given injection level, the overlap of the carrier distribution with the fundamental mode profile decreases as the junction is shifted away from the center. This results in a reduction in mode gain and thus an increase in the threshold current density. Also the p side portion decreases as the junction approaches the $x=-W$ waveguide boundary. The injected electrons on the same side become more laterally confined leading to lower $J_n(a_-)$ and thus the current is mainly due to hole injection. The converse happens on the n side : $J_p(a_+)$ decreases as the junction moves toward $x=W$. In figure 3.5, threshold current density is plotted, for the fundamental mode ($m=0$) and the first three higher order modes, as a function of the junction location. It is seen that, provided that the junction is placed near the center of the waveguide ($x=0$), the fundamental mode has the lowest threshold current density and is thus favored. On the other hand, if the junction is located near the ends of the waveguide, higher order modes will be preferred. As the waveguide width is increased, a higher threshold current density results, due to decreased lateral carrier confinement. The carrier profile tends to be more sharply peaked, as the width of the waveguide increases. In figure 3.6, we plot the threshold current density of a laser with the junction located in the middle of the waveguide, versus the width of the waveguide. The laser is assumed to operate

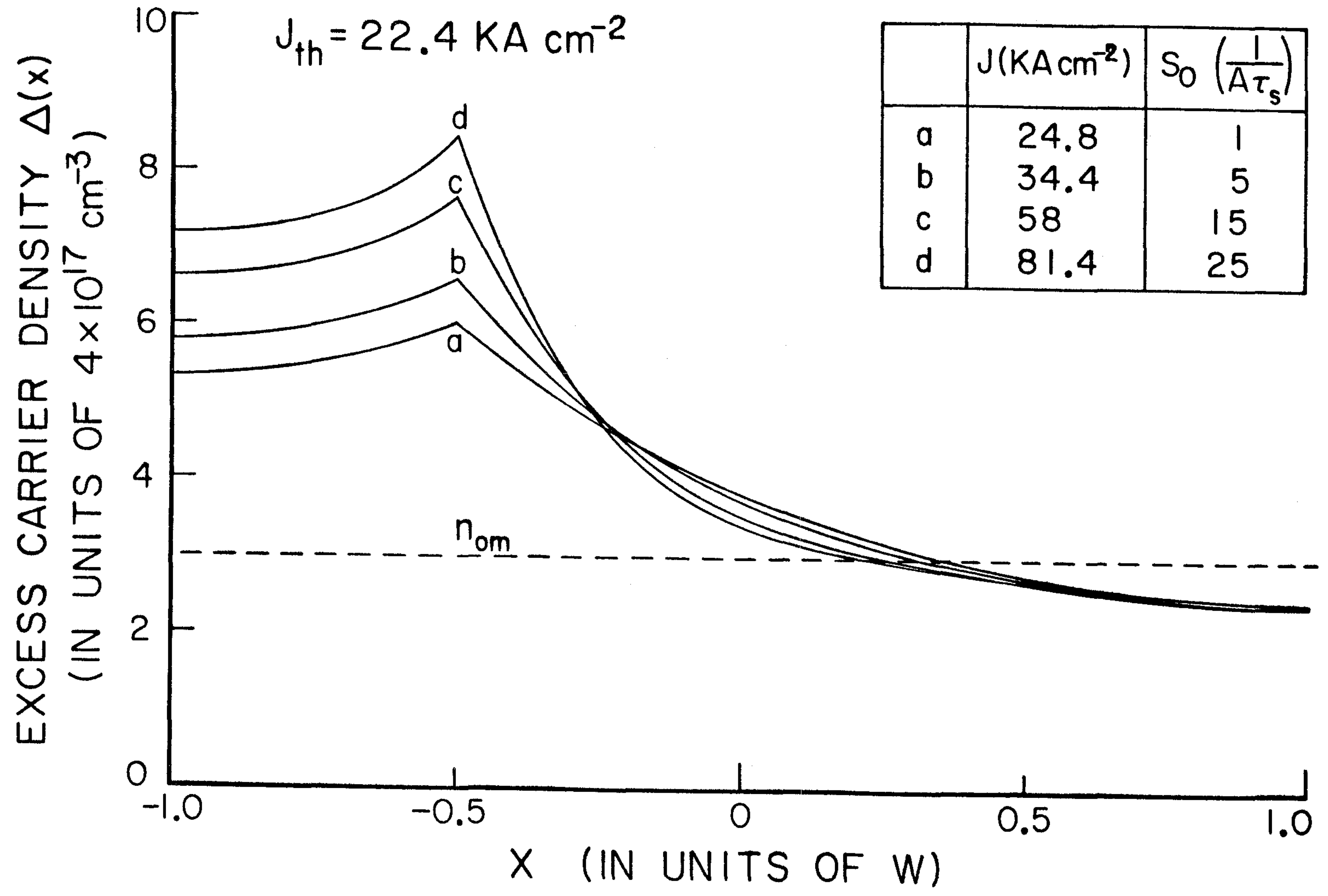

Fig. 3.4 Calculated excess carrier density profiles for a p-n junction at x=-3W/4.

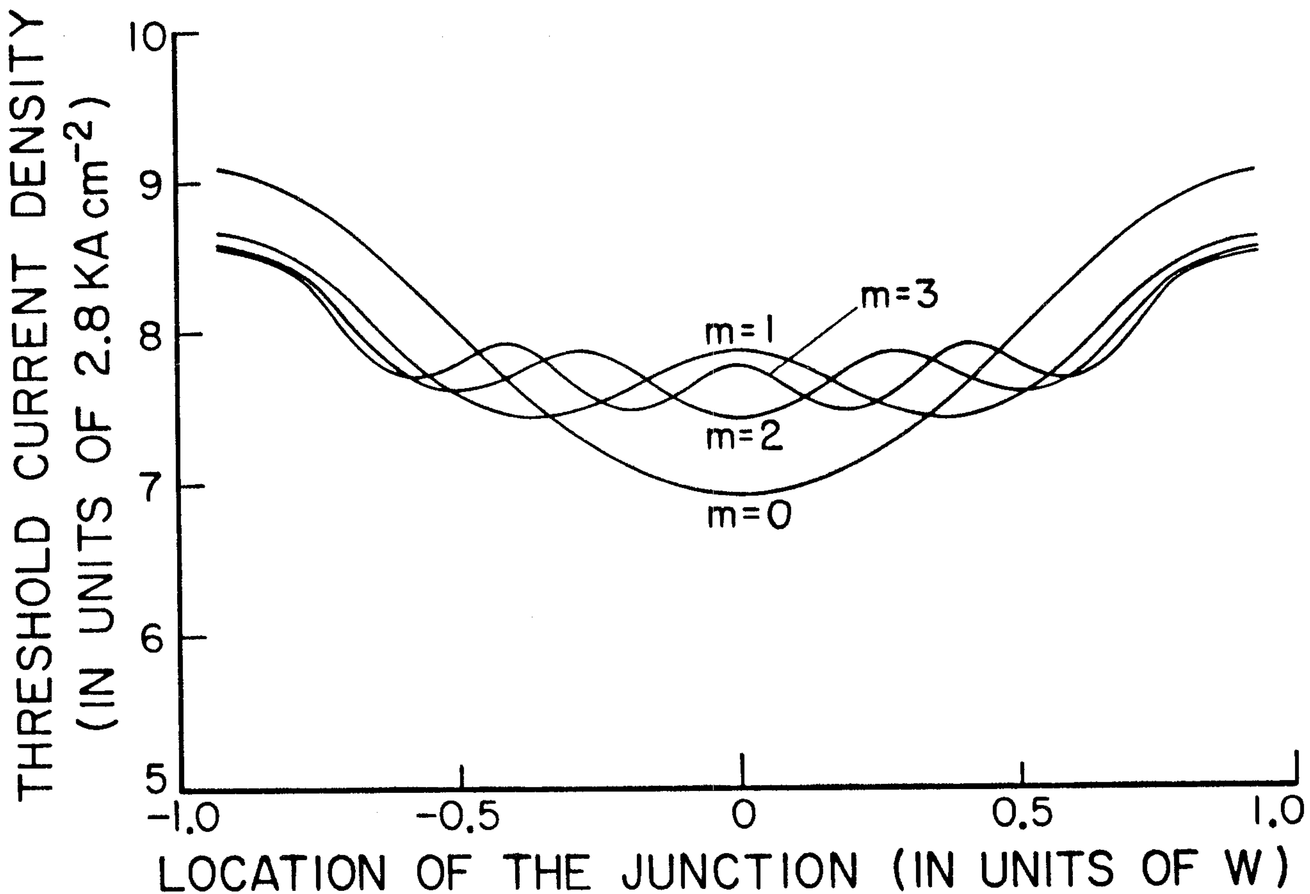

Fig. 3.5 Calculated threshold current density versus the location of the junction, with the laser lasers in the mth mode.

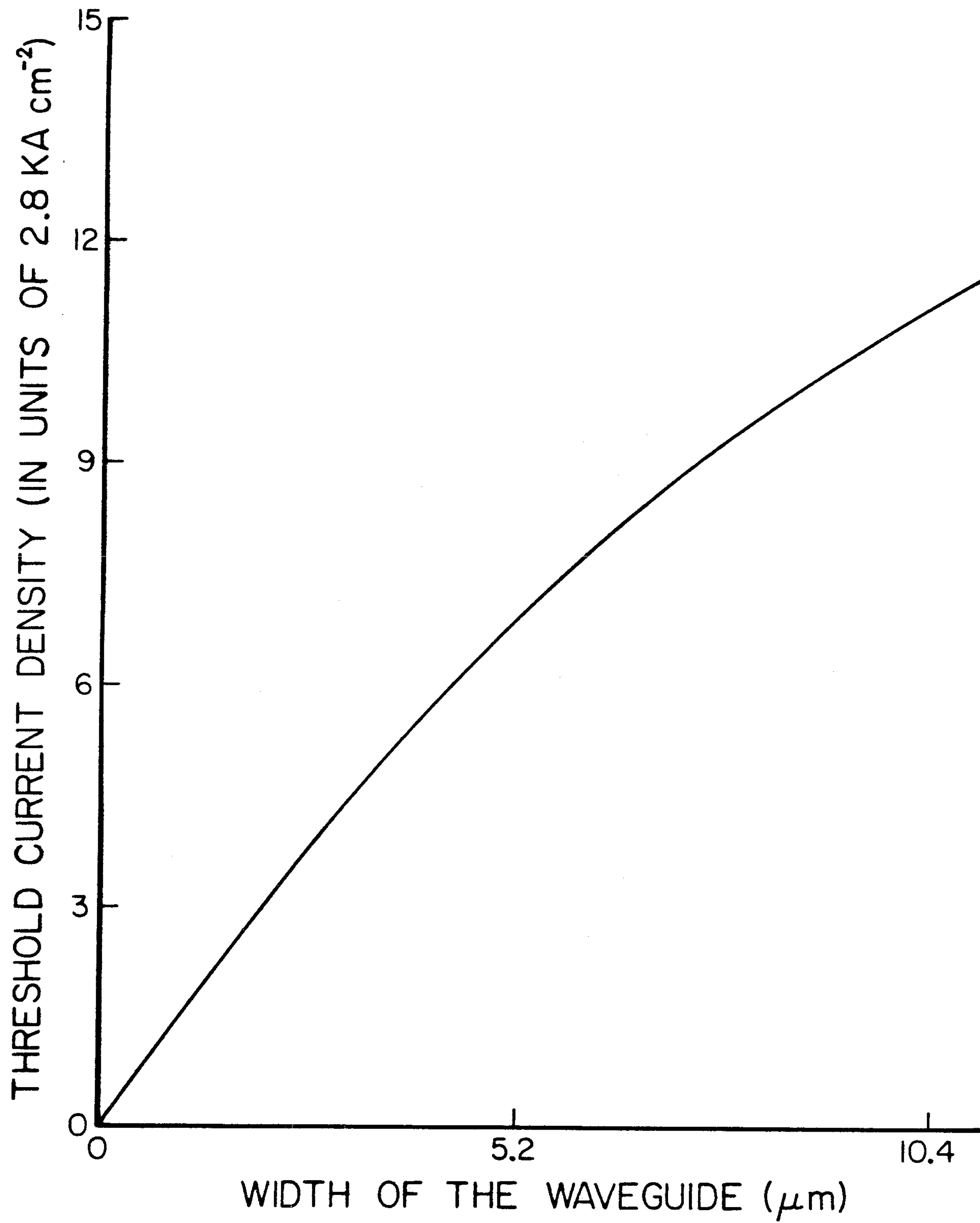

Fig. 3.6 Calculated threshold current density for the fundamental mode, in the case of a p-n junction at x=0, as a function of the width.

predominantly in the fundamental mode.

The relative degree to which various lateral modes are preferred or discriminated against can be quantitatively expressed by the modal gain γ_m:

$$\gamma_m = \frac{n_0}{c} \times \frac{\int_{-W}^{+W} A\Delta(x) S_m(x)\, dx}{\int_{-W}^{+W} S_m(x)\, dx} \tag{12}$$

where c/n_0 is the group velocity of the region, $\Delta(x)$ is the excess carrier density profile, and $S_m(x)$ is the intensity profile of the mth mode. In principle, $\Delta(x)$ can be obtained, from equations 3 and 4, only when the lasing amplitudes of all the transverse modes are known. As a first order approximation, with the diffused junction located at the center of the waveguide, we can assume that lasing occurs predominantly in the fundamental mode and proceed to solve for $\Delta(x)$ from equations 3 and 4. The resulting carrier distribution $\Delta(x)$ can then be used in equation 12 to calculate the gain γ_m of the higher order modes. The values of the γ_m thus obtained will be an indication of the stability of the lasing in the fundamental mode. The results are shown in figure 3.7, in which the modal gain γ_m is plotted as a function of the injection current density J for different modes. From the figure, it is observed that the first order mode($m=1$) and the third order mode($m=3$) are discriminated against as J increases while the second order mode($m=2$) is not much affected. This results in the increasing tendency of the fundamental mode to operate as the injection current is increased. This behavior has not been observed in the other laser structures. In some structures, such as the channeled substrate laser [5], gains of higher order modes approach that of the fundamental mode as the injection level is raised.

Case 2: In case of a p^+-n junction, the same parameters are used as in Case

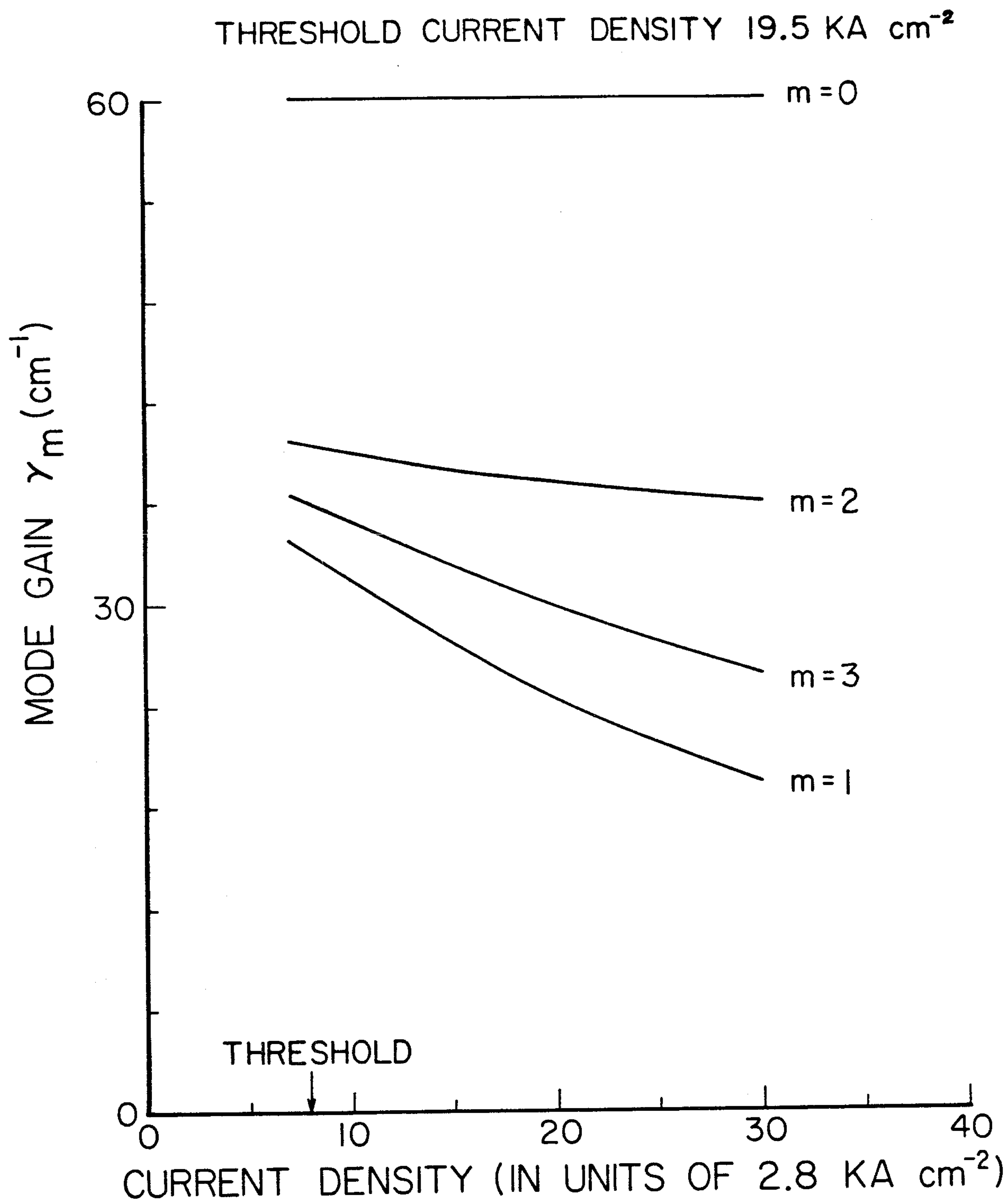

Fig. 3.7 Calculated modal gains for the first four modes, as a function of current density.

1 above, except that the ratio of the diffusion coefficient on the p side to that on the n side is taken to be 2.25. The acceptor concentration N_A takes the value of $1x10^{19}cm^{-3}$. Again, assuming lasing in the fundamental mode (m=0), the carrier density profiles shown in figure 3.8 are for different injection current densities. Since the diffusion length is longer on the p side in this case compared to that in the case of a p-n junction, the electron is more confined on the p side in this case. This results in threshold current density reduction, as mentioned in Case 1. Intuitively, an increase in diffusion length is equivalent to a decrease in the effective waveguide width. Furthermore, the modal behavior in the present case can be understood from the reduction of effective waveguide width on the p-side. Thus, when the junction is on the negative x side, the situation is closer to that shown in figure 3.4; and when the junction is on the postive x side, the situation is like that of a p-n junction (figure 3.3), with the width of the waveguide on the p side replaced by the effective width. Therefore, at equal distance from the middle, the threshold will be higher when the junction is on the negative x side than when it is on the positive x side. Other features, such as the threshold current density as a function of the waveguide width, the mode discriminating behavior, and the mode stabilization behavior, are similar to that in case 1 above. This is expected, because as the injection level increases, these two cases become increasingly similar.

The above analysis indicates that a substantial improvement in mode stabilization can be achieved in lasers with lateral injections. This is demonstrated by the fabrication of a new laser structure -- the Groove Transverse Junction Stripe (TJS) Laser [6,7].

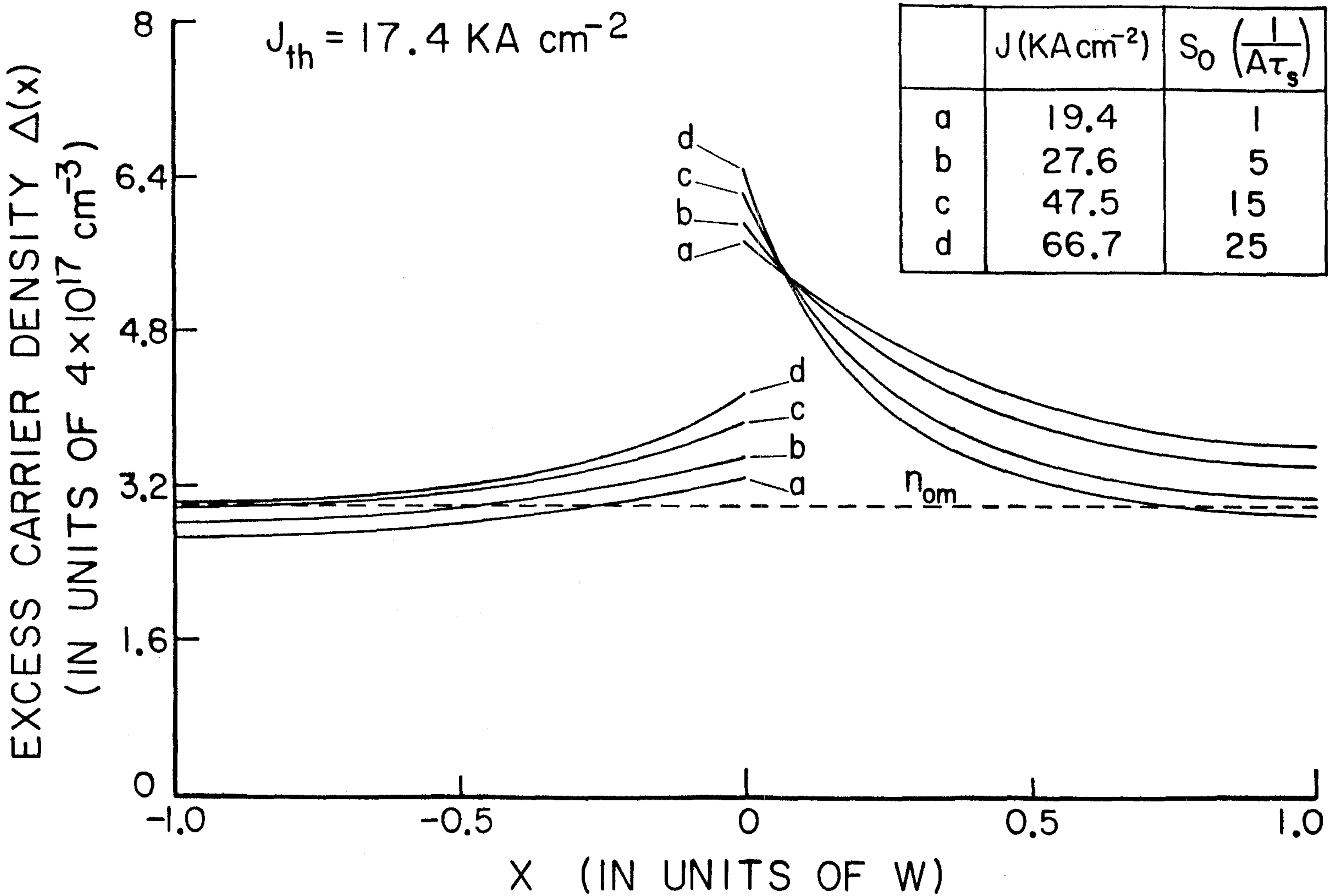

Fig. 3.8 Calculated excess carrier density profiles for a p^+-n junction at x=0.

3.3 Lasers with lateral diffused junctions—Experiment I

3.3a Groove TJS Lasers

The Groove TJS Laser consists of a three epitaxial n-type layers (double heterostructure) grown inside a groove channel on a semi-insulating substrate, and a lateral Zn diffused region, as shown in figure 3.9. The current flows laterally from the p-type region across the junction to the n-type region above the groove. As the quaternary layer has a narrower bandgap than the InP, current leakage through the InP-InP homojunction is small, thus the carriers injection occurs predominantly in the quaternary layer. Current leakage through the SI material is very small due to the high specific resistivity of the SI substrate. Optical confinement is obtained by the geometrical structure of the crescent shaped quaternary waveguide (see Chapter 2). As a result, a low threshold current can be obtained.

The substrate preparation for this laser before epitaxy is the same as that described in section 2.4. Instead of growing vertical junction type layers (p-InP, quaternary, and n-InP are layers) inside the dovetail shaped groove channels, three n-type LPE DH layers are grown during epitaxy. The layers are: undoped InP (n type, $4{-}9\text{x}10^{16}\text{cm}^{-3}$), undoped quaternary InGaAsP (0.1-0.3 μm) and n^+-InP ($2\text{x}10^{18}\text{cm}^{-3}$, Sn doped), respectively. After epitaxy, a Zn diffusion is performed at 640 °C for 20-30 minutes. The Zn diffuses laterally for a distance of 4-6 μm in the SI InP and penetrates laterally the groove quaternary layer to form a p-n junction. Figure 3.10 shows a photograph of a laser with the Zn diffusion front.

It is interesting to note that two diffusion fronts are observed in the semi-insulating substrate while only one front is observed in the n-layers. The shallow front corresponds to carrier density of $10^{17}{-}10^{18}\text{cm}^{-3}$, while the deep front

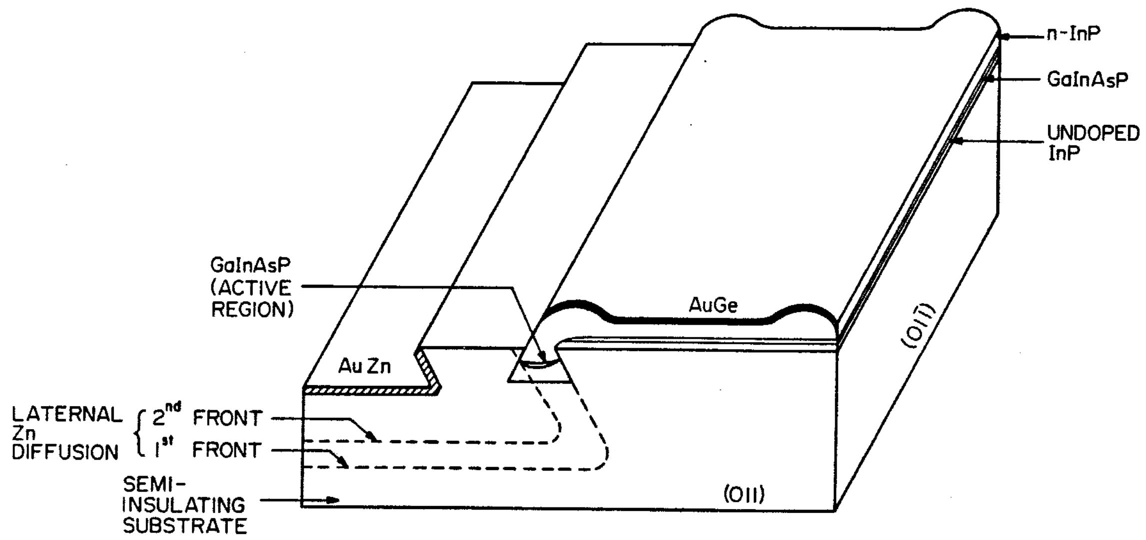

Fig. 3.9 A schematic diagram of a Groove TJS Laser with Zn diffusion touching the active region.

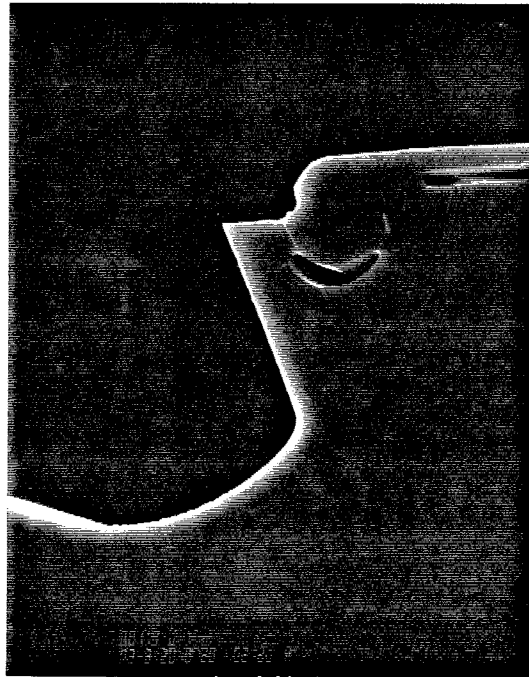

Fig. 3.10 A photomicrograph of a Groove TJS Laser showing the diffusion fronts.

corresponds to carrier density of $10^{15}cm^{-3}$ or below. As a result, two fronts are observed in the SI InP which has very low carrier concentration and only one front is observed in the n-layers which are doped above $10^{16}cm^{-3}$. Depending on the position of the diffusion front inside the upper n^+-InP layer, different laser threshold currents are obtained. For diffusion front just touching the active region (see figures 3.9,3.10), the lowest threshold current obtained per unit active region width is 5 mA/μm for lasers with cavity length of 300 μm and active region thickness of ~ 0.2 μm. When the diffusion front is in the middle of the active region inside the groove (see figure 3.11), the lowest threshold current obtained per unit width is 10 mA/μm for lasers with the same cavity length and active layer thickness. Noting that when the diffusion front just touches the active region, the area of the high doping InP homojunction is small and when the diffusion front is in the middle of the active region, a large area p-InP/n^+-InP junction above the active region results (see figure 3.11), the increase in the laser threshold current may be explained by the carrier leakage across the InP homojunction.

The light output versus current characteristics of one of the lasers is shown in figure 3.12. The laser threshold current is 13 mA, with a cavity length of 300 μm. The lowest threshold current obtained is 12 mA. Room temperature CW operation of the lasers is obtained with threshold current as low as 15 mA. A 2000 hours lifetime test has been carried out on this laser and no output degradation has been observed. The lasers emits at 1.3 μm in wavelength. The external differential quantum efficiency of these lasers is about 30-40% for both facets.

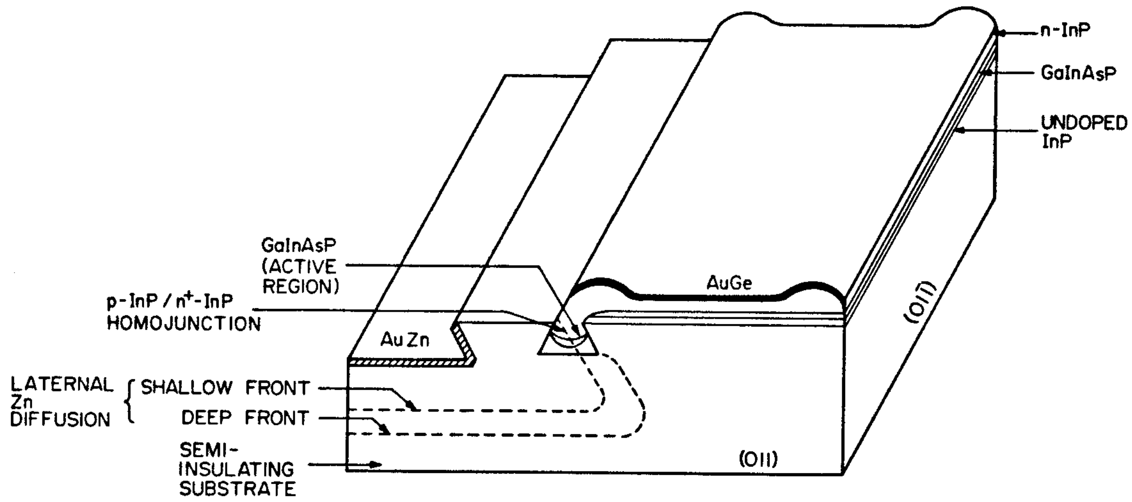

Fig. 3.11 A schematic diagram of a Groove TJS Laser with the diffused junction near the center of the waveguide.

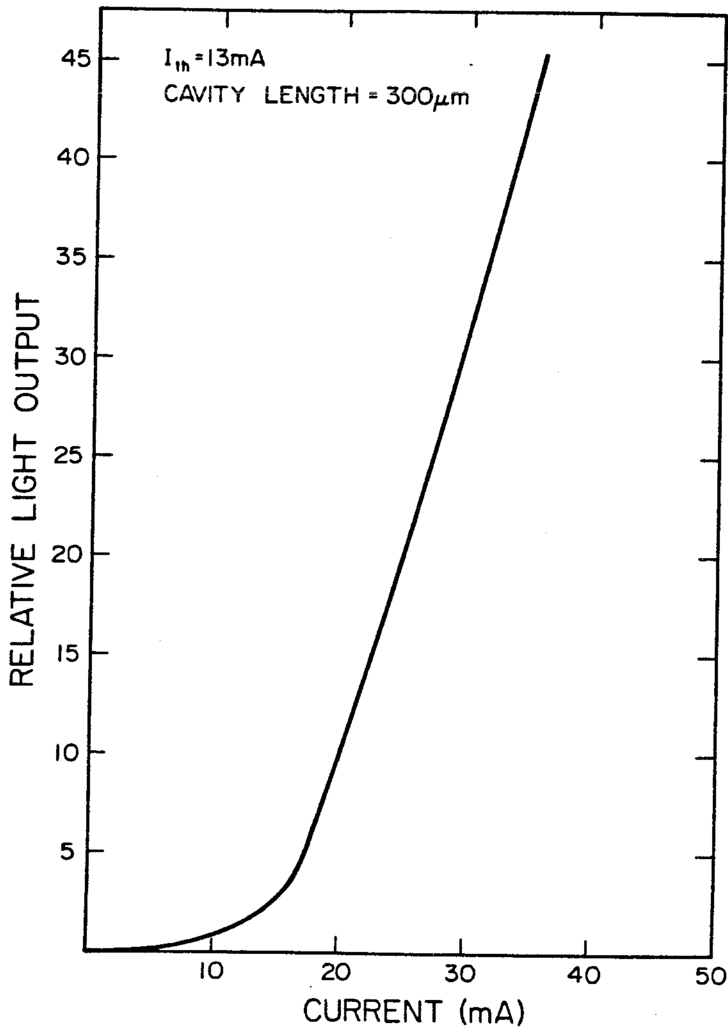

Fig. 3.12 L-I characteristics of a Groove TJS Laser.

3.3b Comparision with theory

Depending on diffusion depth, the resulting lateral junction will be a p-n junction or a p^+-n junction. The active region width is 3-5 μm and the thickness is $\sim 0.5-1 \mu$m at the center of the active region. The lasers are tested with 50 ns current pulses having a repetition rate of 1 kHz. Stable lateral mode operation is achieved up to 45 times threshold current, when the Zn diffusion front is placed somewhere near the middle of the active region, with a maximum power of 245 mW/facet. Figures 3.13 shows a far field pattern of a laser with diffusion front in the middle. The lasers are operated with current pulses having a width of 50 ns and a repetition rate of 1 kHz. The fact that the spatial mode profile does not change significantly as the power output is increased is a proof of the stabilization effect at all power levels. Most of the lasers with junction at the middle of the waveguide, operate in a single longitudinal mode up to to 1.2-1.4 times threshold current. However, some of the lasers operate in a single longitudinal mode to 2-3 times threshold current. Figure 3.14 shows the spectra of the laser whose far field is shown in figure 3.13. Single longitudinal mode operation is maintained up to twice the threshold current. When the diffusion front is near the active region edge, higher order transverse modes are observed; figure 3.15 shows a typical multi-mode far field pattern of such a laser. It is also observed that an increase in active region width results in a slight increase in the threshold current density, in qualitative agreement with the numerical results described in section 3.2c.

3.4 Lasers with lateral diffused junction—Experiment II

3.4a Terrace TJS Lasers

Like the Groove Lasers, the Terrace TJS Lasers [8] are grown on semi-

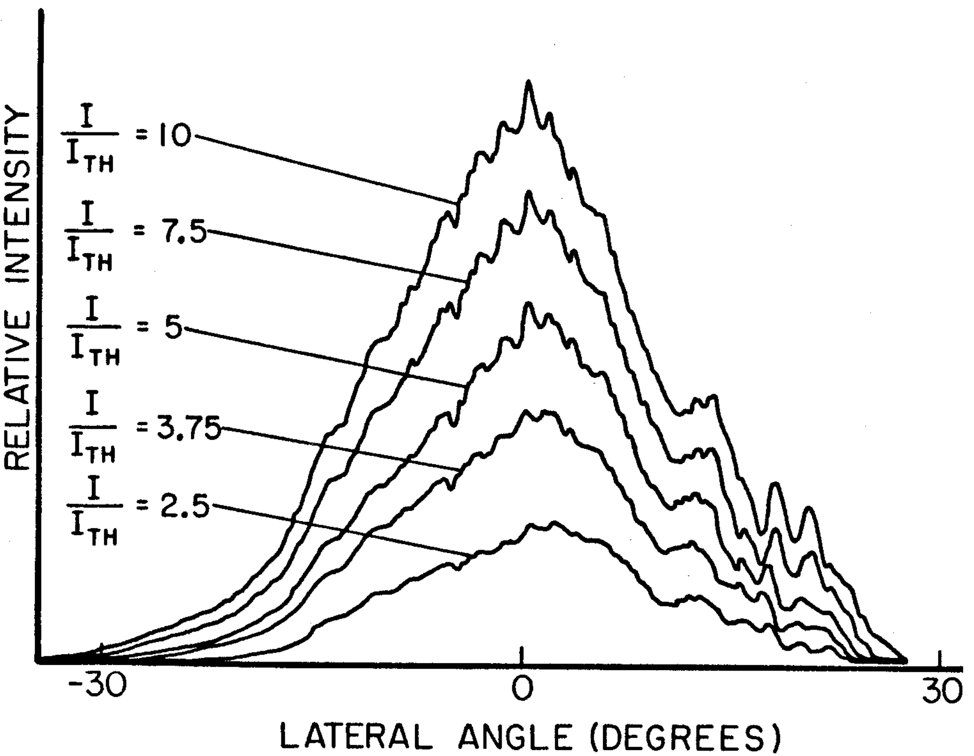

Fig. 3.13 Far field patterns of a Laser with junction at waveguide center, at different injection levels.

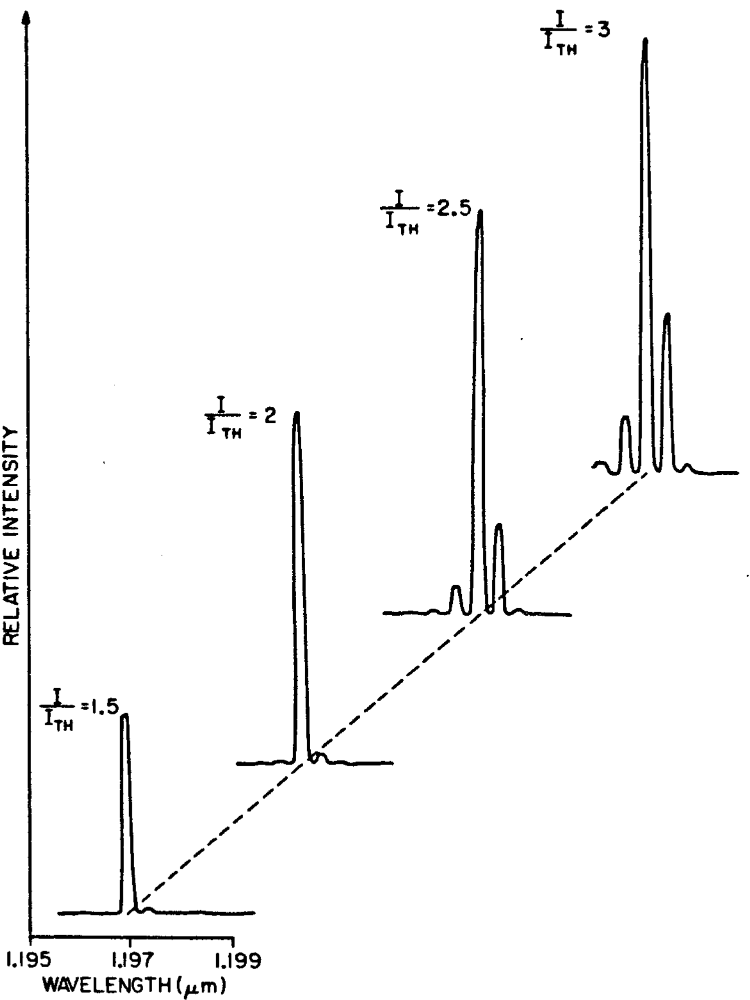

Fig. 3.14 Spectra of the same laser at different injection levels.

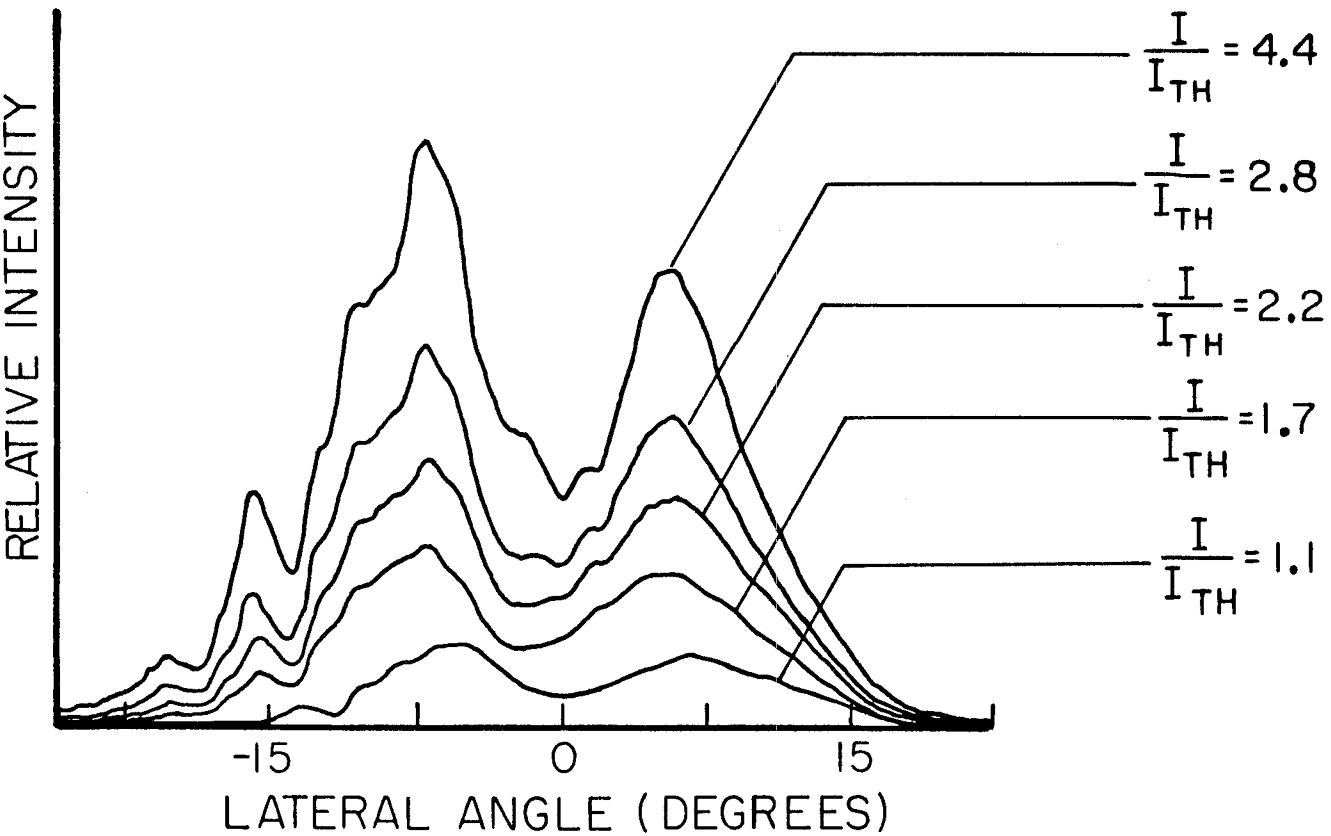

Fig. 3.15 Far field patterns of a Groove TJS Laser with lateral diffused junction touching the active region.

insulating InP to optimize current confinement while retaining some of the original SI surface for fabricating other devices. The fabrication of the Terrace TJS Lasers is similar to that of the Terrace Laser with vertical junction (section 2.5). A schematic diagram of the laser is shown in figure 3.16. The DH layers are identical to that of the groove lateral junction lasers, and with similar layer doping levels. The typical layer thicknesses are : (n-InP) 0.5 μm, (InGaAsP) 0.2-0.3 μm at the thickest part, (n^+-InP) 2-3 μm. Again, after epitaxy, a Zn-diffusion is performed laterally with the diffusion front penetrating the active region to form a lateral p-n junction. The current flows laterally from the contacts to the junction plane where carrier injection occurs. The carrier injection in this case occurs predominantly across the lower bandgap InGaAsP homojunction. For this particular structure, the forward bias leakage of carriers across the InP-InP junction is minimized, as part of the wall of the terrace is still semi-insulating and the thin InP layers reduce the InP-InP homojunction area resulting in good current confinement. As mentioned in section 2.5, the active layer thickness variation leads to a lateral effective refractive index tapering, which provides the necessary index-guiding for optical mode confinement. Lasers with the transverse junction placed 1-1.5 μm away from the edge of the active layer and with 250 μm cavity length have threshold current in the 50-80 mA range. The light output increases linearly with the injection current at up to four times threshold current. External differential quantum efficiency is about 38 % for both facets. Fundamental mode operation of the lasers is achieved with the diffused junction located near the thickest part of the waveguide, as predicted above. A far field pattern of the laser is shown in figure 3.17, where the laser threshold current is about 60 mA. Stable fundamental mode operation is seen to be maintained up to very high injection($\sim$ 10 times threshold current). The laser is capable of delivering moderately high output power, a peak optical out-

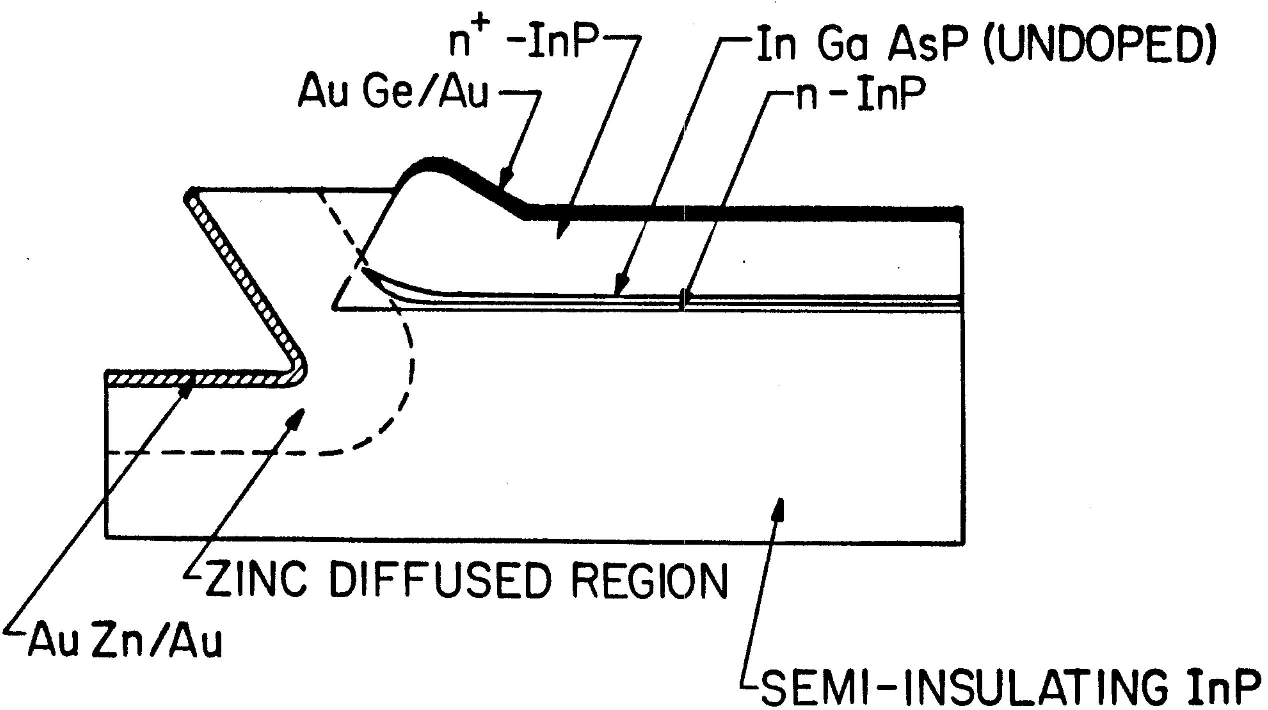

Fig. 3.16 A schematic diagram of a Terrace TJS Laser.

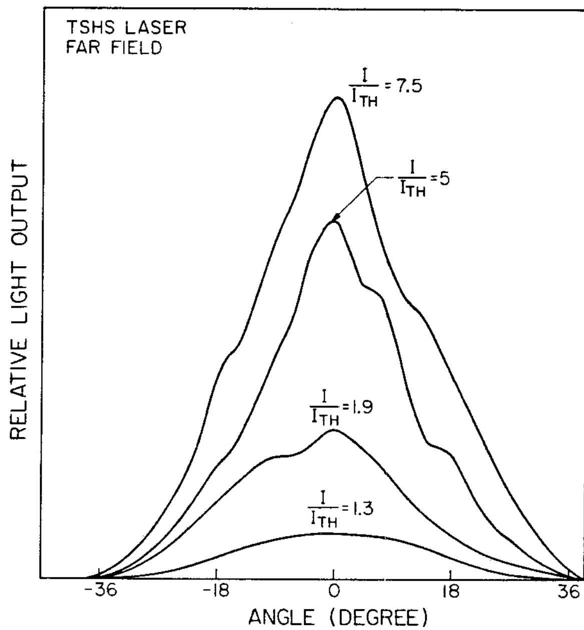

Fig. 3.17 Far field patterns of a Terrace TJS Laser.

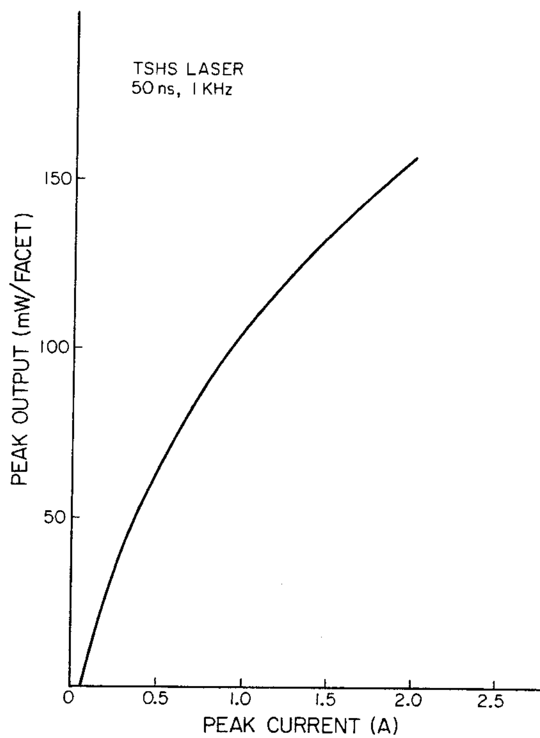

Fig. 3.18 Peak output power versus current characteristics of a Terrace TJS Laser.

put power versus injection characteristics is shown in figure 3.18, with the specified testing condition.

3.5 Conclusion

In conclusion, we have studied the gain stabilizing behavior of waveguides with lateral carrier injection. The finite width of the real index guided waveguide, as compared to the carrier diffusion length, together with the boundary conditions, results in the lateral carrier confinement within a small region about the quaternary p-n junction. As the current injection increases, the optical power increases, the gain profile becomes progressively narrower due to the decrease of the stimulated lifetime. Stabilization for the fundamental mode is obtained when the transverse junction is placed near the middle of the waveguide. These results are in good agreement with experimental observations in which the Groove and Terrace InGaAsP/InP lasers with a lateral junction show a remarkable persistence in the fundamental lateral mode operation.

Appendix 3-1 : Computational scheme solving steady state rate equations with known mode profiles

We divide the waveguide into h regions, with the width w_k in the kth region, where k=1,...,h. Next, taking S(x) as given by equation 1, as a constant in each region, we can solve equations 3,4 for the excess carrier density. Thus, in the kth region:

$$\Delta_k(x_k) = A_k e^{-\frac{x_k}{L_k}} + B_k e^{\frac{x_k}{L_k}} + C_k \qquad 0 \le x_k \le w_k \tag{A-1}$$

where

$$L_k = \frac{L}{\sqrt{1 + S_k A \tau_s}}$$

$$C_k = \frac{A n_{om} S_k L_k^2}{D_{eff}}$$

L is the diffusion length in that region, and L_k is the effective diffusion length in the presence of the photon intensity profile.

The coefficients A_k, B_k are determined by matching boundary conditions at $x_k = w_k$:

$$A_k = \frac{e^{-\frac{w_k}{L_k}}}{2}(A_{k+1}(1 - \frac{L_k}{L_{k+1}}) + B_{k+1}(1 + \frac{L_k}{L_{k+1}}) + C_{k+1} - C_k \tag{A-2}$$

$$B_k = \frac{e^{\frac{w_k}{L_k}}}{2}(A_{k+1}(1 + \frac{L_k}{L_{k+1}}) + B_{k+1}(1 - \frac{L_k}{L_{k+1}}) + C_{k+1} - C_k$$

$$A_h = B_h e^{\frac{-2w_h}{L_h}} \tag{A-4}$$

$$A_1 = B_1 \tag{A-5}$$

Defining $B_h = K_1$, $B_1 = K_2$, using the recurrence relations (A-2) and (A-3), coefficients $A_h, A_{h-1}, B_{h-1}, \ldots$ can be calculated a linear function of K_1. Similarly

A_1, A_2, B_2 can be calculated as a linear function of K_2. By matching the junction boundary condition at x=a, which for the case of a p-n junction, (as given by equation 10) gives,

$$K_2 = c_1 K_1 + c_0 \tag{A-6}$$

and for the case of a p^+-n junction, (as given by equation 11) results in,

$$K_2 = d_2 K_1^2 + d_1 K_1 + d_0 \tag{A-7}$$

where c_1, c_0, d_2, d_1, d_0 are determined from computation. Once K_1 is known, all the A's and B's can be determined. To find K_1, we go back to equation 4, which now takes the form:

$$\sum_{k=0}^{h} S_k w_k \left(\frac{1}{A\tau_f} - C_k + n_{om} \right) = \sum_{k=0}^{h} S_k L_k \left(A_k \left(1 - e^{-\frac{w_k}{L_k}} \right) + B_k \left(e^{\frac{w_k}{L_k}} - 1 \right) \right) \tag{A-8}$$

The left side of equation A-8 is constant once S_k is given, the right side is a linear function of K_1 if equation A-6 is used, or a quadratic function of K_1 if equation A-7 is used. In both cases K_1 can be found and thus the carrier density profiles can be computed.

Appendix 3-2 : Validity of the real-index guiding assumption

The validity of the analysis in section 3.2 rests on the assumption that the spatial mode is index-guided and is independent of the injection level. Under high level injection, however, the localization of carriers near the junction provides a gain-guiding mechanism so that a combination of index and gain guiding can take place. Gain guiding may thus become increasingly dominant at very high-level injection and in the case of a very wide waveguide. The analysis is valid when the width of the optical mode guided by the gain profile is much wider than that guided by the real-index waveguide, which is approximately equal to half of the width of the waveguide. For a rough estimate of the width of the gain-guided mode, the exact shape of the gain profile is not important and one can use the result for the approximate fundamental width x_m in the case of a gaussian gain profile [9]:

$$g(x) = g_0 e^{\frac{-x^2}{L^2}} \tag{A-9}$$

$$x_m = 2\left(\frac{\lambda L}{2\pi}\right)^{\frac{1}{2}}\left(\frac{g_0 \lambda n}{\pi}\right)^{-\frac{1}{4}} \tag{A-10}$$

where λ is the free space wavelength, L is the diffusion length, $g(x)$ and g_0 are in cm^{-1}, and n is the effective refractive index of the medium. One can use the values of the peak gain and half width of the gain profile obtained in the above section in equation A-10 and determine x_m. The results described in the preceding sections cease to be valid when $x_m \leq W/2$. If one limits the widths of the waveguide to less than 5 μm and assuming diffusion length is 2 μm, one can estimate from equation A-10 that index-guiding is the dominant mechanism for a peak gain as high as 1000 cm^{-1}, which corresponds to a pump current J density of about 90 KA cm^{-2}. This sets an upper limit on the range of validity of the analysis in section 3.2.

In the analysis, we have also, for simplicity, neglected the effect of evanescent waves outside the guide. This is justified since the inclusion of evanescent waves will result in an even smaller gain for the higher order modes and therefore will only improve further the stabilization of the fundamental mode.

References

1. S. Wang, C. Y. Chen, A. S. Liao and Figueroa, IEEE J. Quant. Electron., QE-17, pp. 453-468, (1981).
2. G. H. B. Thompson,'Physics of Semiconductor Laser," John Wiley and Sons (1980).
3. K. L. Yu, K. Y Lau, S. Margalit, U. Koren, T. R. Chen, and Amnon Yariv, IEEE J. Quant. Electron., QE-19, pp. 426-432, (1983).
4. N. H. Fletcher, Proc. I.R.E., vol 45, pp. 862-872, (1957).
5. D. P. Wilt and A. Yariv, IEEE J. Quant. Electron., QE-17, pp. 1941-1949, (1981).
6. K. L. Yu, U. Koren, T. R. Chen, and A. Yariv, IEEE J. Quant. Electron., QE-18, pp. 359-361, (1982).
7. T. R. Chen, U. Koren, K. L. Yu, K. Y. Lau, L. C. Chiu, A. Hasson, S. Margalit. and A. Yariv, Appl. Phys. Lett., vol 41, pp. 225-228, (1982).
8. T. R. Chen, K. L. Yu, U. Koren, A. Hasson, S. Margalit. and A. Yariv, J. Appl. Phys., vol 53, pp. 426-432, (1982).
9. K. Y. Lau and A. Yariv, J. Appl. Phys., vol 52, pp. 641-645, (1981).

Chapter 4

Carrier Leakage and Temperature Dependence of InGaAsP Laser threshold current

4.1 Introduction

A problem of quaternary InGaAsP/InP light-emitting diodes (LEDs) and lasers is the severe output power saturation of the LEDs and the high temperature sensitivity of the laser threshold current in contrast with GaAlAs/GaAs lasers. Threshold current of quaternary lasers, empirically found to vary with temperature T as $I_{TH} \sim e^{T/T_o}$, is characterized by $T_o \sim$ 70–90 °K for quaternary lasers which is lower than that of GaAlAs/GaAs lasers ($T_o \sim$ 120 ° K). This is generally accepted to be caused by the material properties of the InGaAsP/InP system such as non-radiative Auger recombination. However, this fact alone cannot account for the abnormally low T_o (40–60 °K) observed in some lasers [1], and it cannot fully explain the output power saturation in LEDs. Carrier leakage over the hetero-barrier has been suspected to be responsible for these behaviors. Experimental studies have shown the existence of significant carrier leakage over the hetero-barrier in 1.3 and 1.5 μm LEDs [2-4] whereas leakage can only be inferred indirectly for lasers [5,6]. A direct measurement of the electron and hole leakage current in InGaAsP/InP lasers is extremely desirable as it enables the investigation of the origin of the leaked carriers that may lead to ways whereby higher T_o can be achieved.

4.2 Experimental measurement of the carrier leakage

4.2a The laser-bipolar-transistor structure for leakage measurement

A schematic representation of the laser-bipolar-transistor used in this work [7] is shown in figure 4.1. The composition and the thickness of the four epitaxial layers are: n^+-InP collector layer (Sn doped, n= $2\times10^{18}cm^{-3}$, 3-4 μm thick), p^--InP confining layer (Zn doped, p= $2\times10^{17}cm^{-3}$, 1.5 μm thick), InGaAsP active layer (n= 4-9 $\times$ $10^{16}cm^{-3}$, 0.2 μm thick) and n^+-InP confining layer (Sn doped, n= $2\times10^{18}cm^{-3}$, 4 μm thick). The last three layers constitute a typical DH InGaAsP/InP laser [8,9]. The emitter-base junction (see figure 4.1) works as in an ordinary laser diode. The collector-base junction is reverse biased, as in a bipolar transistor, to collect the leakage current. The n^+ layer is used to collect electron leakage current. After growth, selective etching was performed on the top n^+-InP layer with the resulting mesa structure formed as shown in the left part of figure 4.1. In order to achieve low threshold current, the quaternary layer was undercut with a selective etchant to reduce the width. Part of the wafer was etched down to the bottom n^+-InP to facilitate the fabrication of the collector contact as shown in the right part of figure 4.1. Finally, three electrical contacts were made respectively for the emitter, base and collector of the n-p-n bipolar transistor.

This particular DH structure has very good lateral current confinement as the active layer of the laser is bounded on the sides by semi-insulating InP and air respectively; the current leakage due to carrier bypassing the active region through the burying layer, as is the case in some conventional heterostructure lasers, is completely eliminated. This enables us to measure directly the current leakage over the hetero-barrier.

Under forward bias, the emitter-base junction acts as a laser diode. The elec-

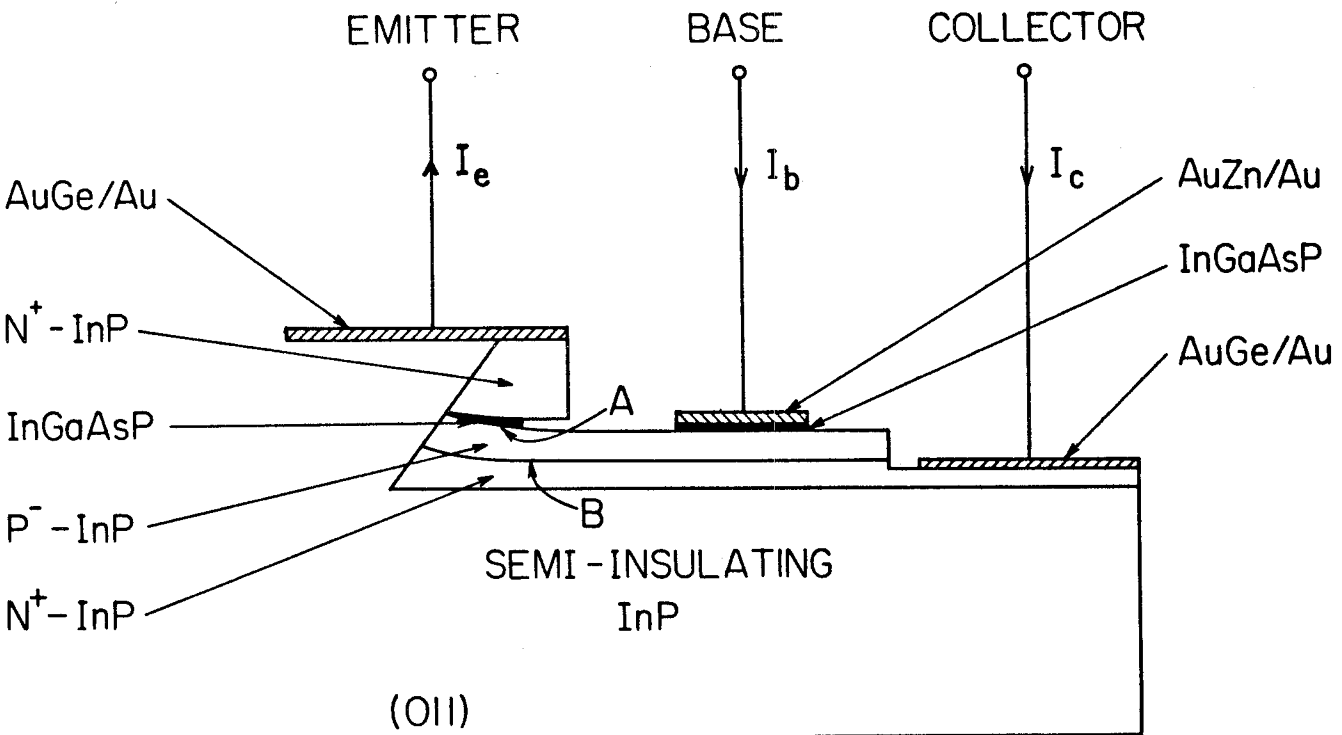

Fig. 4.1 A schematic diagram of the Laser-bipolar-transistor structure.

trons are injected from the n^+-InP (emitter) to the quaternary region. In this structure, those electrons, which have surmounted the hetero-barrier at (A) (see figure 4.1) and arrived at the base-collector junction (B), will be swept out by the electric field in the reverse biased junction. As the p^- layer thickness is smaller than one electron diffusion length ($\sim$3-4 μm), most of the leakage minority carriers will be collected, thus giving rise to I_C.

The turn-on voltage of the laser junction is about 0.7 V and the reverse breakdown voltage of the collector junction is about 8-9 V (defined at 0.5 mA reverse current, somewhat arbitrary). The threshold current of the laser (for an active layer width of $\sim$ 2 μm and a cavity length of 250 μm) ranges from 15-30 mA with the lowest one being 12 mA

4.2b Electron leakage measurement

A block diagram depicting the measurement circuit is shown in figure 4.2a. The base current (I_b), the reverse bias voltage of the collector junction (V_c), the leakage current (I_c) and the light output were simultaneously monitored and measured. The emitter current (I_e) is the total injection current to the laser, I_b is the recombination current that is mostly in the low bandgap p type active layer, and I_c is the leakage current. A phototrace of these currents is shown in figure 4.2b. The general behavior of the collector current versus the collector voltage is shown in figure 4.3. As the reverse bias voltage increases, the collector current also increases and eventually saturates. This saturation occurs when the junction is reverse biased and all the electrons which have overcome the hetero-barrier are collected. Hence, this saturated collector current is just the electron leakage current (assuming negligible carrier loss in the p^--InP layer by recombination process or other processes). It has been found that under low

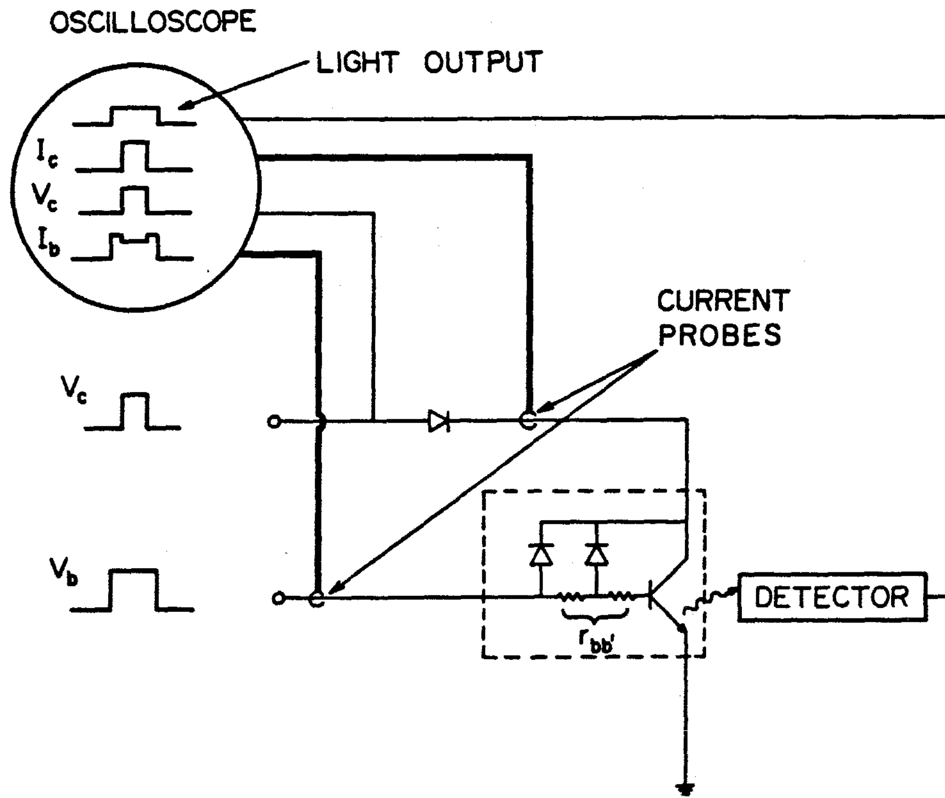

Fig. 4.2a A block diagram of the measurement circuit; $r_{bb'}$ is due to the distributed resistance at the base-collector junction.

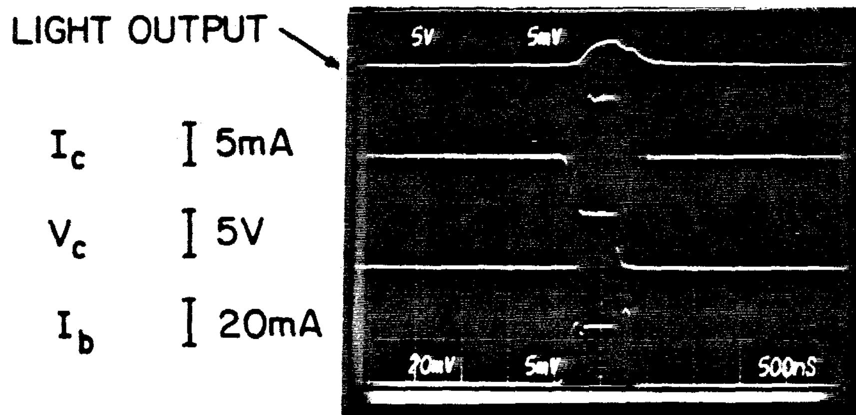

Fig. 4.2b A photograph of the measured signals.

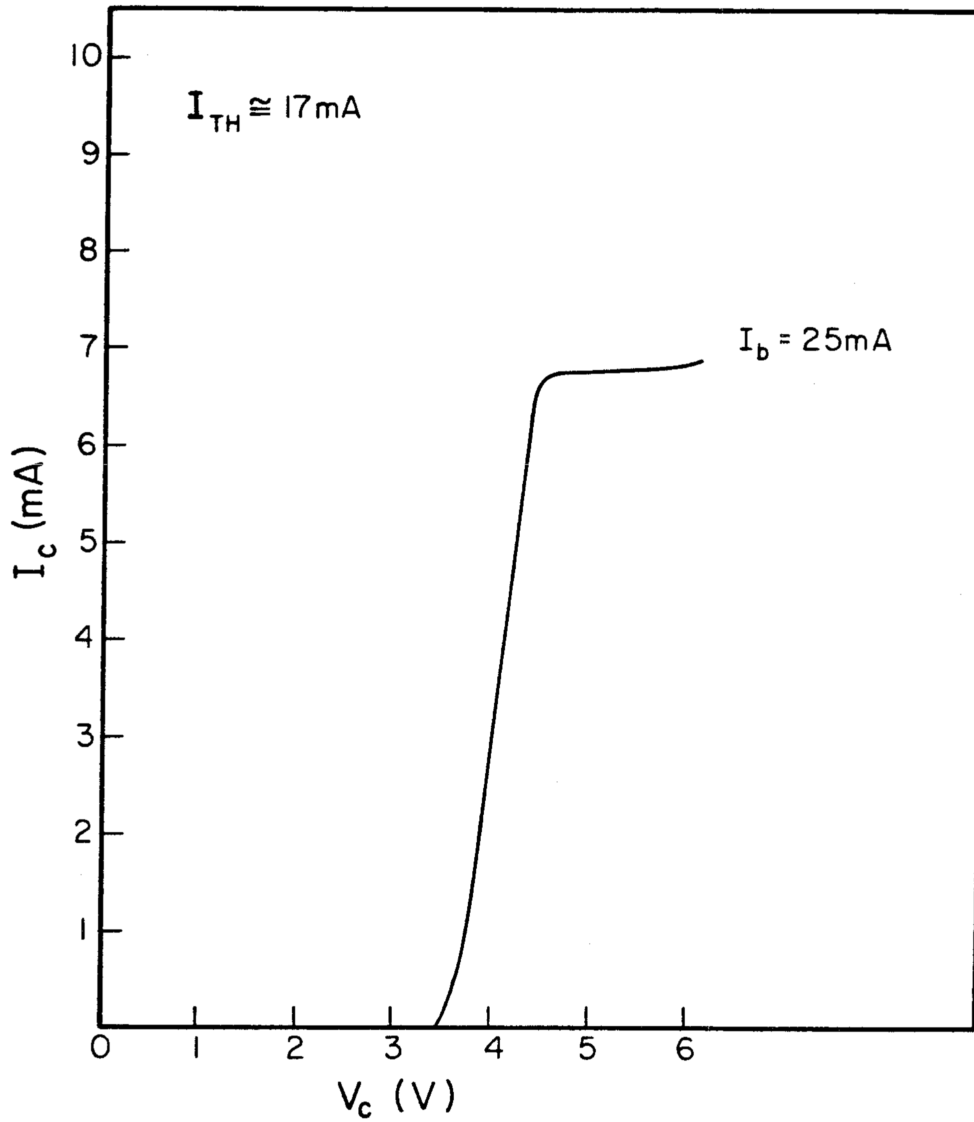

Fig. 4.3 General behavior of the collector current and collector voltage.

injection condition, the electron leakage is very small. However, it increases rapidly with increasing injection. For lasers emitting at 1.2 μm [7] and 1.3 μm [10], the leakage current is about 10-30 percent of the total injection current when the latter is about 20 mA (corresponding to a current density of ~ 4 kA/cm^2, which is near the threshold current density of the lasers). A typical leakage current versus the total injection current (I_e) characteristics is shown in figure 4.4. It is noticed that the leakage current increases with injection current and that no saturation occurs even above threshold; this is discussed in detail in section 4.3.

The leakage current was also measured with a transistor curve tracer. Figure 4.5. shows typical characteristics of the transistor in the common-emitter configuration. As can be seen from figure 4.5, the collector current, which corresponds to the leakage current, increases superlinearly with the base current.

To ensure that this leakage does not result from lateral current leakage flowing through the parasitic junction near the tip of the active layer (figure 4.1), the quaternary layer of some of the lasers were etched away completely. The resulting device was then measured as described above. The results indicate negligible current leakage through this parasitic junction.

4.2c Temperature behavior of electron leakage

Electron leakage current has been measured in the temperature range of 10-32 °C and is found to be highly temperature sensitive. The electron leakage current increases by a factor of 1.4 from 10 °C to 32 °C, when the total injection current is held at 20 mA (see figure 4.6). Direct measurement of the leakage current is used to probe its effect on the temperature sensitivity of the thresh-

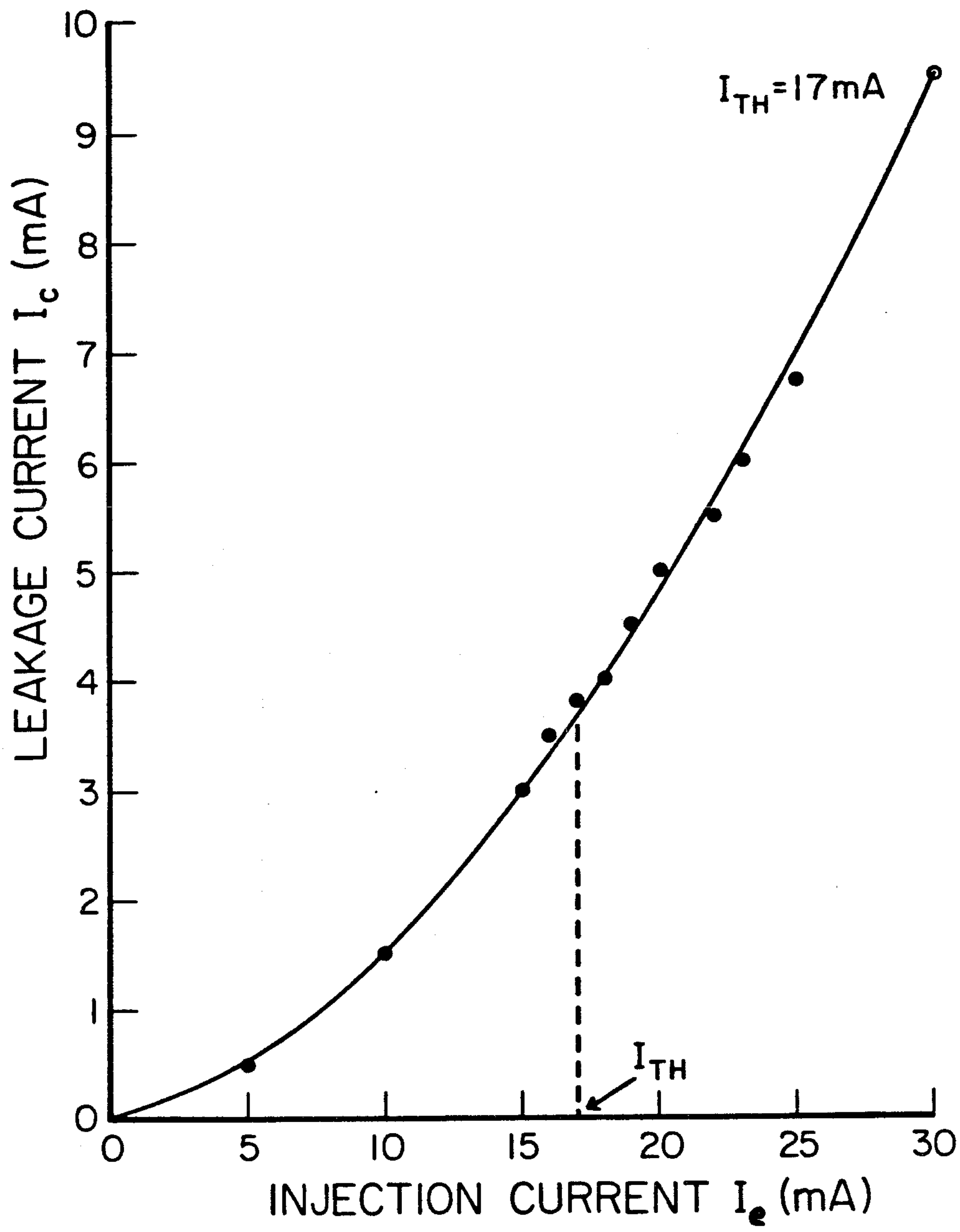

Fig. 4.4 A typical leakage current versus injection current characteristics.

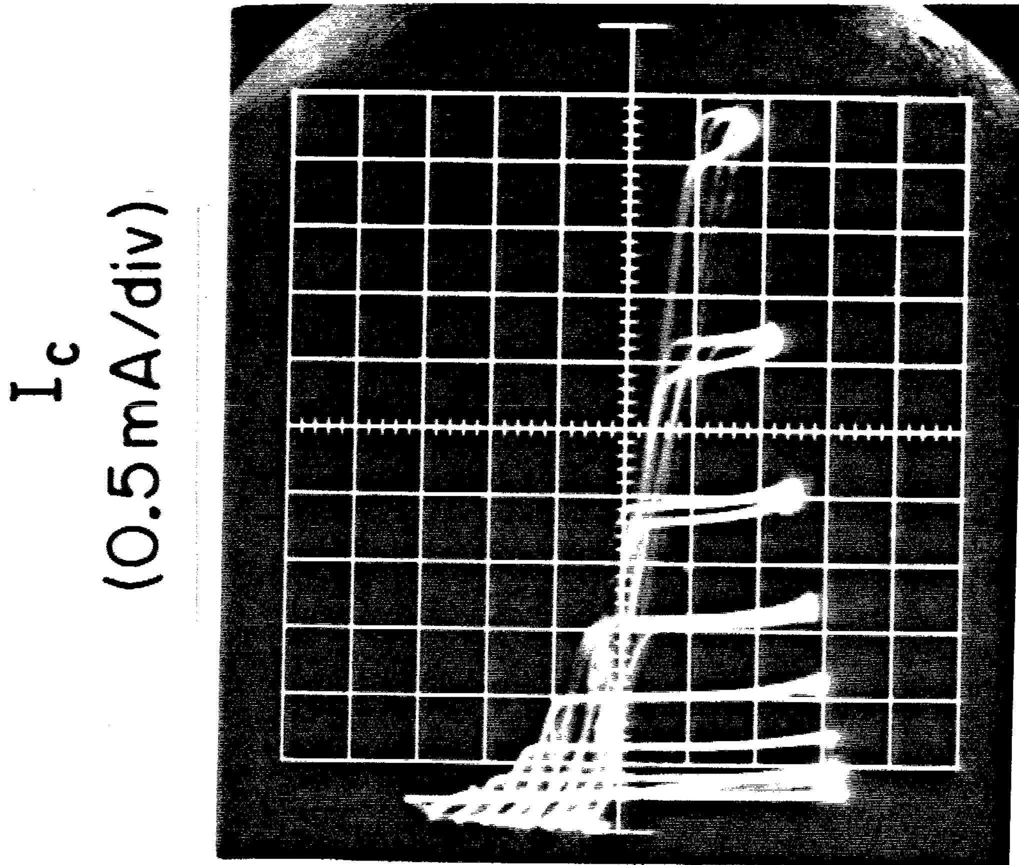

Fig. 4.5 A transistor curve trace of the collector current versus collector characteristics.

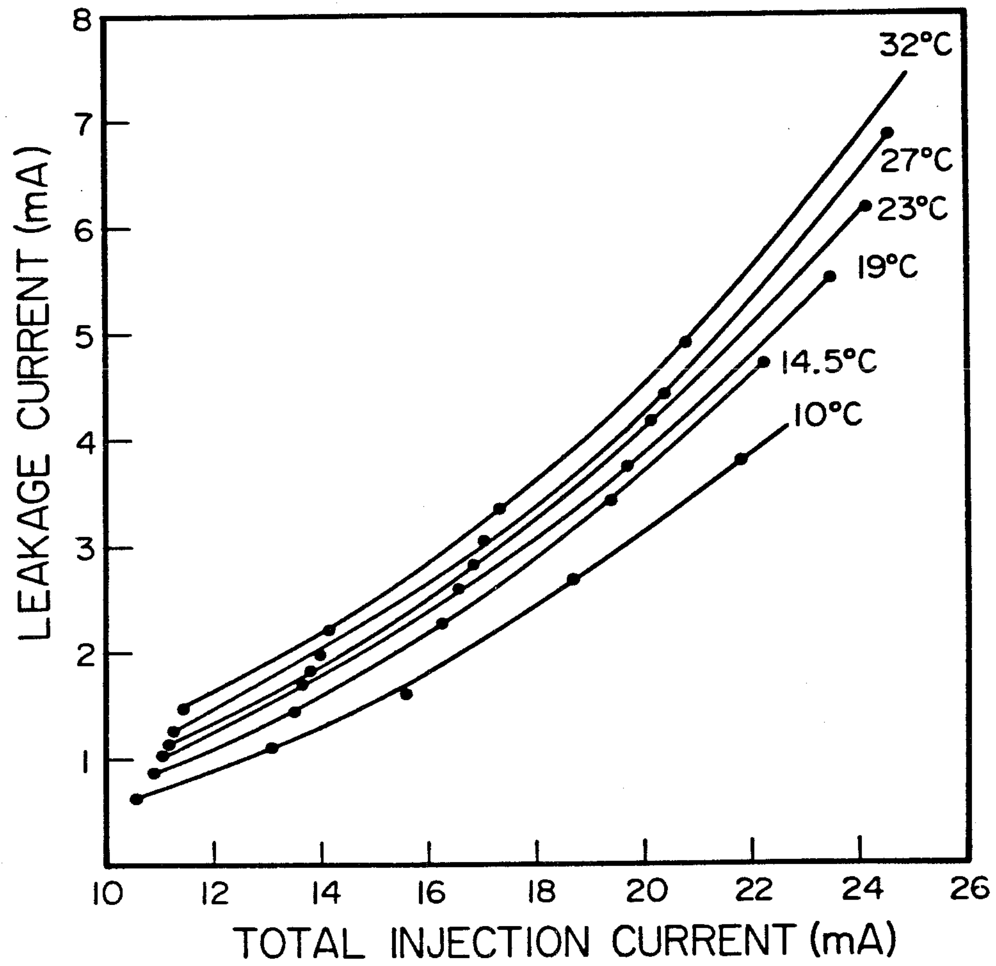

Fig. 4.6 Electron leakage current as a function of total injection current at different temperatures.

old current. Temperature characteristics of an ideal 'leakage-free" laser can be obtained by subtracting, at each temperature, the leakage current from the measured threshold current. The results for a laser with a threshold current of 17 mA (at 23 °C) are presented in figure 4.7. From the threshold current measured at different temperatures, a T_0 of 56 °K is obtained, with the corresponding "leakage free" characteristic temperature T_0' equal to 89 °K. This demonstrates for the first time the effect of leakage current on the temperature sensitivity of quaternary lasers.

4.2d Hole leakage measurement

By changing dopant types on the structure of figure 4.1, we have also successfully fabricated a similar device for measuring the hole leakage. A schematic drawing of the structure is shown in figure 4.8. The composition and thickness of the four epitaxial layers are: p-InP collector (Zn doped, $\sim 4\mu m$), n^+-Inp base (Sn doped, $\sim 0.5-1\mu m$), undoped InGaAsP active layer ($\sim 0.2\mu m$), and p-InP emitter (Zn doped, $\sim 4\mu m$). In contrast to the electron leakage result, no hole leakage current (to within 1% of the total injection current) was detected at the collector junction-- even when the injection current density is over 10 kA/cm^2. We are thus led to the conclusion that hole leakage over the heterobarrier in InGaAsP lasers is negligible.

The null result of the experiment is not surprising, since holes have larger effective mass and the ratio of the mobilities (μ_p/μ_n) is about 0.05, the hole leakage is expected to be at least 400 times less than that of electron leakage.

4.3 Carrier Leakage in Heterojunction—Theory

Hitherto leakage over the heterobarrier was explained by a model postulating thermal excitation followed by diffusion [11]. According to this model, the leak-

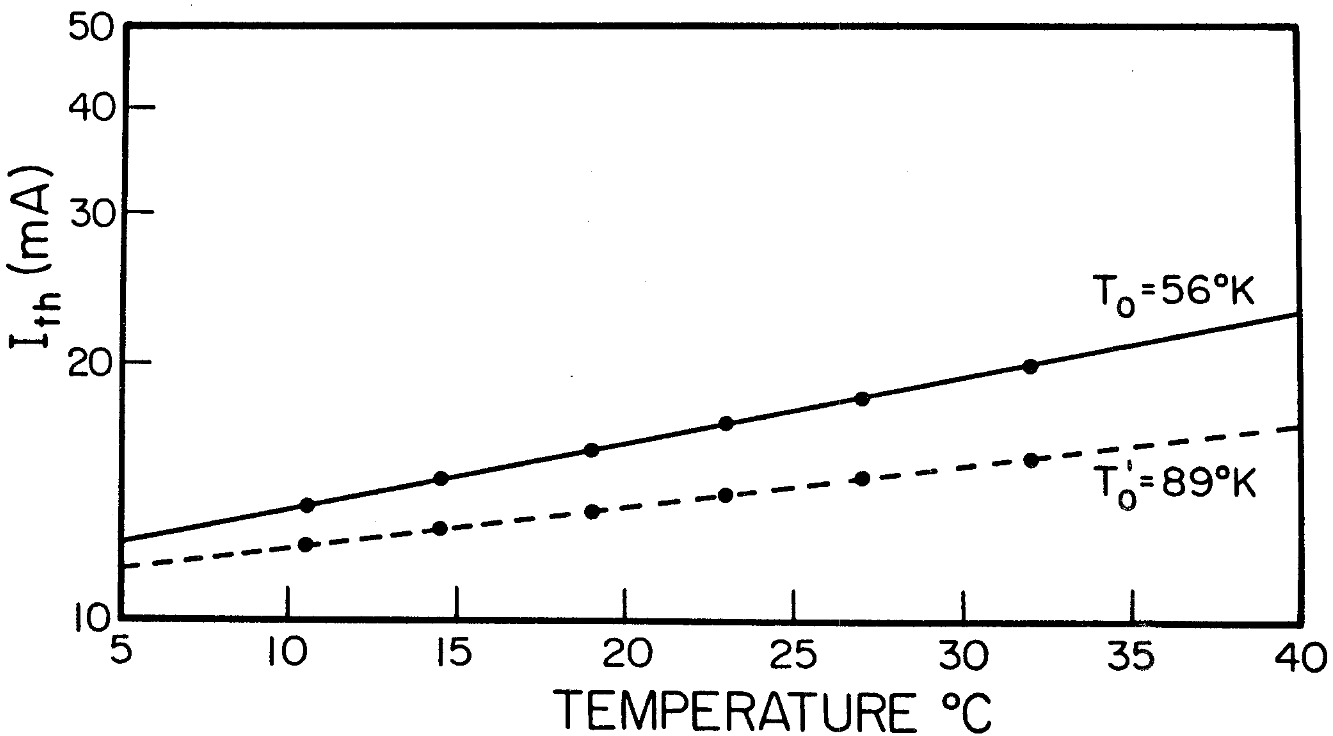

Fig. 4.7 T_o of a Terrace Laser. Solid line shows the conventional temperature characteristics with T_o = 56 °K. Dashed line show the "leakage-free" characteristics with T_o' = 89 °K.

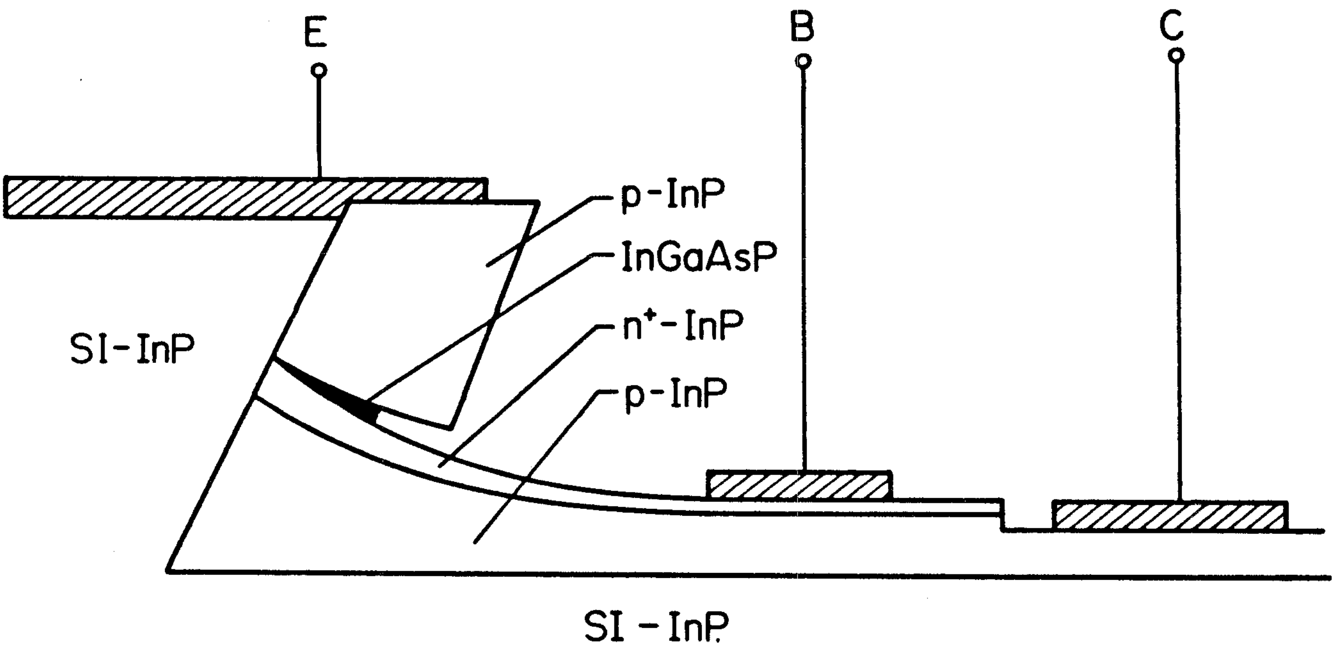

Fig. 4.8 A schematic diagram of the laser-transistor structure for hole leakage measurement.

age current depends on the carrier concentration at the heterojunction. As a consequence, since carrier concentration is clamped above threshold, one would expect the leakage current to saturate above threshold. The apparent discrepancy between theory and experimental results can be resolved if the electric field drift component of the minority carriers (electrons), which has been neglected so far, is invoked. We will show that in the high injection regime where lasers normally operate, the electron leakage current J_e will be proportional to the injected hole current, J_p^{α}, where α is a positive number between 2 and 3. This would result in an "unclamped" leakage current described in sect 4.2. A model [12] is devised in the next section to describe the electron leakage over the heterobarrier which includes the influence of both the electric field and carrier heating effect.

4.3a Field enhanced electron leakage

Under high injection conditions in double heterostructure InGaAsP LEDs and lasers, if the doping level in the p-InP cladding layer is low, it can be shown that there exists a substantial electric field across the InP layer. In such a case, the hole current can be written as

$$\bar{J}_p = q\mu_p N_A \bar{E} \qquad (1)$$

where q is the electric charge, μ_p the hole mobility, N_A the doping level in the p-InP layer, and $\bar{E}$ the electric field strength. For simplicity, only the component tranverse to the junction will be considered. the ratio of the drift and diffusion components of the electron leakage current across the p-InGaAsP--p-InP heterojunction is then given approximately by

$$\frac{J_{drift}}{J_{diff}} \approx \left(\frac{\mu_N}{\mu_P}\right) \frac{L}{qD_N N_A} J_P$$

(2)

where L is the thickness of the cladding layer, and is assumed to be small compared to the diffusion length of the electrons in the P cladding layer, μ_N the electron mobility, and D_N the electron diffusion constant. Taking μ_n=3000 cm^2/V-sec, μ_p=150 cm^2/v-sec, L=1.5 μm, D_N=77 cm^2/sec (at 300 °K), and $N_A=10^{17}cm^{-3}$, it is verified that the drift current is larger than the diffusion current when J_p exceeds ~ 420 A/cm^2. Since normal lasers operate at much higher current densities, it is expected that the drift rather than diffusion current will dominate. Since the drift (leakage) current increases with the field $\bar{E}$, and $\bar{E}$ increases with J_p (see equation 1), it follows that the leakage current continues to grow with current past threshold.

Figure 4.9 shows a band structure at the p-InGaAsP--p-InP hetero-interface at thermal equilibrium. κ, the fraction of the diffusion potential (V_D) on the wide-gap side, is given by [13] :

$$\kappa = \frac{1}{1 + \frac{\varepsilon_2 N_{A2}}{\varepsilon_1 N_{A1}}} \tag{3}$$

where ε is the dielectric constant and the subscripts 1 and 2 denote the low and high gap materials respectively. The hole current under a forward bias V $(=V_1 + V_2, V_2=\kappa V, V_1=(1-\kappa)V)$ is then given by (see Appendix 5-1)

$$J_P = J_{ps}(e^{\frac{qV}{kT}} - 1) \tag{4}$$

with

$$J_{ps} = qN_{A2}v_{r2}\frac{1}{(1 + \frac{v_{r2}}{v_{d2}})}e^{-\frac{qV_1}{kT}}e^{-\frac{\kappa qV_D}{kT}} \tag{5}$$

where

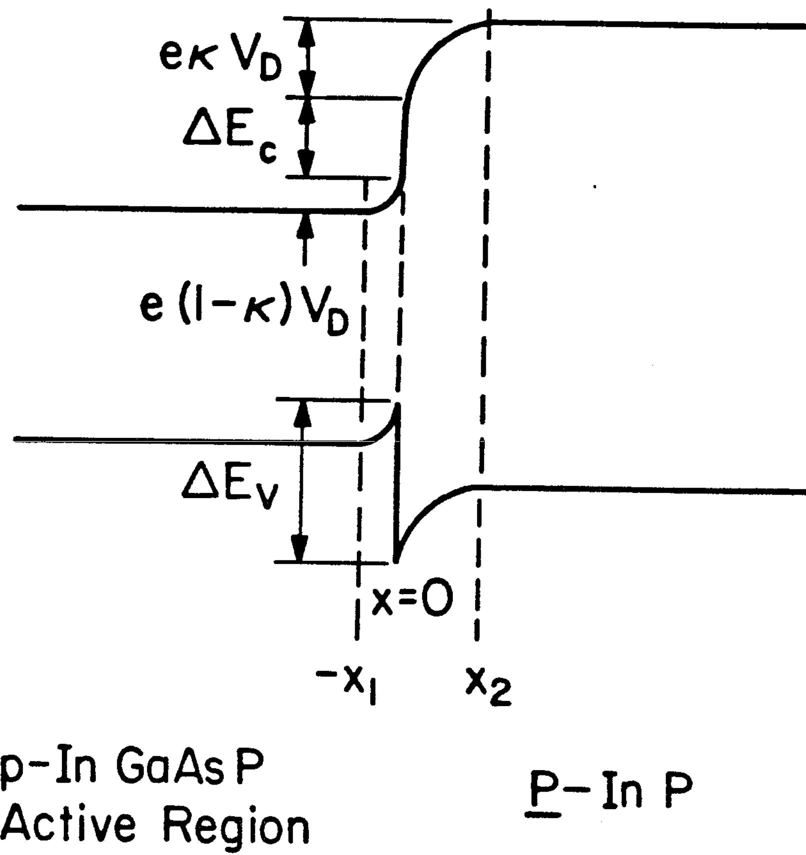

Fig. 4.9 Band structure at the p-InGaAsP--P-InP hetero-interface at thermal equilibrium.

$$v_{d2}^{-1} = \frac{1}{\mu_{p2}kT} e^{\frac{-\kappa q V_D}{kT}} \mathrm{erf}[(\frac{\kappa q V_D}{kT})^{\frac{1}{2}}](\frac{\pi \varepsilon_2 kT}{2N_{A2}})^{\frac{1}{2}} \tag{6a}$$

$$v_{r2} = (\frac{kT}{2m_{2h}\pi})^{\frac{1}{2}} \tag{6b}$$

which are exact analogues of the thermionic-diffusion model of a Schottky barrier [14,15]. In the above, m_{2h} is the hole effective mass and ΔE_v is the discontinuity in the valence band. v_{r2} is the thermal velocity of holes in region 2, and v_{d2} is the effective diffusion velocity associated with the hole transport across the band bending region. The electron concentration at x_2 (figure 4.9) is given approximately by :

$$N_2(x_2) = (\frac{m_{2e}}{m_{1e}})^{\frac{3}{2}} n_1 e^{\sum_1^{i=4} A_i (\frac{n_1}{N_{C1}})^i} e^{-\frac{\Delta E_c}{kT}} e^{-\frac{qV_D}{kT}} (e^{\frac{qV}{kT}} - 1) \tag{7}$$

where n_1 is the electron density in material 1 (InGaAsP), A_i's are constants which account for the degeneracy [13], and N_{C1} and N_{C2} are the conduction band effective density of states.

In most cases, it can be verified that $v_{d2} >> v_{r2}$ and the conduction mechanism is thermoionic emission dominated. Also, though equation 4 indicates a rectifying characteristic, the large J_{ps} value (exceeds 1000 A/cm^2 in most cases) renders the junction more "ohmic" than rectifying in nature.

Solving the steady state carrier transport and continuity equations for electrons,

$$-\frac{N_2}{\tau_{n2}} = \mu_N \overline{E} \frac{\partial N_2}{\partial x} + D_n \frac{\partial^2 N_2}{\partial x^2}$$

$$J_e = q\mu_N N_2 \overline{E} + qD_N \nabla N_2$$

the electron leakage current is given by

$$J_e(x) = (\frac{\mu_N}{\mu_p})\frac{J_P}{N_{A2}}N_2(x_2) - \frac{qD_N}{A}N_2(x_2)[\frac{1}{y_1}e^{\frac{L}{y_2}-\frac{x}{y_1}} + \frac{1}{y_2}e^{-\frac{L}{y_1}+\frac{x}{y_2}}] \quad (8)$$

where

$$A = e^{\frac{x_2}{y_2}-\frac{1}{y_1}} - e^{-\frac{x_2}{y_1}+\frac{L}{y_2}}$$

$$y_{1,2} = \frac{\pm L_{ed} + \sqrt{L_{ed}^2 + 4L_e^2}}{2} \quad (9)$$

$$L_{ed} = (\frac{\mu_N}{\mu_P})\frac{J_P\tau_{N2}}{qN_{A2}}$$

and

$$L_e^2 = D_N\tau_{N2}$$

with τ_{N2} the electron lifetime in the InP cladding layer. In arriving at the above solution, we have assumed the boundary condition $N_2(L)=0$. However, when the leakage is drift dominated, the boundary condition $N_2(L)$ is not important as is apparent from (8).

The total injected current density J_{tot} is simply

$$J_{tot} = J_p + J_e = J_{rec} + J_{leak} \quad (10)$$

Since J_e is just the leakage current J_{leak}, it follows that the recombination current $J_{rec}=J_p$. Up to lasing threshold, J_p can be expressed as

$$\frac{J_{rec}}{qd} = Bn_1(n_1 + N_{A1}) + C_{chcc}n_1^{2.09}(n_1 + N_{A1}) + C_{chsh}n_1(n_1 + N_{A1})^{2.14} \quad (11)$$

where d is the active layer thickness, B is the radiative recombination constant, C_{chcc} and C_{chsh} are the Auger coefficients for the CHCC and CHSH processes [16]. B is estimated from spontaneous lifetime data and C_{chcc} abd C_{chsh} are calculated as described in [16] (see figure 4.10).

The discontinuities in the conduction (ΔE_c) and valence band (ΔE_v) play an

important role (see equations 7,8) in determining the magnitude of the leakage current. Unfortunately, the discontinuity in the quaternary system is not known accurately. However, there are experimental [17,18] indications that a substantial fraction of the discontinuity lies in the valence band. We have used $\Delta E_c = E_g/3$ as measured in references 17 and 18. If the interface is graded, then the potential spike which is resistive to hole injection would decrease, resulting in less leakage. In this work, an abrupt interface is assumed. However, the ratio $\frac{\Delta E_c}{\Delta E_v}$ as well as the doping level N_{A2} are varied to provide a quantitative trend and estimate of the leakage current and its effects.

4.3b Hot carrier induced leakage

For quaternary lasers and LEDs, the injected electrons in the active region have been found [19] to have a temperature different from the surrounding lattice. Thus, we have to include this effect in the leakage calculation. The results of T_e at 300 °K from reference 19 have been used and the electron temperatures at various lattice temperatures (T_L) are estimated from the expression :

$$T_e(T_L) = T_e(300)\frac{C_{chcc}(T_L)}{C_{chcc}(300)} \qquad (12)$$

where it is implicitly assumed that the hot carriers are generated by the Auger process. With $\Delta E_c = E_g/3$, and with $N_{A1} = 4.6\times 10^{17} cm^{-3}$, $N_{A2} = 1.4\times 10^{17} cm^{-3}$, the calculated leakage has the same order of magnitude as the observed results in section 4.2. Figure 4.11 shows the calculated effect of doping and discontinuity on the magnitude of leakage current in a 1.2 μm laser with d=0.2 μm and L=1.5 μm. It is observed from these results that in order to minimize leakage, the cladding layer could be doped heavily or a graded junction be grown to smear the spike at the interface. There is a slight discontinuity in slope of J_{th}. How-

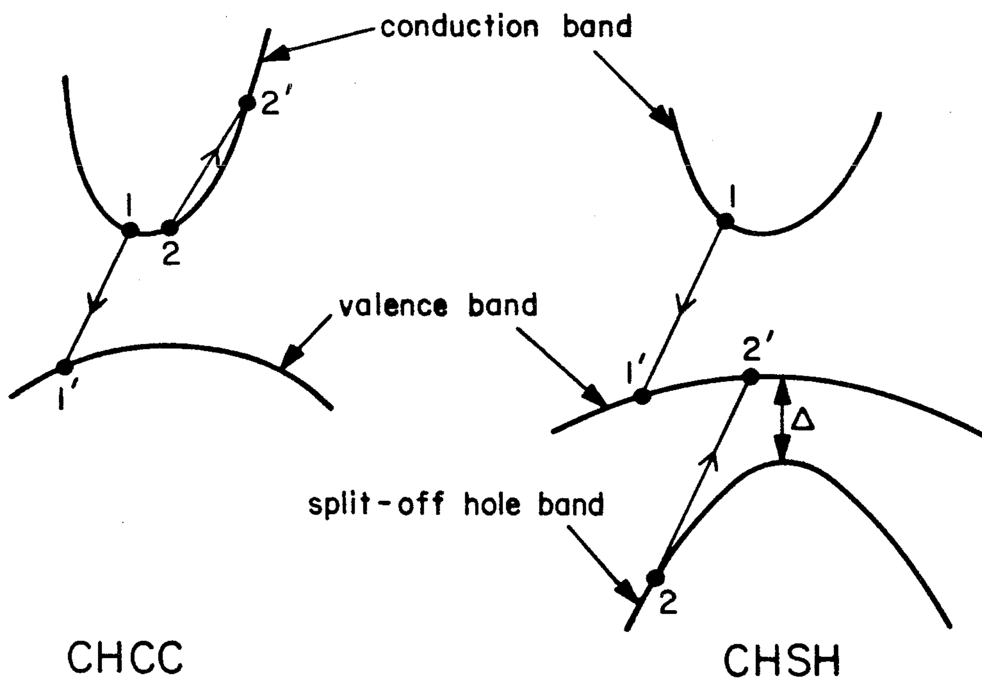

Fig. 4.10 Schematics of the conventional CHCC and CHSH Auger processes.

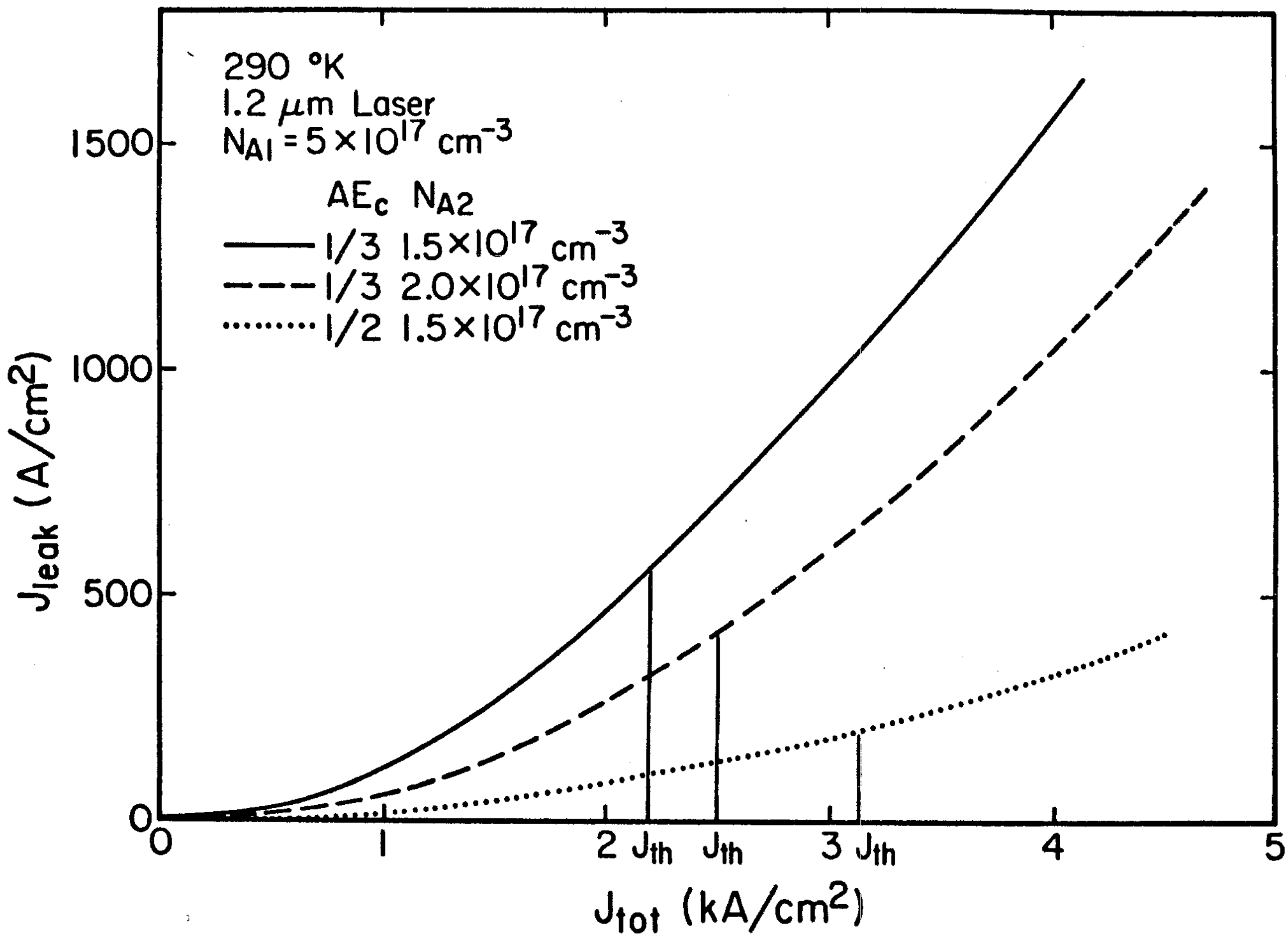

Fig. 4.11 Calculated electron leakage current versus total injected current for different P-InP doping levels and different conduction band discontinuities.

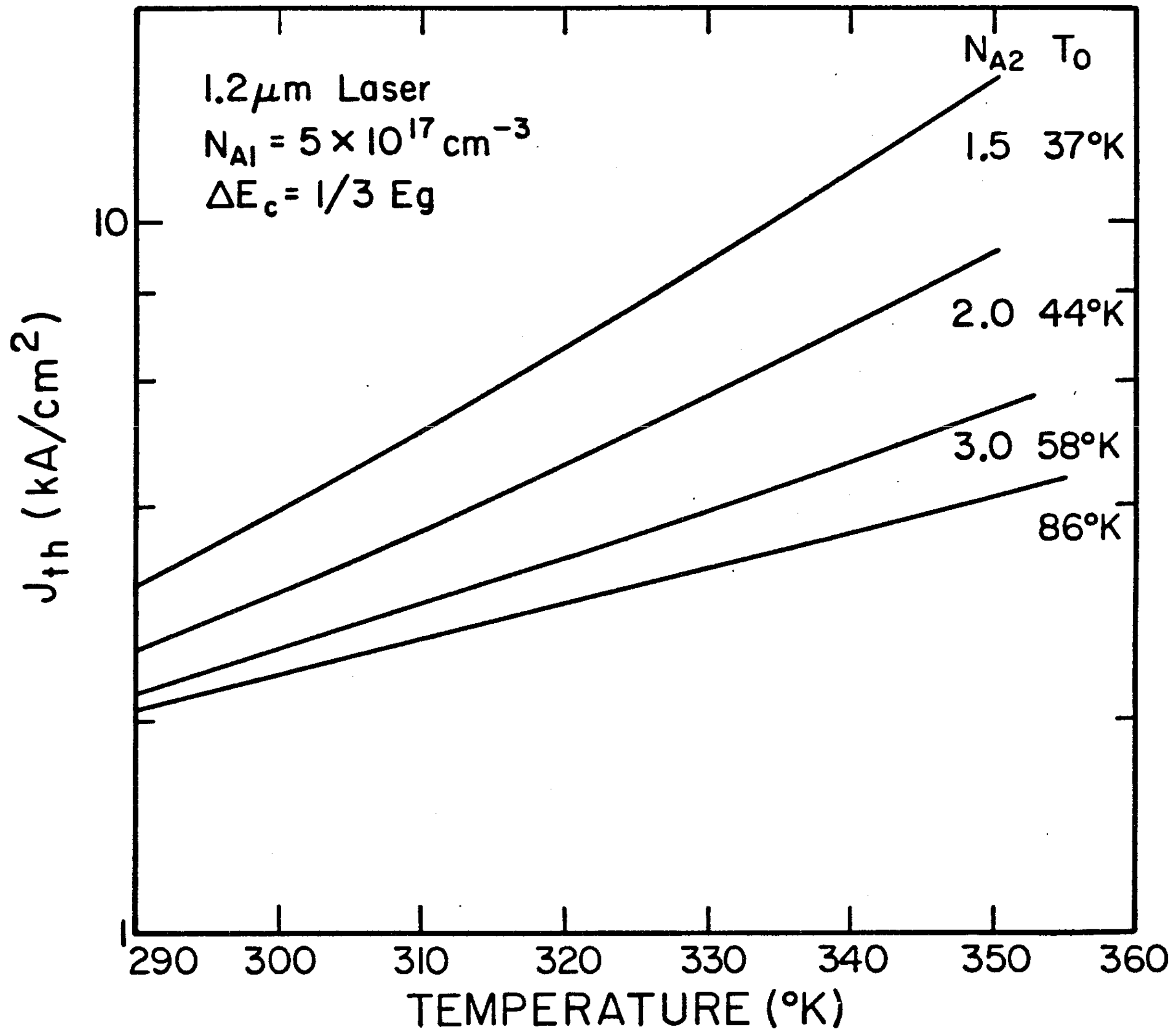

Fig. 4.12 Calculated T_0 for different P-InP doping levels.

ever, for large leakage currents, this change in slope is small and insignificant. Figure 4.12 depicts the effect of leakage current on the T_o of the laser. In the next section we describe experimental results which confirm these predictions.

4.4 P-doping effect on leakage— Experimental studies

Experimental investigations of the effects of p-layer doping level on the T_o of InGaAsP lasers emitting at 1.2 and 1.3 μm were performed under various conditions [20] and the results are summarized in Table 4.1. The schematic cross section of the Terrace Laser for these experiments is shown in figure 4.13.

4.4a Experiment I

In this experiment, two separate LPE growths of the laser structure shown in figure 4.13 were performed where the atomic fractions of zinc in the p layer growth melt were $\sim 10^{-5}$ (low doping) and $\sim 10^{-4}$ (high doping) respectively. For lasers grown with low zinc concentration, the T_o was found to be 43 $\pm$ 5 °K, with average threshold current density around 5.2 kA/cm^2 and with the external quantum efficiency about 50-60 % for both facets. The lasers grown with higher zinc concentration, on the other hand, had values of $T_o \sim 85 \pm 5$ °K(with highest being 90 ^{0}K) but with higher threshold current densities averaging around 8.4 kA/cm^2.

It is noted from the above results that, by increasing the doping level in the growth melt, T_o can be increased significantly. In doing so, however, we paid the penalty in higher threshold current density and lower quantum efficiency ($\sim$ 30% for both facets). This increase in threshold current density is attributed to the Zn outdiffusion from the cladding into the active layer during the growth of the P layer [21].

Wavelength (μm)	Condition	T_o (°K)	J_{th} (kA/cm^2)
1.2	Wafer heated at 675 °C	41 ± 7	∿ 5
1.2	Wafer not heated	60 ± 7	∿ 5
1.3	Low doping level	43 ± 5	5.2
1.3	High doping level	85 ± 5	8.4
1.3	Modified structure	83 ± 4	4.0

Table 4.1 **Summary of the experimental observation of T_o and threshold current density under various conditions.**

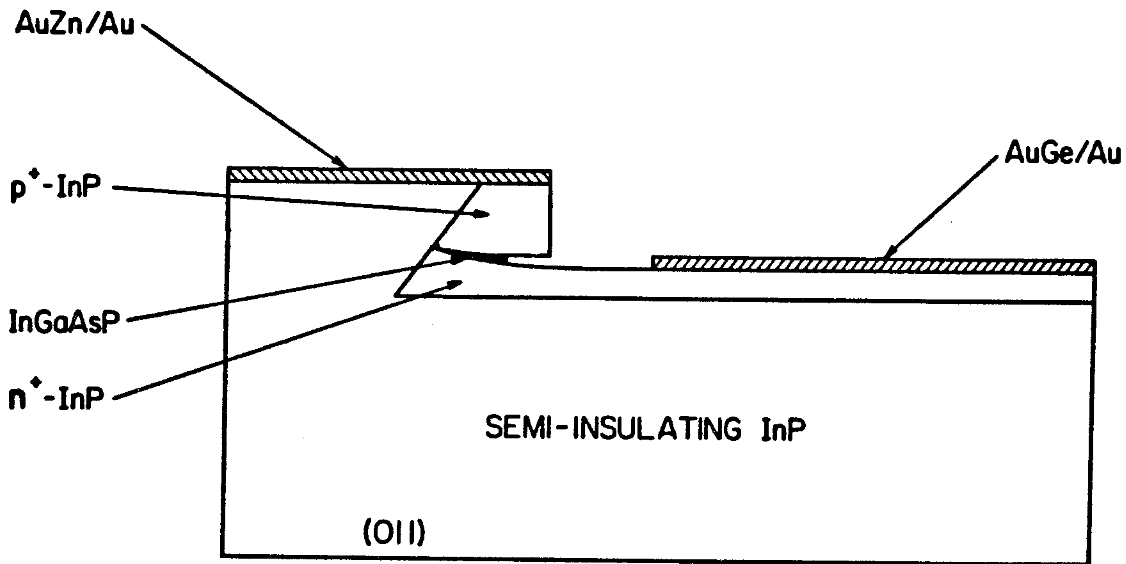

Fig. 4.13 A schematic diagram of a Terrace Laser.

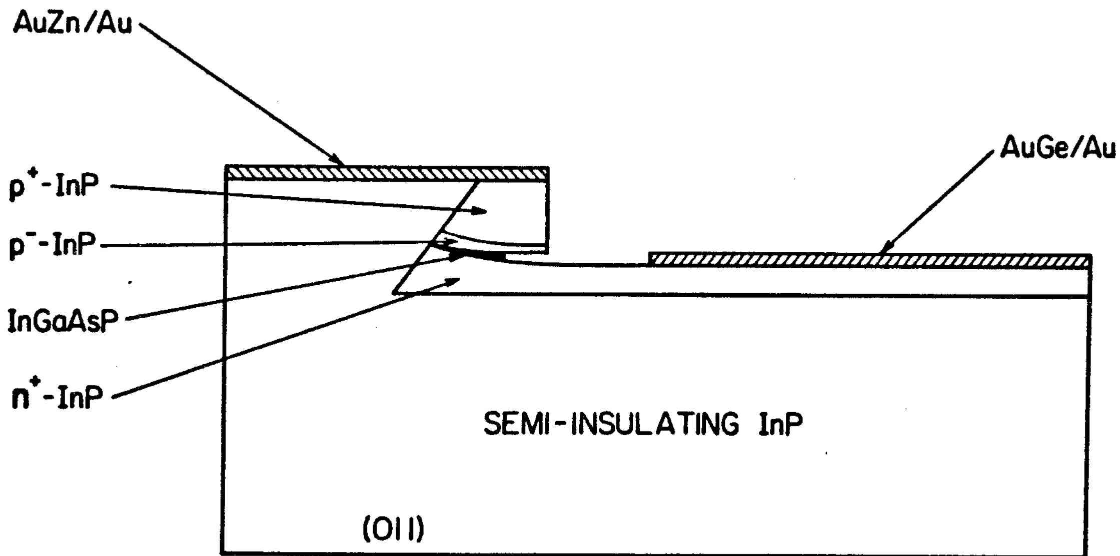

Fig. 4.14 A schematic diagram of a Terrace Laser with an extra p^--InP layer.

4.4b Experiment II

In the second experiment, a grown wafer with moderate p-doping in the cladding layer was cleaved into two pieces, one of which was put into the LPE system and heated to 675 °C in $P-H_2$ atmosphere for about an hour. The T_o of the lasers from the unheated wafer was 60 ± 7 °K, whereas that of the heated one was 41 ± 7 °K. Again, the decrease in T_o in the heated wafer is attributed to the Zn outdiffusion from the cladding into the active layer during the heating.

4.4c Application to high T sub o lasers

Having identified the cause of the abnormally low T_o, we proceeded to modify the laser structure to impede Zn diffusion into the active region. The schematic of a four layer structure is shown in figure 4.14. A thin (0.3-0.5 μm) p^--InP layer was first grown adjacent to the active layer, following by a p^+-InP layer. This thin layer acts as a buffer to absorb the Zn diffused from the p^+ layer to provide the desirable highly doped cladding layer, and at the same time acts as a diffusion stop layer to reduce the Zn diffusion into the active layer.

The resulting lasers have a T_o of 83 °K with threshold current densities around 4 kA/cm^2. The lowest I_{th} was 11 mA for a cavity volume of $250\times 0.2\times 1.5$ μm^3. The external quantum efficiency is around 70% for both facets at $I=3I_{th}$. This extra layer has served to improve the temperature sensitivity of the threshold current density without raising its room temperature value.

4.5 Conclusion

In conclusion, the electron and hole leakage in a InGaAsP laser emitting at 1.2 and 1.3 μm have been measured directly in the temperature range of 10-32 °C, using a laser-bipolar-transistor structure. No hole leakage has been observed.

On the other hand, electron leakage is found to be substantial. The leakage current is found to be a sensitive function of temperature. Experimental data obtained show that lasers with the leakage current eliminated have the highest T_0 's. Theoretical study of carrier injection across the heterojunction including the electric field and hot carrier effects at high level injection also predicts these results. Furthermore, the study suggests adding a p^--InP layer in the conventional 3 layer DH structure to optimize the threshold current and light output characteristics. This is verified experimentally.

Appendix 4-1 Hole injection across a heterobarrier

For simplicity, we consider a metal-semiconductor (p-type) Schottky barrier as shown in figure 4.15. The applied voltage V between the metal and the semiconductor bulk gives rise to a flow of holes into the metal. Throughtout the region between x_m and W (see figure 4.15), the hole current is expressed as :

$$J_P = -q\mu_P p(x)\frac{d\varphi_P(x)}{dx} \tag{A-1}$$

where μ_p is the hole mobility, $\varphi_p(x)$ is the quasi-fermi level for holes at x, and P(x) is the hole density :

$$P(x) = N_A e^{\frac{q}{kT}(\varphi_P(x) - \psi(x))} \tag{A-2}$$

with $\psi(x)$ denoting the potential of the valence band. Thermionic emission for holes occurs in the region between x=0 and $x=x_m$ and the hole current there is expressed in terms of the thermal velocity v_r (equation 6b):

$$J_P = q(P(x_m) - P_o)v_r \tag{A-3}$$

where $P(x_m)$ is the hole density at x_m when the current is flowing and P_o is the hole density at x_m without current flow (the Fermi-level of the metal is taken as the zero reference) :

$$P_o = N_A e^{-\frac{q\psi_{BP}}{kT}} \tag{A-4}$$

Substituting equation A-2 into equation A-1 and then intergrating the resulting expression from x_m to W, we get :

$$e^{\frac{q\varphi(x_m)}{kT}} - e^{\frac{qV}{kT}} = -\frac{J_P}{\mu_P N_A kT}\int_{x_m}^{W} e^{\frac{q\psi(x)}{kT}}dx \tag{A-5}$$

Next solve equations A-3,A-4 for $e^{\frac{q\varphi(x)}{kT}}$ and substitute it into equation A-5 :

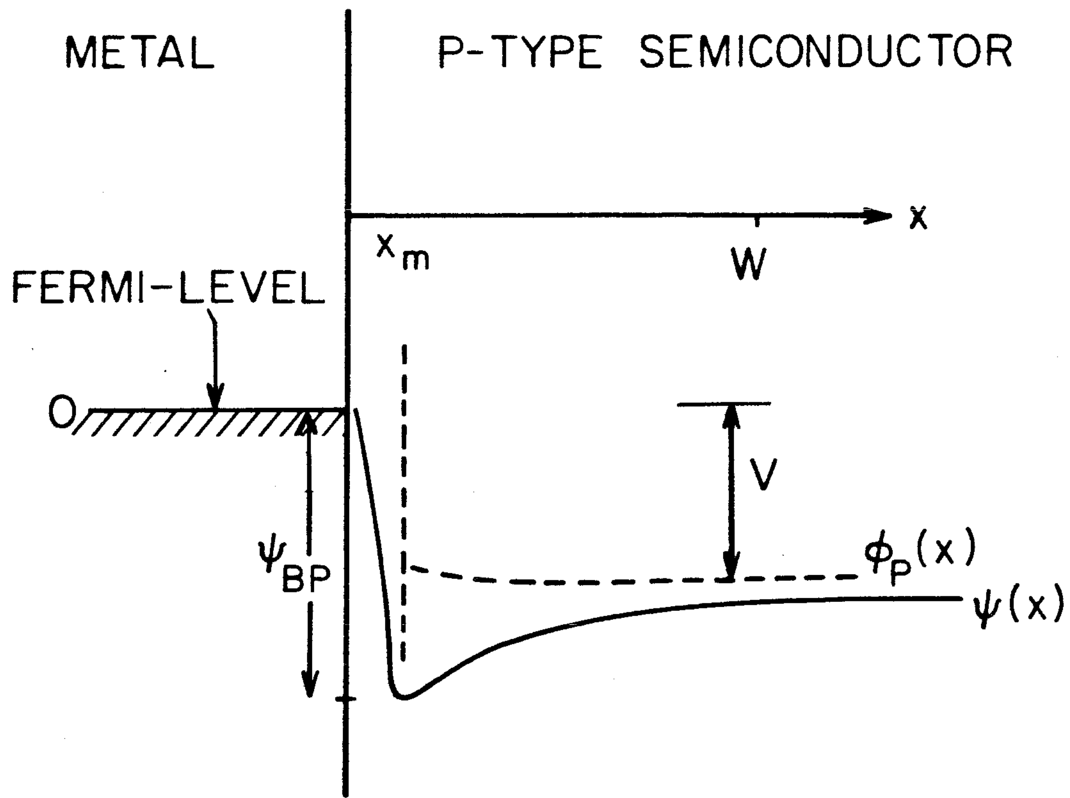

Fig. 4.15 A band diagram representation of a Schottky Barrier.

$$J_P = qN_A \frac{v_r}{1 + \frac{v_r}{v_d}} (e^{\frac{qV}{kT}} - 1) \tag{A-6}$$

where

$$v_d^{-1} = \frac{q}{\mu_P kT} \int_{x_m}^{W} e^{-\frac{q}{kT}(\psi_{BP} + \psi(x))} dx \tag{A-7}$$

and $\psi_{BP}=\psi(x_m)$ is the barrier height. We consider the case where the charge density between the metal surface ($x \approx 0$) and $x=W$ is essentially that of the ionized acceptor N_A, thus the valence band is parabolic near the interface and in the limit $x_m \to 0$:

$$\psi(x) = \frac{qN_A}{2\varepsilon}(x-W)^2 \tag{A-8}$$

With this $\psi(x)$ into equation A-7, we have

$$v_d^{-1} = \frac{1}{\mu_P kT} (\frac{\varepsilon \pi kT}{2N_A})^{\frac{1}{2}} \mathrm{erf}(\sqrt{\frac{qV_{BP}}{kT}}) e^{-\frac{q\psi_{BP}}{kT}} \tag{A-9}$$

For p-InP--InGaAsP heterojunction, the active region (InGaAsP) takes the place of the metal and if we identify V_{BP} as κV_D and $V=V_1 + V_2$ and so on, equations A-6, and A-9 become equations 5 and 6 respectively.

References

1. G. Henshall and G. H. B. Thompson, presented at the Eighth IEEE International Semiconductor Laser Conference, Sept. 1982, Ottawa, Canada.

2. S. Yamakoshi, T. Sanada, O. Wada, I. Umebu, and T. Sakurai, Appl. Phys. Lett., vol 40, p. 144 (1982)

3. S. Yamakoshi, T. Sanada, O. Wada, I. Umebu, and T. Sakurai, in Gallium Arsenside and related compounds, 1981 Oslo, Inst. of Phys. Conf. Ser., International Symposium on GaAs and Related Compounds.

4. O. Wada, S. Yamakoshi, and T. Sakurai, Appl. Phys. Lett., vol 41, p.981 (1982)

5. M. Yano, Y. Nishitani, K. Hori, and M. Takusagawa, presented at the Eighth IEEE International Semiconductor Laser Conference, Sept. 1982, Ottawa, Canada.

6. A. Mozer, K. M. Romanek, W. Schmid and M. H. Pilkuhn; E. Schlosswe, Appl. Phys. Lett., vol 41, p964 (1982).

7. T. R. Chen, S. Margalit, U. Koren, K. L. Yu, L. C. Chiu, A. Hasson and A. Yariv, Appl. Phys. Lett., vol 43 (1983).

8. T. R. Chen, K. L. Yu, U. Koren, A. Hasson, S. Margalit and A. Yariv, J. Appl. Phys., vol 53, L-2533 (1982)

9. T. R. Chen, L. C. Chiu, K. L. Yu, U. Koren, A. Hasson, S. Margalit, and A. Yariv. IEEE, J. Quant. Electron., May, 1983.

10. T. R. Chen, B. Chang, L. C. Chiu, K. L. Yu, S. Margalit and A. Yariv, to be published in Appl. Phys. Lett.

11. C. M. Wu and E. S. Yang, J. Appl. Phys., vol 49, p.3114 (1978).

12. L. C. Chiu, K. L. Yu, S. Margalit, T. R. Chen, U. Koren, A. Hasson and A. Yariv,

to be published in IEEE, J. Quant. Electron.

13. H. C. Cassey, Jr. and M. B. Panish, "Heterostructure Lasers," Part A, Chapter 4, Acadamic Press, New York (1978)

14. S. M. Sze, "Physics of Semiconductor Laser Devices," Chapter 5, J. Wiley and Sons (1981).

15. D. L. Scharfetter, Sol. Stat. Electron., vol 8, pp.299-311 (1965)

16. L. C. Chiu, P. C. Chen, and A. Yariv, IEEE J. Quant. Elect., QE-18, pp. 938-941 (1982)

17. S. R. Forest, O. K. Kim, and R. G. Smith, Appl. Phys. Lett., vol 41, pp. 95-98 (1982)

18. G. E. Stillman, L. W. Cook, G. E. Bulman, N. Tabatabaier, R. Chin, and P. D. Dapkus, IEEE Trans. Elect. Dev., ED-29, pp. 1355-1371 (1982)

19. J. Shah, R. F. Leheny, R. E. Nahory, and H. Temkin, Appl. Phys. Lett., vol 39, pp.618-620 (1981).

20. T. R. Chen, L. C. Chiu, K. L. Yu, U. Koren, A. Hasson, S. Margalit, and A. Yariv. to be published in Appl. Phys. Lett.

21. W. Ng and Y. Z. Liu, Electron. Letts., vol 16, pp. 693-695 (1980)

Chapter 5

Optoelectronic Integration in InGaAsP/InP system

5.1 Introduction

Integrated optoelectronics (IOE) involves the integration of optical and electronic devices of compatible performance on the same chip. Research [1-5] in the last decade has demonstrated the feasibilty and potential of IOEs based on GaAs/GaAlAs material system. Since InGaAsP/InP devices enjoy similar characteristics as their GaAs/GaAlAs counterparts, IOE is a natural step in the technological evolution [6]. Apart from its spectral range which makes it the preferred material system for high frequency long distance communication, InP and its quaternary compounds have, compared to GaAs, higher peak electron velocity and thus greater potential for higher speed operation. Moreover, InP metal-insulator-semiconductor field-effect transistors (MISFETs) can be designed for both enhancement and depletion mode operation, a feature not available in GaAs field effect devices.

An important step in achieving IOECs is the fabrication of devices on non-conductive substrates to achieve optimal electrical isolation between devices. A further consideration is the power dissipation in micro circuits which can lead to a rise in operating temperature and exponentially change device performance. Therefore, the power dissipated by both lasers and other devices should be kept to a minimum (e.g. by low threshold lasers). This is especially important for IOECs where devices are made on substrates with poor heat conductivity. The low threshold lasers on semi-insulating Fe-doped InP such as the Groove Laser in chapters 2 and 3 are therefore ideal for such purposes.

5.2 Integration of a Groove Laser with InP MISFET

InP FETs formed with a Schottky diode gate (MESFETs) are not practical as the metal-InP junction is usually leaky and unstable. An alternative to the MESFET is the MISFET with either a native oxide or a dielectric, such as SiO_2 or Si_3N_4 deposited on InP as the gate insulator. The MISFET can be operated in the depletion mode to modulate the drain to source current (I_{DS}). As electron mobility is higher than hole mobility in InP, n-channel FETs are preferred. Also, for high speed operation, the gate capacitance must be minimized. This can be achieved with gate contact pads directly bonded on semi-insulating substrates.

The n-channel InP FETs are usually made with ion-implantation on semi-insulating InP substrates which are then annealed at high temperature (~ 700 °C) to thermally activate the implants. FETs with uniform channels can be made in this way. However, this process technique is undesirable in the Laser-FET integration because high temperature treatment causes excessive dopant diffusion from the p-InP layer into the nearby quaternary layer and degrades laser performance. We have consequently opted for the FET channel layer grown by LPE.

5.2a Fabrication

Both lasers and FETs are fabricated on semi-insulating InP with all the device layers grown in a single LPE step [7]. The Groove TJS Laser is chosen as its low CW threshold current enables direct light output modulation by the MISFET drain-source current without additional biasing.

The FET fabrication proceeds after the groove TJS laser fabrication (as described in section 3.3). After the Zn-diffusion step, Au/Zn and Au/Ge are evaporated on the p and n sides respectively. A layer of CVD SiO_2 is deposited over

the whole wafer and the gate windows are opened by photolithography. The Au/Ge layer under the gate windows, as well as the top two LPE layers underneath are completely etched away. The last (undoped) InP layer is etched with 10% iodic acid until a desirable thickness is reached. After etching, the wafer is cleaned with methanol and dilute nitric acid. A recess structure is thus formed. Gate insulating layer is obtained by treating the substrate in O_2 plasma for 15 minutes and by depositing ~600Å CVD SiO_2 on the gate recess. The gate electrode is made of an evaporated Cr/Au layer defined with a conventional lift-off technique. The recessed channel is about 6 μm wide while the Cr/Au gate electrode is 1.5-2 μm long. The wafer is thinned and cleaved into 300-400 μm (cavity length) chips. These chips are then bonded substrate side down to copper heat sinks. A schematic cross section of the resulting integrated device is shown in figure 5.1.

5.2b Characteristics

The performances of the laser and the electronic (MISFET) device are first examined separately. Figure 5.2 shows light versus current characteristics of a groove TJS laser at pulsed operation. This laser has a pulsed threshold current of 17 mA and a cavity length of 350 μm. Figure 5.3 shows the curve tracer characteristics of a InP MISFET. The FET has a transconductance of about 5-10 mmho. The drain-source current at zero gate voltage (I_{DS0}) is controlled by the channel thickness and can be typically 15-40 mA at 3 volts drain-source voltage. The I_{DS} current does not always saturate completely at zero gate voltage but frequently saturates or shows negative resistance at $V_g < 0$.

To demonstrate laser light modulation by the FET the test circuits shown in figure 5.4 is used. The laser is modulated by introducing 1.5 μsec pulses

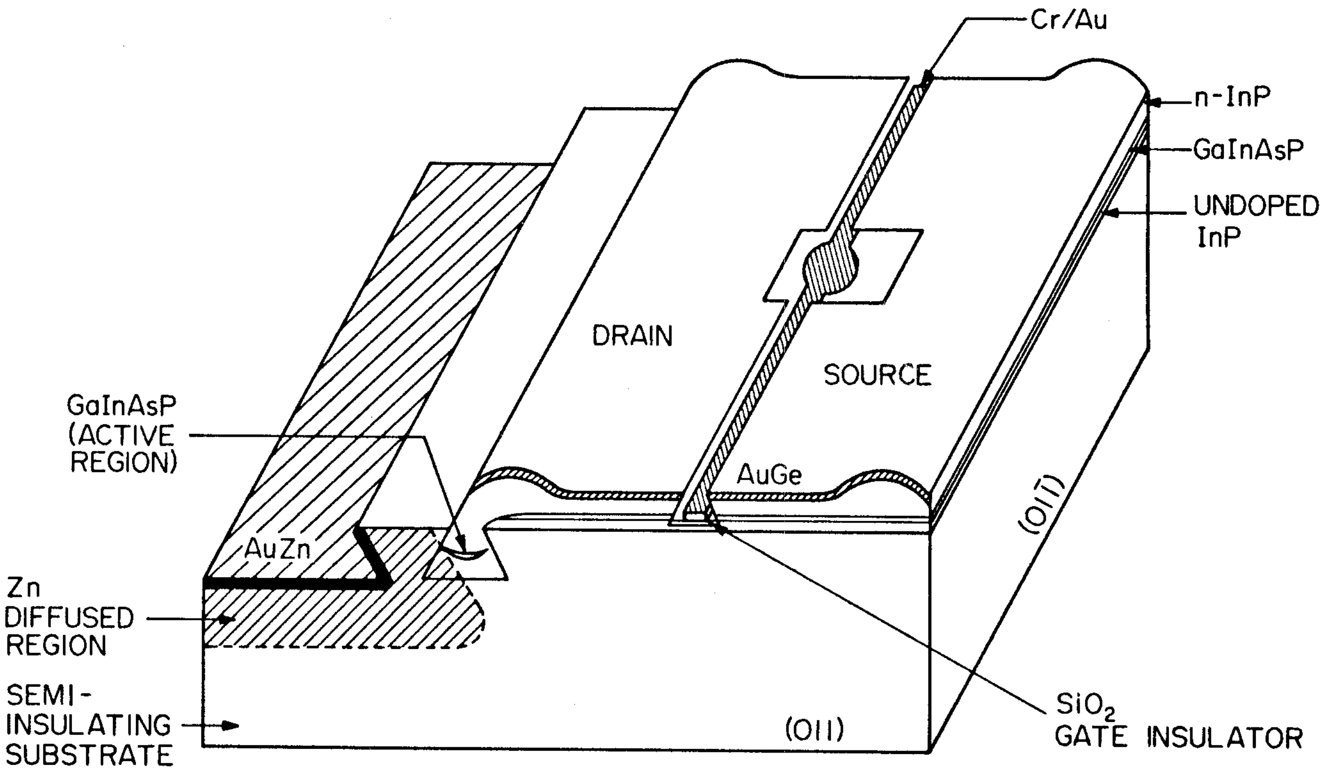

Fig. 5.1 A schematic diagram of a Laser-MISFET integrated device.

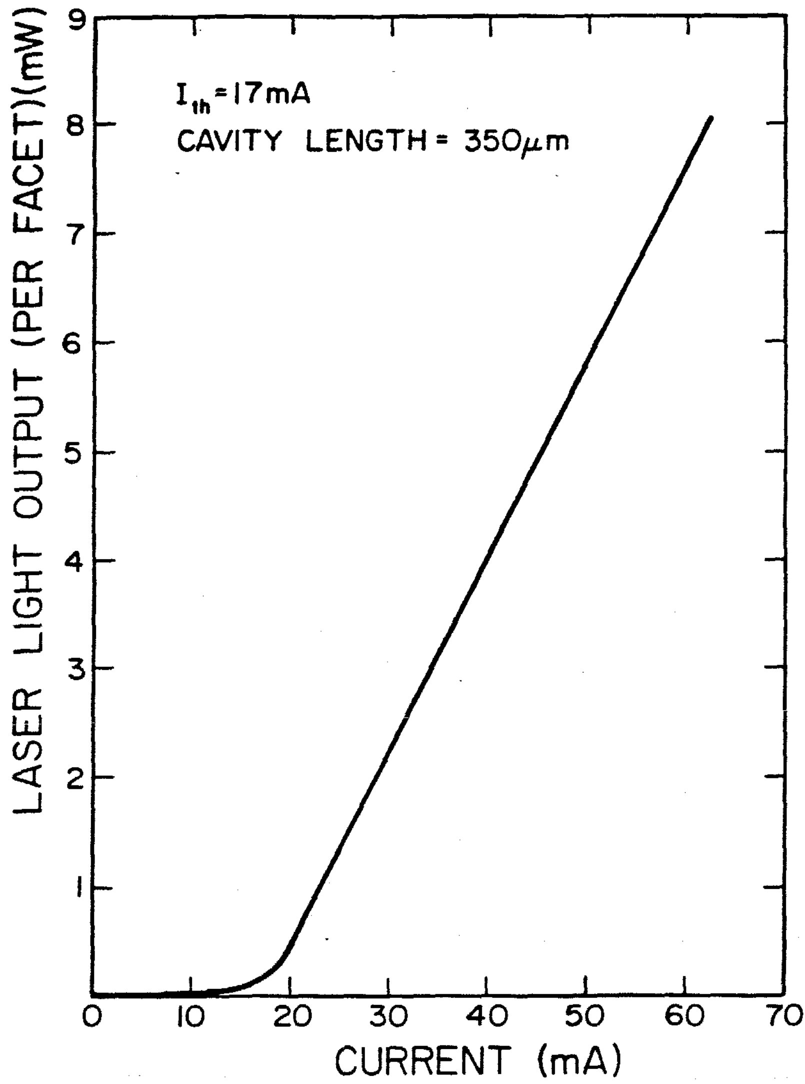

Fig. 5.2 L-I characteristics of the integrated laser.

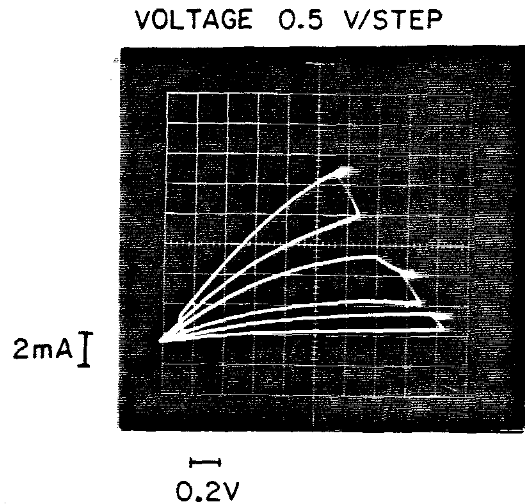

Fig. 5.3 I-V characteristics of the integrated depletion mode InP MISFET.

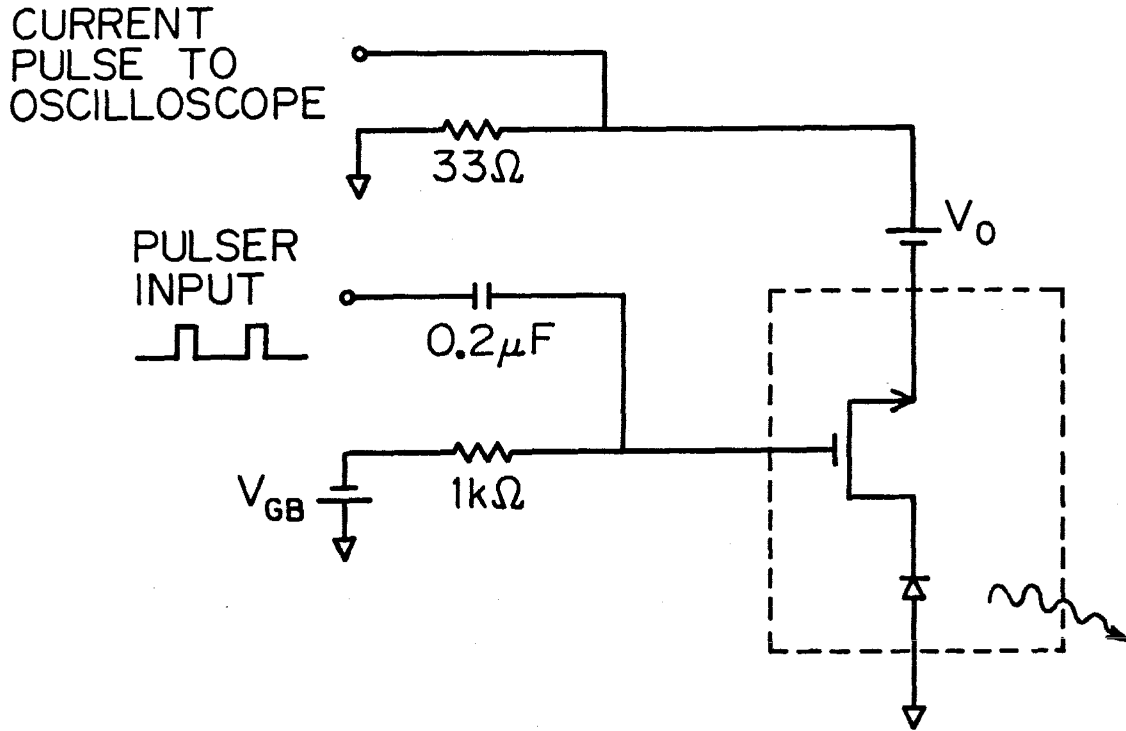

Fig. 5.4 A block diagram of the modulation circuit.

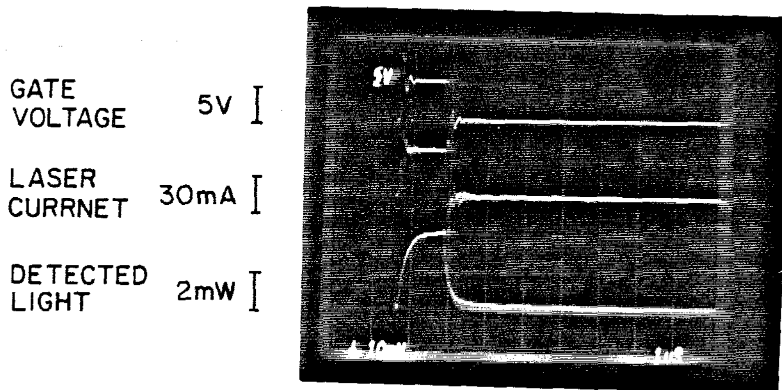

Fig. 5.5 A phototrace showing the laser output modulation with gate voltage.

through a high impedance to the FET gate terminal. The I_{DS} current response and the laser light output is shown in figure 5.5 with V_0 = -4 volts and V_{GB} = -5.5 volts. The laser light output is modulated-on-off by the FET. At pinch-off, that is, before and after the pulse, the current is less than 10 mA which is well below the laser threshold current. During the pulse the FET conducts and I_{DS} values of about 2 I_{TH} are obtained. The light pulse rise time shown in figure 5.5 is limited by the Ge photodiode response time (100 nsec) that is used here.

In effect, we have demonstrated for the first time Laser-FET integration in the InGaAsP/InP system. These IOECs can be used in high speed signal modulation.

5.3 Microcleaved mirrors for integration

The conventional method to fabricate a two-mirror semiconductor laser cavity is to cleave the substrate twice along parallel cleavage planes. This technique produces high quality vertical mirrors with irregularities in the mirror surface much smaller than a quarter of a wavelength of the laser light. However, for IOE applications, this cleaving technique would impose severe restriction on the geometry and dimension (limited by the cavity length) of the chip. Several methods have been devised to fabricate laser mirrors without having to cleave the entire substrate. The outstanding ones are etched mirrors [8], distributed Bragg reflectors [9] and microcleavage mirrors [10,11]. However, the first two methods have only resulted in lasers with higher threshold current density and lower quantum efficiency than the conventionally cleaved lasers.

The microcleavage technique achieves high quality mirrors. This was demonstrated first at Caltech in the fabrication of short cavity GaAs/GaAlAs lasers [10]. This technique (figures 5.6,5.7) relies critically on a selective etching underneath the double-heterostructure to form a cantilever structure. However,

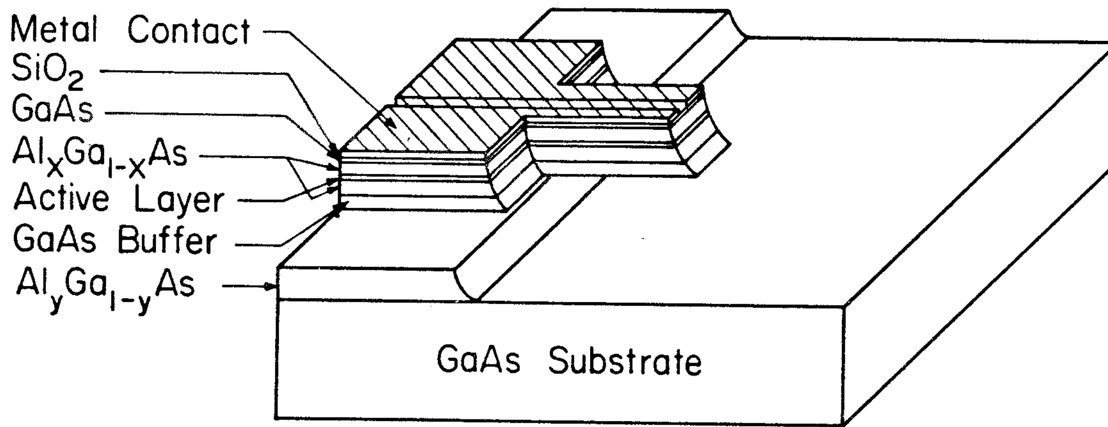

Fig. 5.6 A schematic diagram of a cantilever prior to microcleavage (Ref. 10).

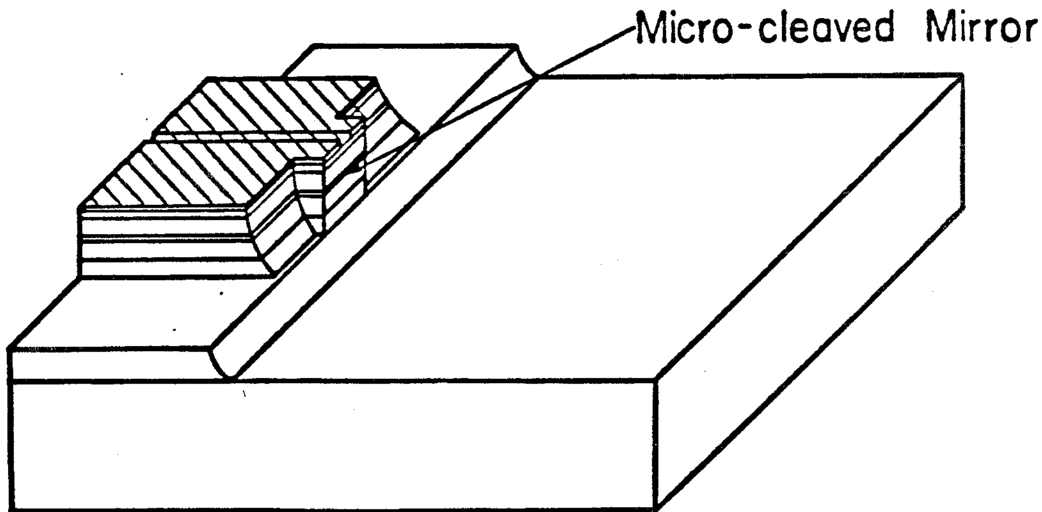

Fig. 5.7 A laser with a micro-cleaved mirror (Ref. 10).

such selective etching cannot be adopted in the quaternary system for lack of a suitable selective etchant (for differently composed (1.1-1.7 μm) quaternary layers). We have therefore devised a different approach [11] to achieve microcleavage in the InGaAsP/InP system.

5.3a Fabrication

Etching profiles with preferential etchants depend on stripe orientations (section 2.2). For stripe openings made in the [011] direction on a (100) substrate, the shape of the etched side wall is shown in figure 5.8. For stripe openings made in the orthogonal direction $[01\bar{1}]$, the etched side wall is shown in figure 5.9. Thus with the wafer masked as shown in figure 5.10, the etching proceeds from both sides of the masked central stripes resulting in a suspended bridge of triangular cross section. The etching along the edges of the masked stripes in $[01\bar{1}]$ direction defines stop-etch planes. Microcleavage of the bridges along these stop-etch planes is then accomplished with ultrasonic vibrations.

A schematic cross section of a Groove Laser is shown in figure 5.11. The etchings on the left hand side of the laser channel preceding Zn diffusion (shown on the left in figure 5.11) are continuous and uninterrupted through the longitudinal laser axis. The mirrors of this laser can be formed with either the usual cleaving or the microcleavage technique. For microcleavage, a preferential etching is then performed on the right hand side of the laser channel with Si_3N_4 as etching mask thus forming ~ 15 μm wide mesa miniature bridges. 10 % iodic acid is employed as the etchant. Since the etching is done in the original semi-insulating InP substrate and does not intersect any grown layers inside the groove, very sharp and well defined dovetail shaped etched walls are obtained on both sides of the Si_3N_4 stripes. The exposed squares defining the suspended

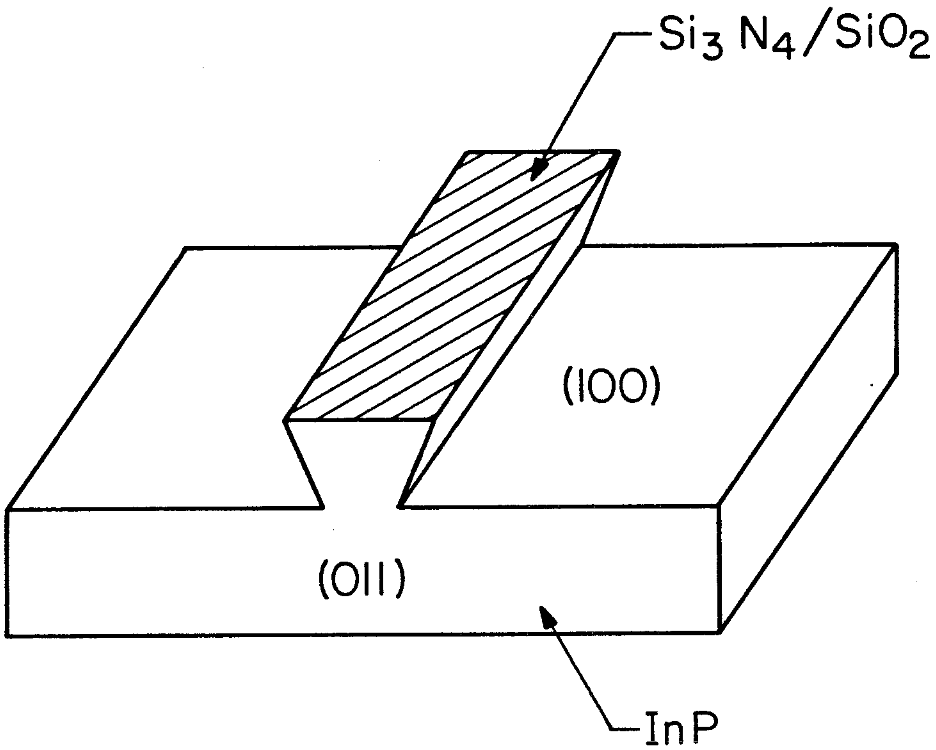

Fig. 5.8 A diagram showing the etching with a masked stripe made in the [011] direction.

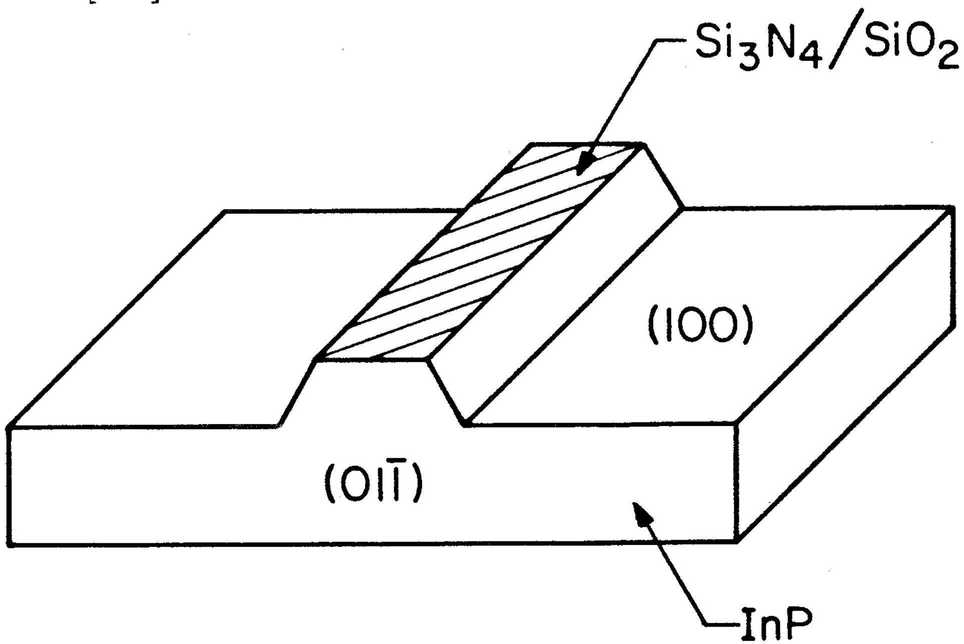

Fig. 5.9 A diagram showing the etching with a masked stripe made in the $[01\bar{1}]$ direction.

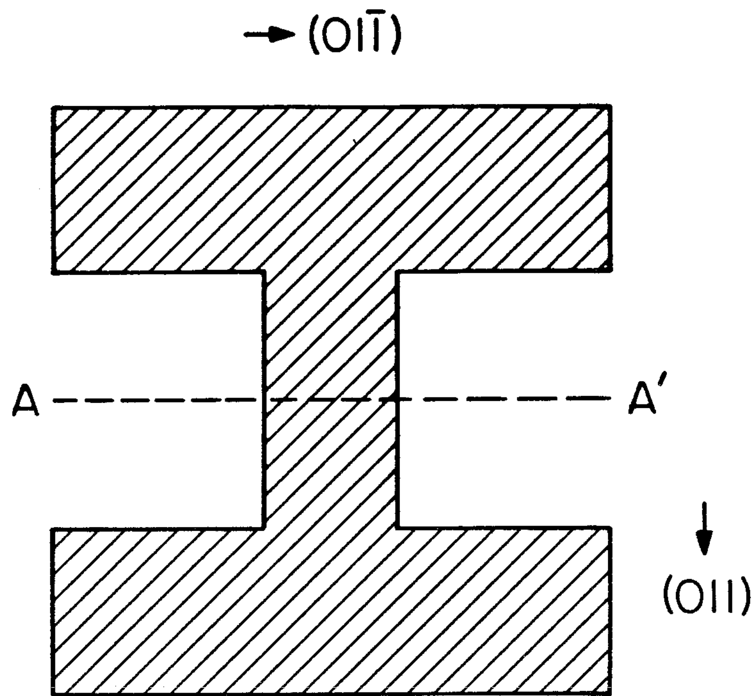

Fig. 5.10a The mask for the fabrication of suspended bridges.

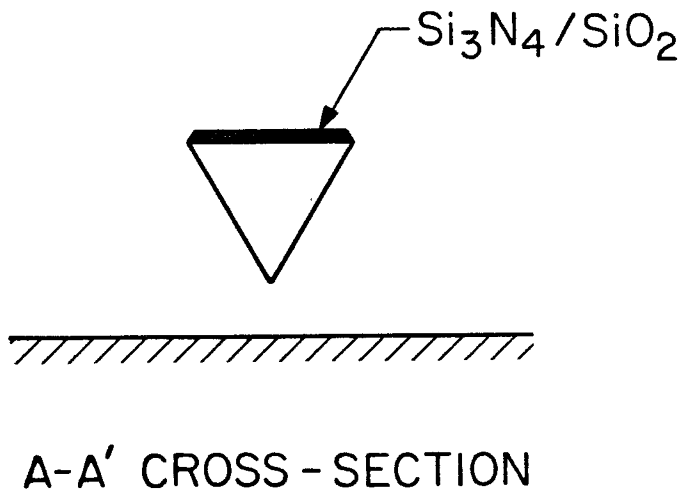

Fig. 5.10b The cross section of the suspended bridge for microcleavage.

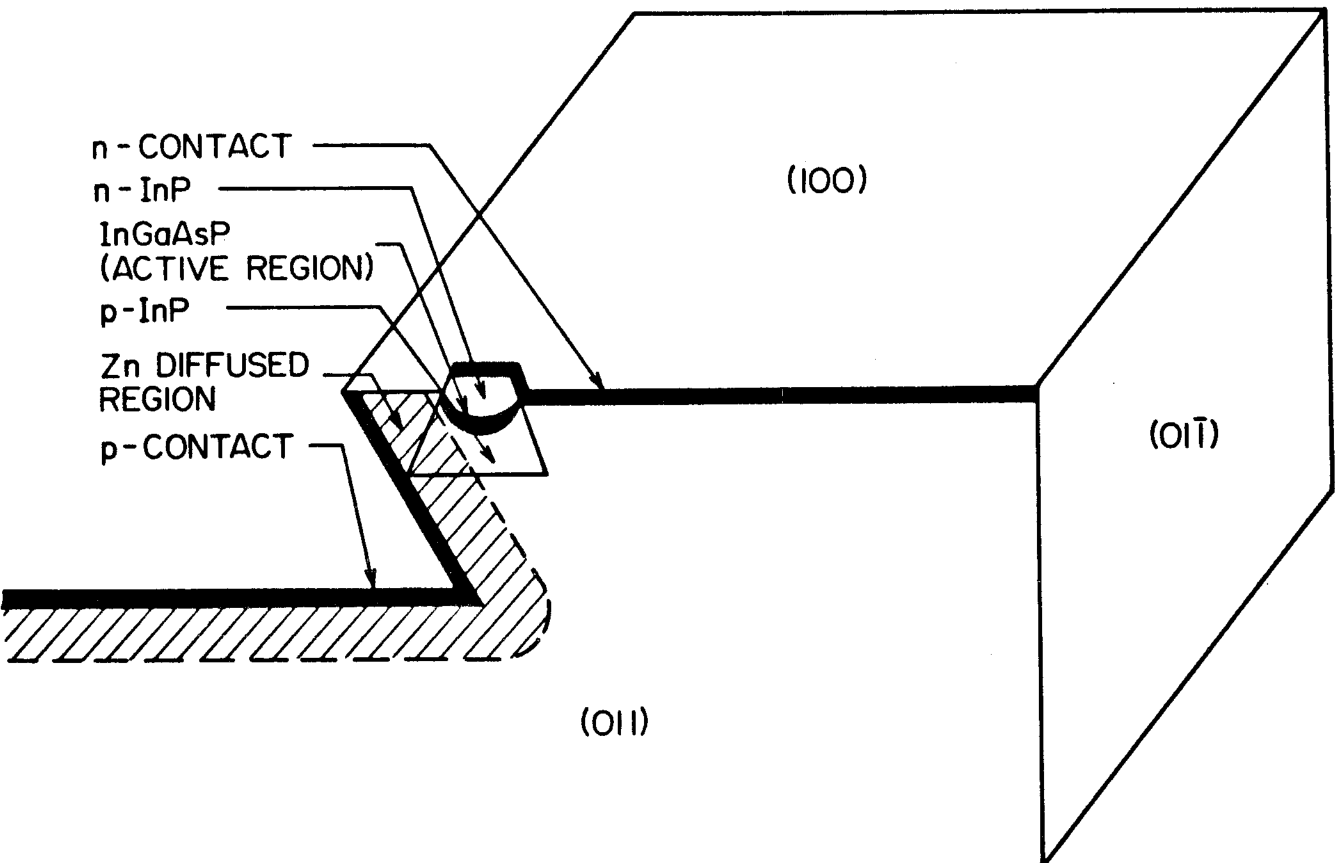

Fig. 5.11 A schematic diagram of a Groove Laser for microcleavage.

bridges are then microcleaved. The resulting structure after microcleavage is shown in figure 5.12. The resulting lasers possess differential quantum efficiencies of 35-45 % for both facets, similar to those lasers of the same type which are conventionally cleaved.

This method therefore allows the designers of IOECs the freedom to integrate arbitrary numbers of high quality lasers with electronic components, and paves the way to IOECs of high complexity.

5.4 Integrated phase-locked laser array

The phased array consists usually of a number of spatially separated coherent sources which are phase coupled by some means (e.g. external cavity [12], evanescent waves [13], overlapping modes [14], and coupling stripes [15]). These devices can produce laser beams with very narrow angular divergence as well as high output power. In addition, the laser beam can be directed by electrically varying the relative phase and amplitude between individual lasers. In optical communication, these phased array injection lasers are therefore desirable in coupling light sources to fibers. The InGaAsP/InP laser array is especially favorable since it can emit in the optimal fiber wavelength range. We described here the first integrated InGaAsP/InP phase locked laser array [16] where a diffraction coupling mechanism [17] is used to phase lock individual stripe lasers on the same chip.

A schematic representation of the integrated phased array is shown in figure 5.13. The structure consists of three sections. The ten modified stripe lasers with equal lateral spacing occupy the central section of the device. The two end sections allow the individual beams to diffract and "mix". The length of the central section L_2 is $\sim$ 100 μm, and the end sections L_1, L_3 are 50-100 μm long.

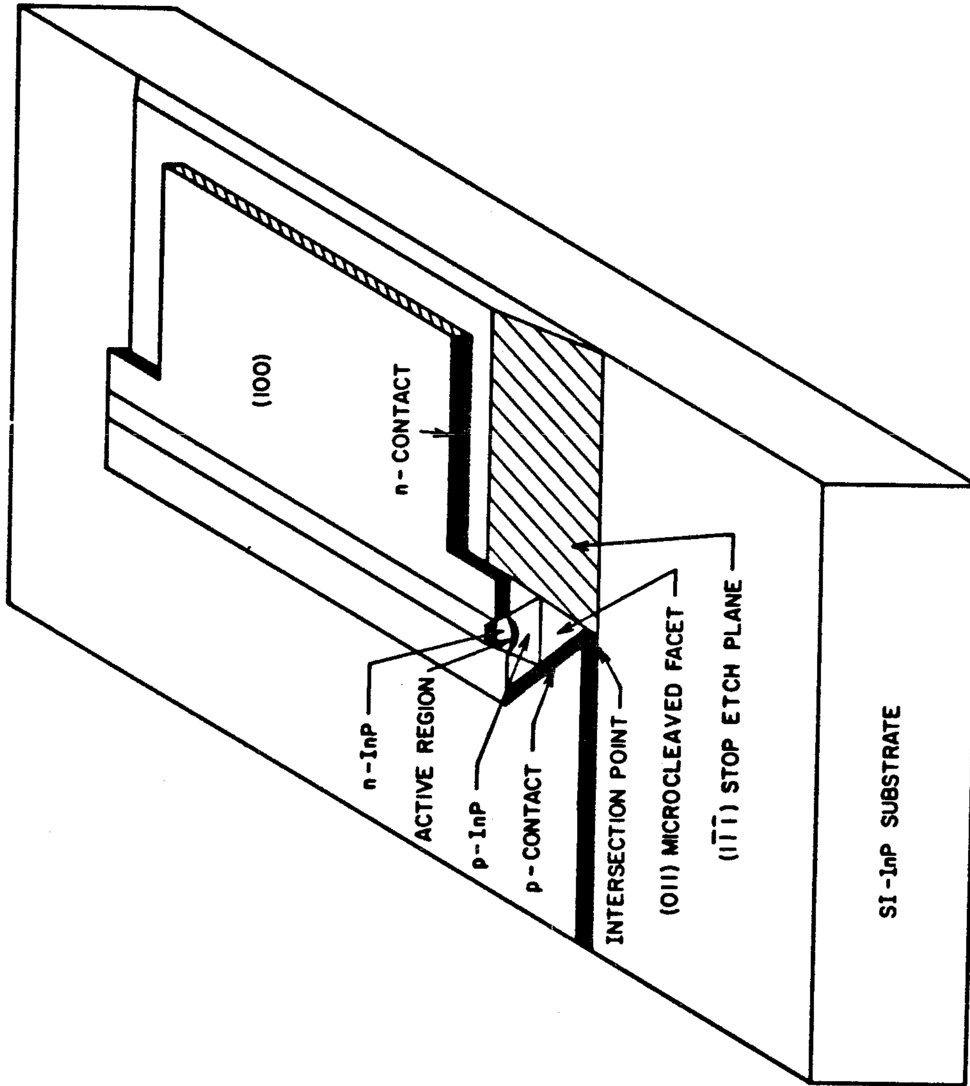

Fig. 5.12 A Groove Laser after microcleaving.

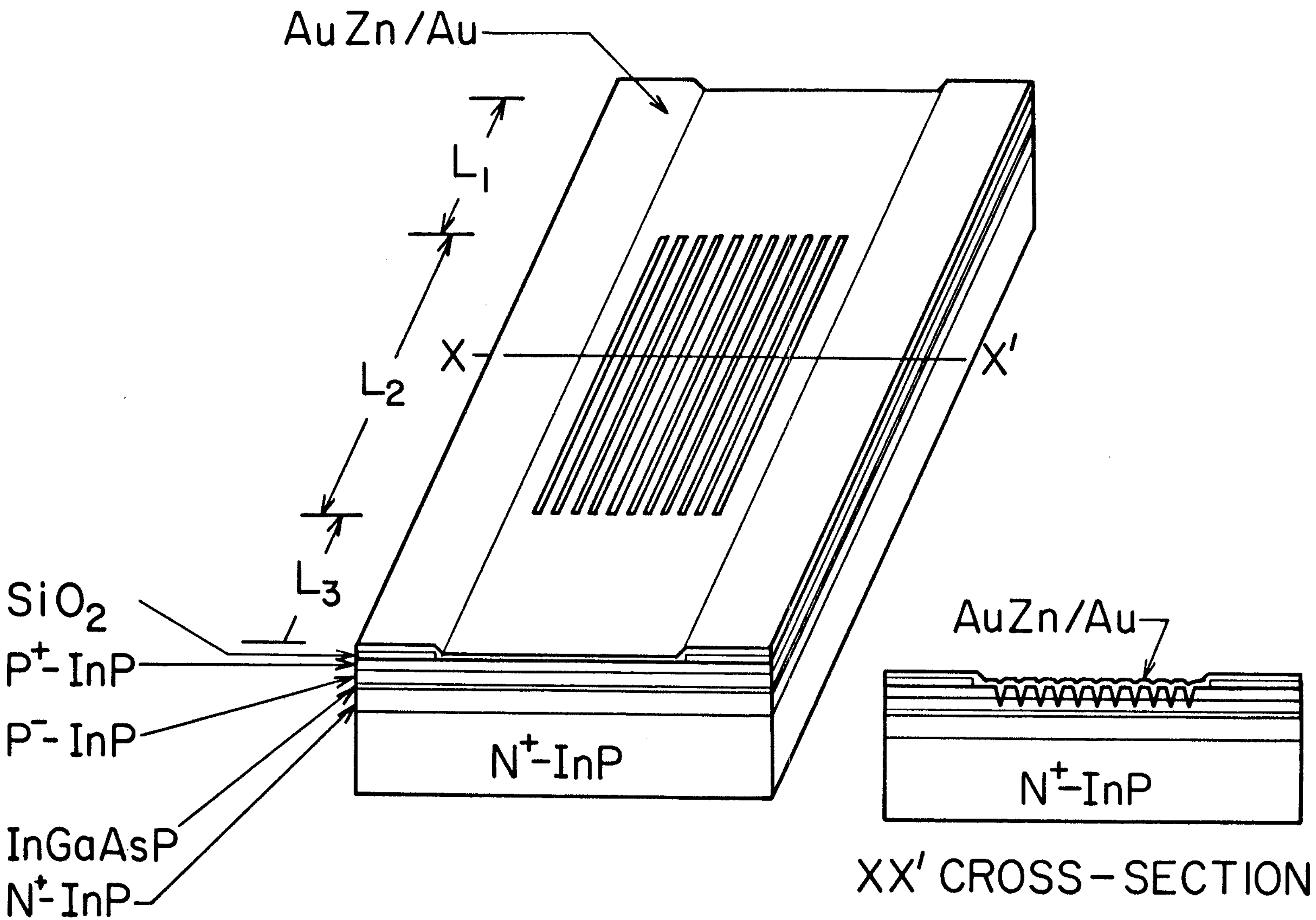

Fig. 5.13 A schematic diagram of a diffraction coupled laser array.

Each individual laser stripe is ~ 3 μm wide with 2 μm separation between adjacent stripes. A cross-section of the laser stripes is also shown on right side of figure 5.13.

5.4a Fabrication

The fabrication of the integrated phased array starts with the LPE growths of four layers on n^+-InP substrate with liquid phase epitaxy. The composition and thickness of these layers are: n^+–InP confining layer, 3 μm; undoped InGaAsP active layer, 0.2 μm; p^--InP layer ~ 2 μm; and p^+–InP 0.2 μm. After growth, Si_3N_4 is deposited on the wafer and 10 stripe openings are made in the $[01\bar{1}]$ direction. On the central section, the p^+–InP and p^-–InP layers are etched with iodic acid through the stripe openings producing V-shaped grooves which are ~ 0.7 μm deep. After etching, the nitride is removed, a layer of SiO_2 is deposited on which ~50μm wide stripes are opened over the sections containing the stripe lasers (figure 5.13). AuZn/Au and AuGe/Au contacts are then evaporated on the top and bottom sides of the wafer respectively.

5.4b Diffraction coupling in phased array

As the metal semiconductor contact resistance is higher for the p^-–InP than for the p^+–InP, most of the current is injected through the top stripes rather than through the V-grooves. This periodic injection profile in the central section gives rise to maximum gain in the active layer beneath the stripes. Upon leaving the central section, the beams from the individual stripes spread out diffractively and, upon reflection from the end mirrors, couple with each other in the central section. In Appendix 5-1 it is shown that the phase between a laser field and the field coupled to it from the adjacent lasers is

$$\Delta\Phi = \frac{\pi\zeta n_{eff}}{2}\frac{a^2}{\lambda L} \tag{1}$$

where a is the center to center spacing between two adjacent lasers, λ is the free space wavelength, L is the length of the diffraction section of the resonator, n_{eff} is the laser mode effective index and ζ is given by :

$$\zeta = 1 + \frac{1}{\left[1 + \frac{a^2}{8L^2}\right]\left[1 + \frac{z_o^2}{4L^2 + a^2}\right]} \tag{2}$$

where z_o is the confocal parameter of the resonator, whose values lie between 1 (for $z_o >> L_d$) and 2 (for $z_o << L$). If $\cos(\Delta\Phi) > 0$, then the lasers in the array operate in phase, and the resulting far field pattern will be single lobed. If $\cos(\Delta\Phi) < 0$, the adjacent lasers operate out of phase and the double-lobed far field pattern will result. Thus the far field pattern can be changed by changing L. It is noted from equation 1 that the coupling between laser stripes is affected by n_{eff}, thus the coupling can be tuned by changing the injection level.

Considering the emission wavelength of the present laser (1.2 μm) and the beam divergence in the 50-100 μm diffraction section, a substantial overall coupling between the 10 individual lasers is expected. In most other arrays with wide separation between individual lasers, the coupling takes place only between adjacent stripes. For the present array having 3 μm wide stripes with 2 μm separation, the modal overlap between the adjacent laser stripes in the central section, provides further direct coupling.

5.4c Characteristics

Threshold currents of the integrated phase-locked laser array are ~ 300 mA, with the lowest being 200 mA. An output power of 210 mW (limited by the pulse generater) is obtained with 100 ns pulses. The lasers show single-lobe far field

patterns; beam divergence (FWHM) as narrow as 3-5 ° has been obtained (figure 5.14) up to 40% above threshold. However, the layer nonuniformity from liquid phase epitaxial growth results in differing stripe operating levels above threshold current. This leads to near field spots with nonuniform spot size (figure 5.15) giving rise to a far field divergence which is slightly wider than that expected from a 50 μm array.

With further optimization of growth and processing parameters, this structure should prove to be a valuable source of high power laser radiation in the long wavelength range suitable for optical communications.

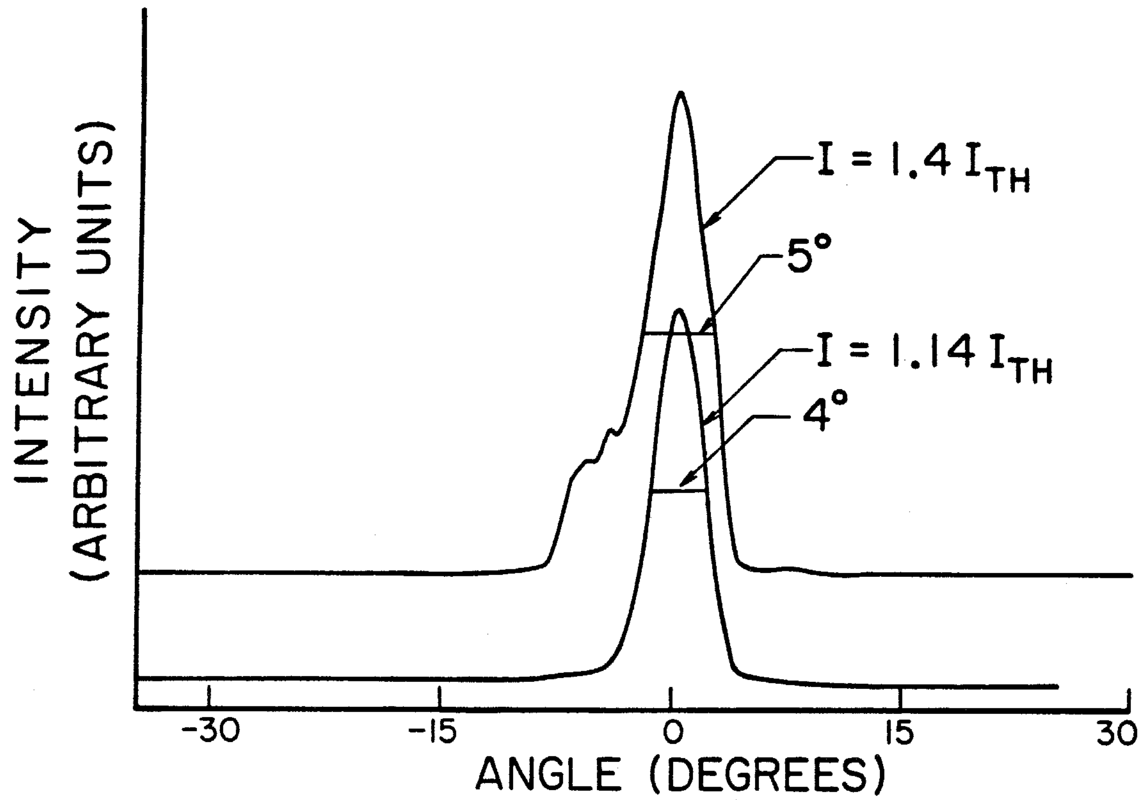

Fig. 5.14 Far field patterns of an integrated phase-array.

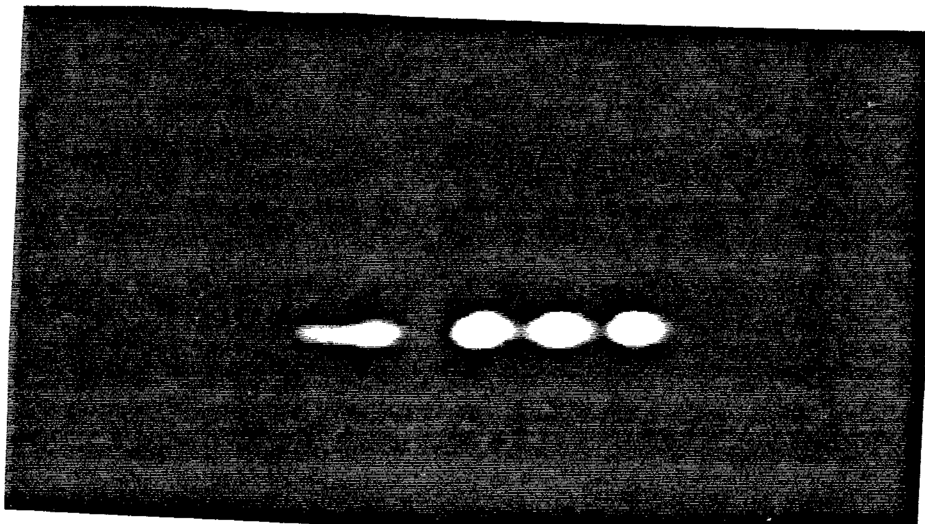

Fig. 5.15 Near field pattern of an integrated phase-array.

Appendix 5-1 : Diffraction coupling in laser array

For simplicity, we consider the configuration shown in figure 5.16, in which the individual laser stripe S_{i-1}, S_i, S_{i+1} etc. are coupled through diffraction. The mirror (at MM' plane) is replaced by an imaginary line, thus the diffracted beams appear to propagate continuously to the laser stripe on the opposite side. The phase change of individual beam upon reflection at MM' is neglected. The phase of the propagating Gaussian beam is given by [18] :

$$\Phi(z,y) = \beta z - \eta(z) + \frac{\beta r^2}{2R(z)} \tag{A-1}$$

where

$$r^2 = z^2 + y^2$$

$$\eta(z) = \tan^{-1}\left(\frac{z}{z_o}\right) \tag{A-2}$$

$$R(z) = z\left[1 + \left(\frac{z}{z_o}\right)^2\right]$$

$$z_o = \frac{\beta\omega^2}{2}$$

z_o is the confocal parameter of the beam, ω_o is minimum spot size and β is the propagation constant.

Approximating the average phase of the beam arriving at a stripe by the phase value at the middle of the stripe, the phase of the beam which couples laser stripe S_i to itself is :

$$\Phi_S = \Phi(z=2L, y=0) = 2\beta L - \tan^{-1}\left(\frac{2L}{z_o}\right) \tag{A-3}$$

Similarly the phase of the beam which couples stripe S_i to S_{i-1} or S_{i+1} is :

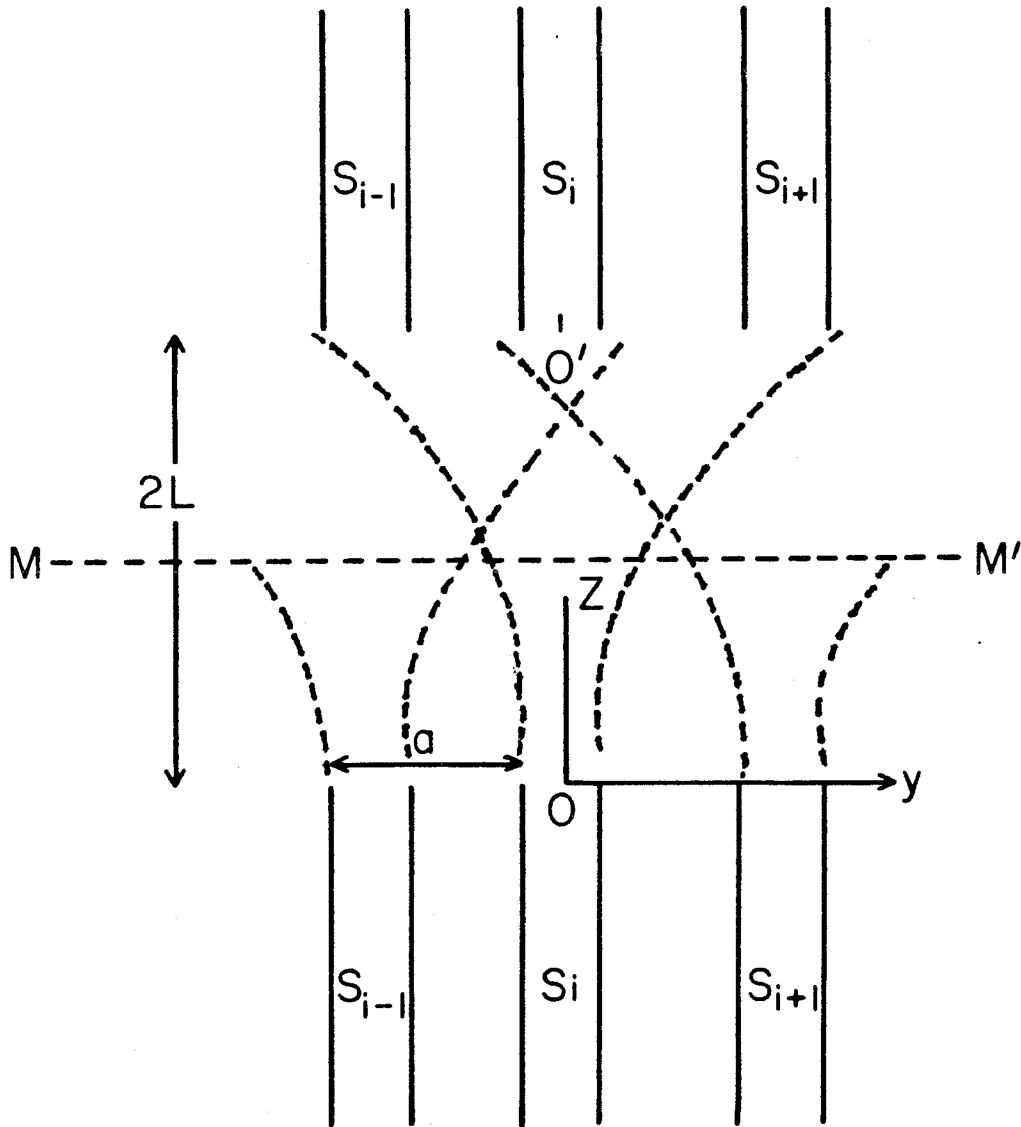

Fig. 5.16 A diagram showing a laser array coupled to itself and to adjacent stripes through diffraction and mirror (MM') reflection.

$$\Phi_A = \Phi(z=\sqrt{4L^2 + a^2}, y=a) \tag{A-4}$$

Consider the phase difference

$$\Delta\Phi = \Phi_A - \Phi_S \tag{A-5}$$

For constructive interference, $\Delta\Phi=2\pi m_1$ where m_1 is an integer. For $\Delta\Phi=2\pi(2m_1+1)$, destructive interference between neighboring beams occurs thus the array will not lase in this mode. Consider the case where $L>>a$ (see figure 5.16), then equation A-5 becomes :

$$\Delta\Phi \approx \frac{\zeta\beta a^2}{4L} \tag{A-6}$$

where

$$\zeta = 1 + \frac{1}{\left[1 + \frac{a^2}{8L^2}\right]\left[1 + \frac{z_o^2}{4L^2 + a^2}\right]} \tag{2}$$

Note that $1 \leq \zeta \leq 2$ and for $\left(\frac{z_o}{2L}\right) << 1$, we have :

$$\zeta \approx 2 - \frac{a^2}{8L^2}$$

and for $\left(\frac{z_o}{2L}\right) >> 1$, we have :

$$\zeta \approx 1 + \left(\frac{2L}{z_o}\right)^2$$

Substituting $\beta = \frac{2\pi n_{eff}}{\lambda}$ into equation A-6, we get equation 1. In addition to the phase matching condition $\Delta\Phi=2\pi m_1$, the oscillation condition of each laser must also be satisfied (i.e. $\frac{2L_1 n_{eff}}{\lambda} = m_2$, m_2 is an integer and L_1 is the total length of the laser).

References

1. A. Yariv, "Active Integrated Optics," in Proc. of 1971 Esfahan Conference on Pure and Applied Physics. Cambridge, MA. MIT Press (1972).

2. I. Samid, C. P. Lee, A. Gover, and A. Yariv, Appl. Phys. Lett., vol 27, pp. 405-407 (1975).

3. C. P. Lee, S. Margalit, A. Yariv, Appl. Phy. Lett., vol 31, pp. 281-282 (1977).

4. C. P. Lee, S. Margalit, I. Ury, A. Yariv, Appl. Phy. Lett., vol 32, pp. 410-412 (1978).

5. N. Bar-Chaim, J. Katz, I. Ury, and A. Yariv, Elect. Lett., vol. 17, pp. 108-109 (1981).

6. U. Koren, S. Margalit, T. R. Chen, K. L. Yu, A. Yariv, N. Bar-chaim, K. Lau, I. Ury, IEEE, J. Quant. Electron., QE-18, pp. 1653-1662 (1982).

7. U. Koren, K. L. Yu, T. R. Chen, N. Bar-Chaim, S. Margalit, and A. Yariv, Appl. Phys. Lett., vol 40, pp. 643-645 (1982).

8. J. L. Merz, R. A. Logan, Appl. Phys. Lett., vol 30, pp. 530-533 (1977).

9. W. Ng, H. W. Yen, A. Katzir, I. Samid, and A. Yariv, Appl. Phys. Lett., vol 29, pp. 684-686 (1976).

10. H. Blauvelt, N. Bar-Chaim, D. Fekete, S. Margalit, and A. Yariv, Appl. Phys. Lett., vol 40, pp. 289-290 (1982).

11. U. Koren, A. Hasson, K. L. Yu, T. R. Chen, S. Margalit, A. Yariv, Appl. Phys. Lett., vol 41, pp. 791-793 (1982).

12. J. W. Crowe, and W. E. Ahearn, IEEE J. Quantum Electron., QE-15, pp 169-172 (1968).

13. J. E. Ripper and T. L Paoli, Appl. Phys. Lett., vol 17, pp 371-373 (1970).

14. D. R. Scifres, R. D. Burnham, and W. Streifer, Appl. Phys. Lett., vol 33, pp 1015-1017 (1978)

15. D. R. Scifres, R. D. Burnham, and W. Streifer, Appl. Phys. Lett., vol 41, pp 118-120 (1982)

16. T. R. Chen, K. L. Yu, B. Chang, A. Hasson, S. Margalit and A. Yariv, To be published in Appl. Phys. Lett.

17. J. Katz, S. Margalit, and A. Yariv, Appl. Phys. Lett., vol 42, pp 554-556 (1982).

18. A. Yariv, "Quantum Electronics" 2nd Edition, Chapter 6, John Wiley and Sons Inc., New York, (1975).

Chapter 6

Short Cavity InGaAsP/InP Lasers

6.1 Introduction

For some applications of semiconductor laser diodes, it is desirable to have lasers operate in a single longitudinal mode. However, for most laser structures with the usual cavity length (200-300 μm), it is observed that single longitudinal mode operation is difficult to achieve, and can be maintained only over a limited temperature and injection current range.

A promising scheme to achieve single mode operation is to make use of the fact that the cavity mode spacing depends inversely on the cavity length. By micro-cleaving the lasers into short-length cavities, spacing between neighboring longitudinal modes is widened thus reducing the number of modes which can oscillate within a given gain profile.

6.2 Longitudinal mode selection

As Fabry-Perot cavity modes are considered, we have the resonance condition [1]:

$$\lambda_m = \frac{2Ln_{eff}(\lambda)}{m} \tag{1}$$

where L is the cavity length, m is the mode number, n_{eff} is the effective refractive index for the guided mode within the laser resonator. The mode separation is found from equation 1 :

$$\delta\lambda = \frac{\lambda}{2L(\frac{n_{eff}}{\lambda} - \frac{d}{d\lambda}n_{eff})} = \frac{\lambda}{2Ln_g} \tag{2}$$

where n_g is the group index of the cavity modes. From equations 2 it is

observed that as the cavity length is reduced, the mode spacing between the central mode and its adjacent modes increases leading to an increasing gain difference between them. This results in mode selection and is verified in micro-cleaved short cavity lasers [2]. Figures 6.1, 6.2 show the spectra of two quaternary Groove Lasers differing only in cavity length. For 85 μm cavity length laser, predominant single longitudinal mode is observed at low current injection ($J=1.31J_{TH}$). As the injection level increases, mode hopping can occur. At $J=J_{TH}$, the modes adjacent to the central one also lase, and lasing wavelength is right-shifted 20 Å. At still higher injection ($J=2.7J_{TH}$) more longitudinal modes occur. However, with 33 μm cavity length laser, single longitudinal mode operation can be maintained at the same wavelength up to high current injection levels, as illustrated in figure 6.2 The mode spacing for the 85 μm length laser is about 20 Å, while it is about 50 Å for the 33 μm length laser, in agreement with calculated values (equation 2).

6.3 High frequency designs

These short cavity length lasers can be modulated with frequency higher than that achievable with conventionally cleaved (200-300 μm cavity length) lasers. It has been demonstrated [3] that GaAs short cavity lasers (100-120 μm) can be modulated up to 6-8 Ghz. This high frequency behavior is examined here. The electron and photon density are described by the following wave equations:

$$\frac{dn}{dt} = \frac{J}{qd} - A(n - n_{om})S - \frac{n}{\tau_s} \tag{3}$$

$$\frac{dS}{dt} = \Gamma A(n - n_{om})S - \frac{S}{\tau_p} \tag{4}$$

where n,S denote electron and photon density respectively, q is a unit electron charge, d is the active layer thickness, J is the pumping current, A is the gain

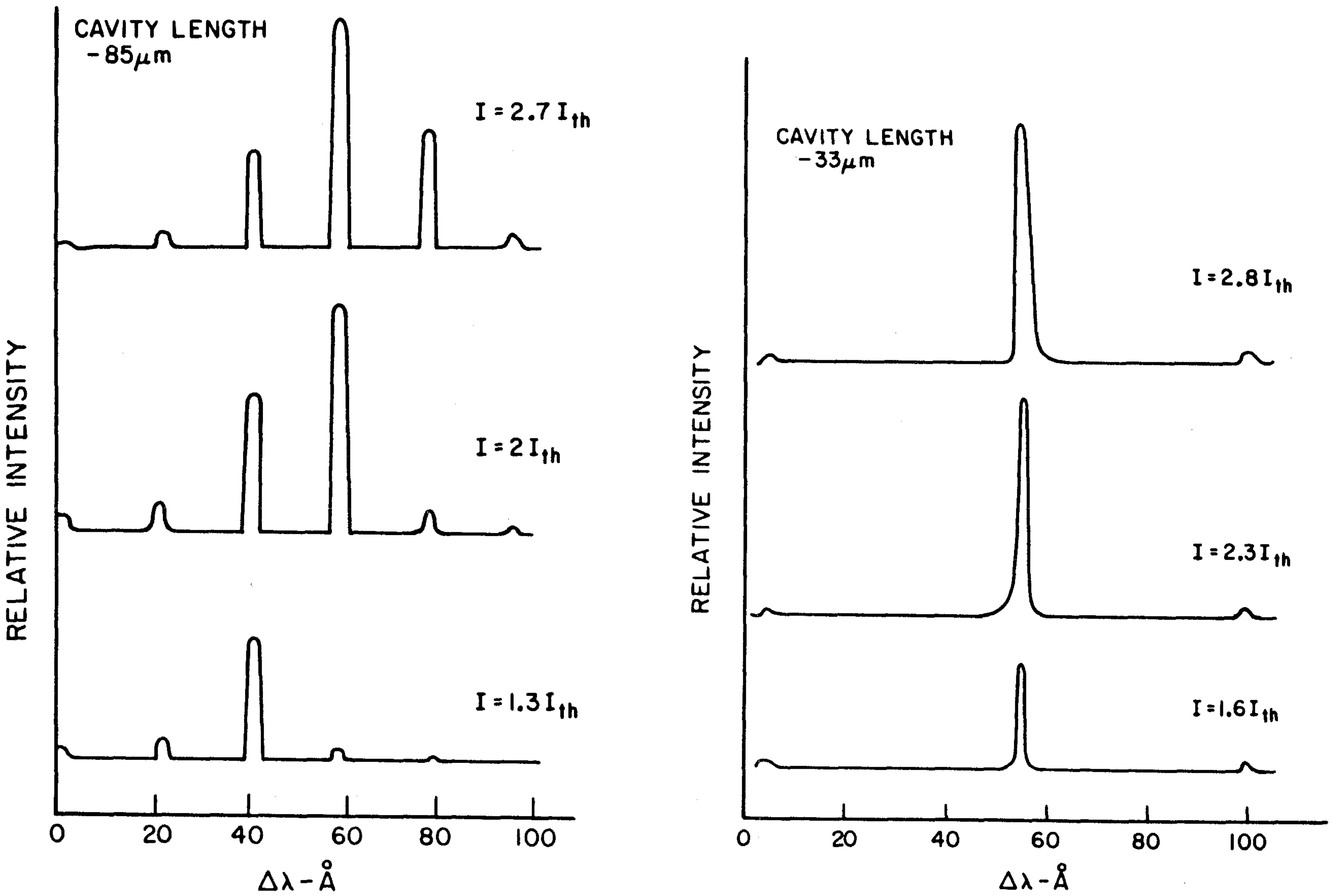

Fig. 6.1 Spectral behavior of a 85 μm cavity length laser with uncoated mirrors.

Fig. 6.2 Spectral behavior of a 33 μm cavity length laser with uncoated mirrors.

coefficient, Γ is the optical mode confinement factor, τ_s, τ_p are the electron and photon lifetimes respectively. In equation 3, for simplicity, electrical pumping is assumed to be homogeneous across the laser stripe and the effect of lateral carrier diffusion is neglected. Similarly, spontaneous emission is neglected in equation 4.

The photon lifetime τ_p can be expressed as:

$$\frac{1}{\tau_p} = \frac{c}{n_{eff}}(\alpha + \frac{1}{L}\ln(\frac{1}{R})) \tag{5}$$

where α is the total internal loss per unit cavity length. L is the cavity length. $R = \sqrt{R_1 R_2}$ with R_1, R_2 the end mirror reflectivities.

Performing a small signal analysis of equations 3,4 (see Appendix 6-1) with n, S varies harmonically about their steady state values n_o, S_o, the following expression is obtained which describes the relaxation oscillation (or corner) frequency [4] of the system:

$$f_c = 2\pi[(\frac{1}{\tau_p} + \Gamma A n_{om})\frac{1}{\tau_s}(\frac{J}{J_{th}} - 1) - \zeta^2]^{\frac{1}{2}} \tag{6}$$

where

$$\zeta = \frac{1}{2}(AS_o + \frac{1}{\tau_s}) \tag{7}$$

f_c represents the maximum modulation frequency of the lasers and (see equation 6) it increases with $1/\tau_p$, Γ,J/J_{th}. As J/J_{th} or $1/\tau_p$ also increases, the rate of change of the carrier density about the n_o increases. Similarly, a larger Γ enhances the small-signal rate of change of the photon density about its steady state value.

It is expected that by increasing J/J_{th}, f_c can be increased. However, J cannot be too high as electrical heating can lead to a rise of device temperature (espe-

cially during CW operation) which can degrade the laser performance. The total thermal power dissipated P_{diss} in a laser diode can be expressed as:

$$P_{diss} = (\frac{h\nu}{q} + iR_s)i - \frac{h\nu}{q}\eta(i - i_{th}) \tag{8}$$

with η the external differential quantum efficiency expressed as

$$\eta = \frac{\frac{1}{2L}\ln(\frac{1}{R})}{\alpha + \frac{1}{2L}\ln(\frac{1}{R})} \tag{9}$$

where in equation 8, i is the laser current, i_{th} is the threshold current, i^2R_s is the ohmic power dissipated by the laser diode equivalent resistance R_s, $\frac{h\nu}{q}$ denotes the total thermal power from recombination processes in the active layer ($h\nu$ is the photon energy). The last term in equation 8 denotes the exclusion of the stimulated optical output power from the total power. For simplicity, the small optical power due to spontaneous emission is neglected. Large Γ values lead to higher frequency operation. Also, by decreasing L, the photon lifetime shortens and could lead to a higher f_c. However, this lifetime shortening would also lead to an increase in J_{th} where (see Appendix 6-1)

$$J_{th} = \frac{qd}{\tau_s}(\frac{1}{\Gamma\tau_p A} + n_{om}) \tag{12}$$

Thus these two have opposite effects on f_c. Figure 6.3 shows the calculated f_c for the Groove Laser as a function of cavity length L, at different injection levels (J/J_{th}). In the calculation, n_{om} takes the value of $1.2\times10^{18}cm^{-3}$, α is taken as 15 cm^{-1}, τ_s is 6 nsec, Γ is 1.7 and A is $3.5\times10^{-6}cm^2sec^{-1}$. The active region is assumed to be 0.2 μm thick and has an effective width of 15 μm and a mirror reflectivity of 0.3. The resistance of a 300 μm cavity length laser is taken to be 5 Ω. The curves of constant P_{diss} per unit cross sectional area are also plotted in this figure.

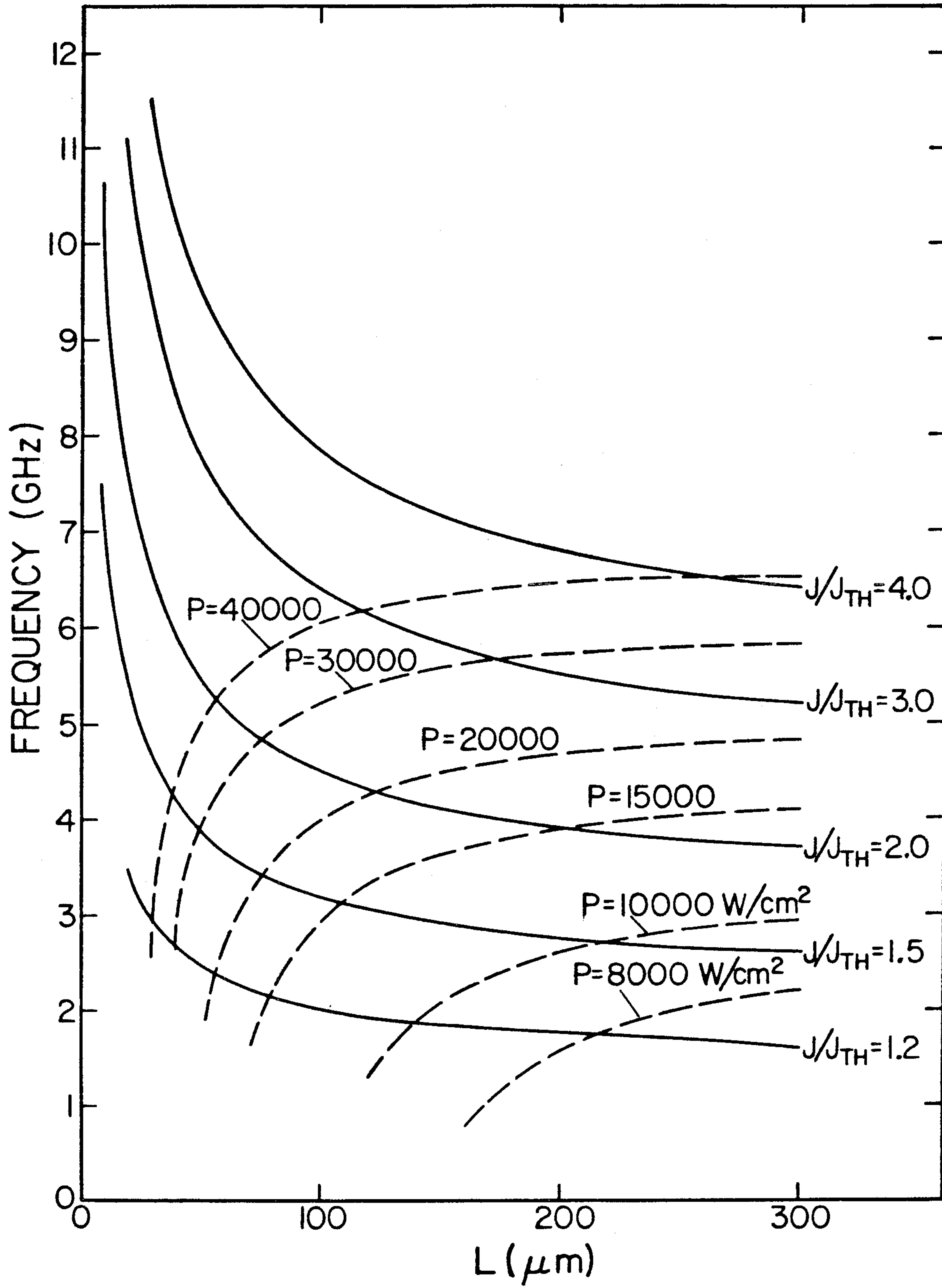

Fig. 6.3 Calculated maximum modulation frequency of a Groove Laser.

6.4 Short cavity lasers with coated mirrors

The threshold current density can be reduced, as shown in equation 12, by increasing the mirror reflectivity. Thus very low threshold current is possible with short lasers, if the mirror reflectivity can be adjusted to compensate length reduction effect on the threshold current density. In figure 6.4, the threshold current density based on equation 13 is plotted against the cavity length for R ranged from 0.2 to 0.95. It is seen that as R approaches 1, a wider cavity length range exists for low J_{th}. This is experimentally verified with the micro-cleaved Groove Lasers having end mirrors coated with alternating amorphous SiO_2 and Si layers. These layers are a quarter wavelength thick except the last one which is one eighth of a wavelength thick. The SiO_2 is deposited from a fused silica source and Si is evaporated from a high purity crystalline silicon source. 6-layer coating has a reflectivity of 80 % for 1.3 μm wavelength light while 8-layer coating has a reflectivity greater than 90 %. For a 38 μm long laser with 80 % reflectivity front mirror and high reflectivity (> 90%) rear mirror, the threshold current is 3.8 mA (figure 6.5) while the threshold of the same laser without dielectric coating is 22 mA. The lowest threshold current achieved is 2.9 mA with a laser coated with 10 layers at the front mirror and 14 layers at the rear mirror. The emission spectra of a 37 μm cavity length groove laser with coated mirrors is shown in figure 6.6. Single longitudinal mode operation is maintained up to 6 times threshold current without any noticeable secondary modes.

6.5 Conclusion

Microcleaved short cavity lasers can be easily operated in a stable longitudinal mode and are capable of high frequency. By coating the mirrors, low threshold current can be obained.

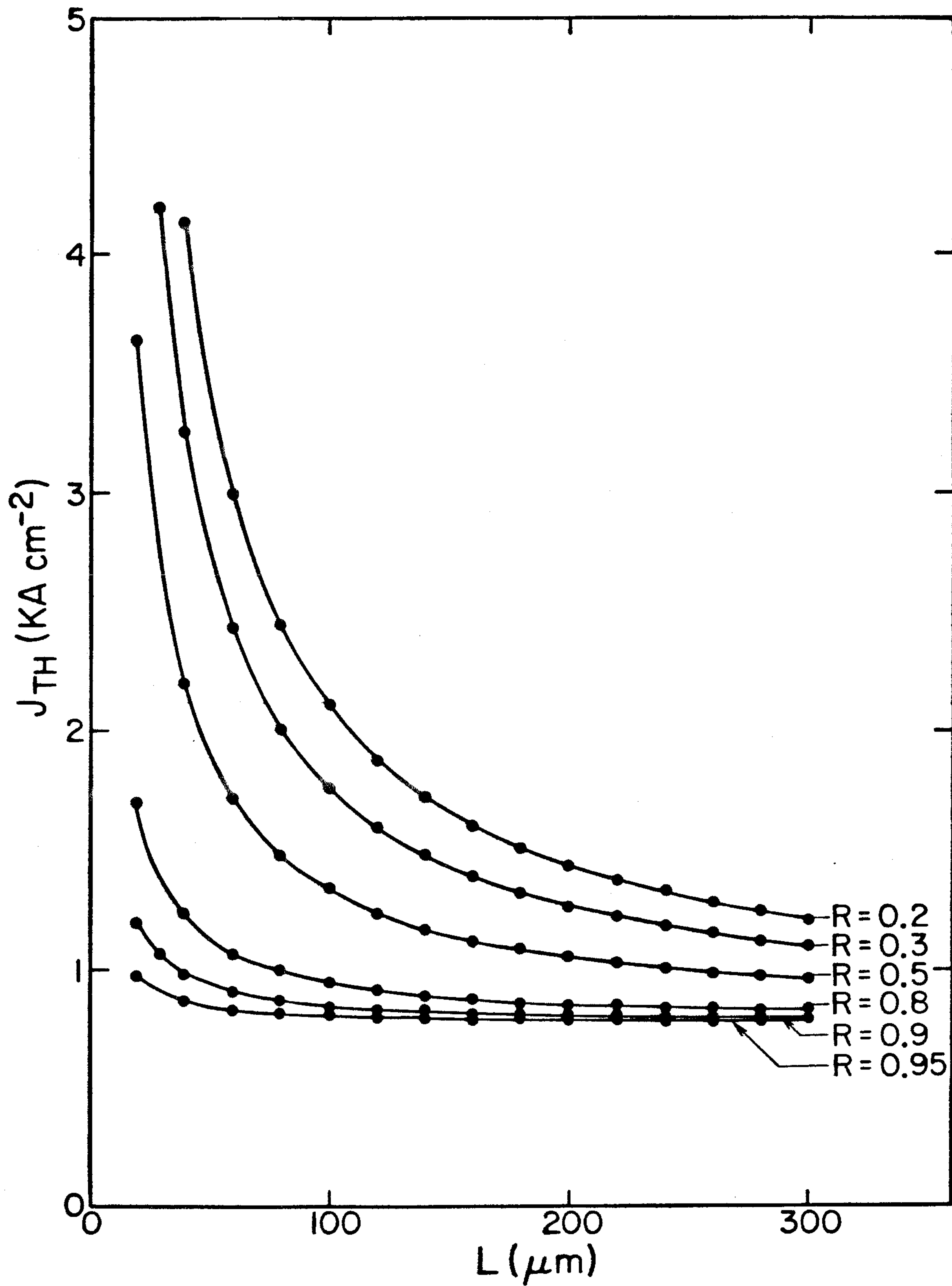

Fig. 6.4 Calculated threshold current density versus laser cavity length at different mirror reflectivities.

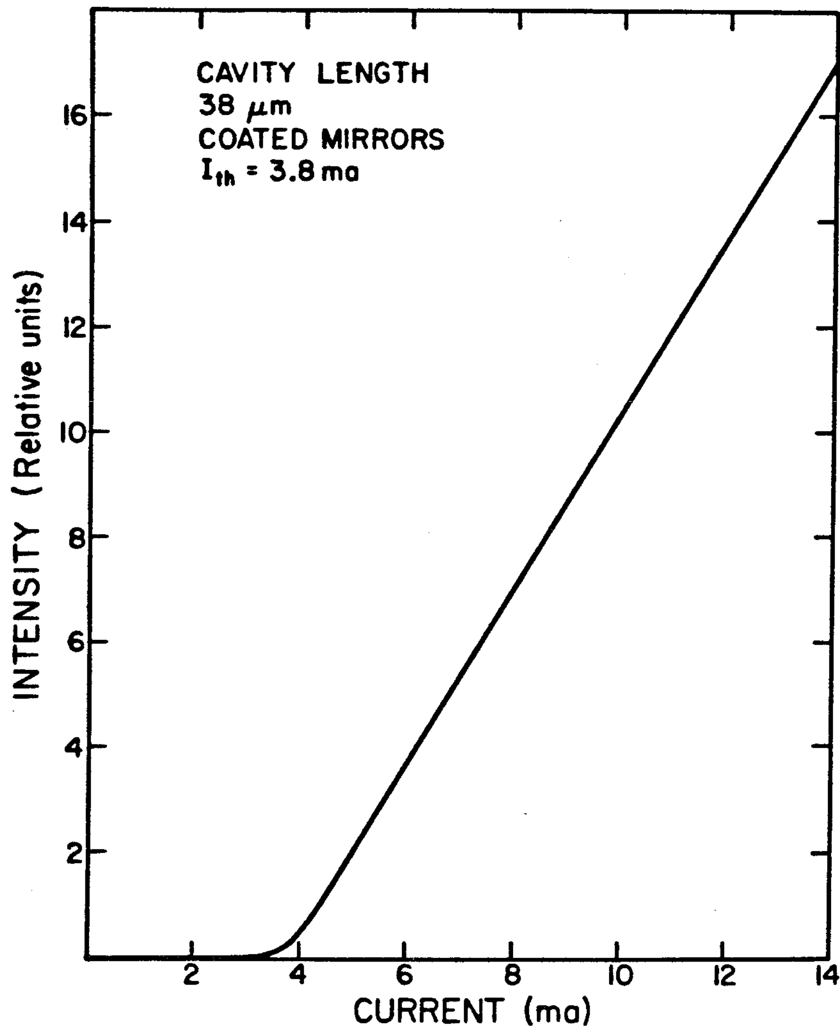

Fig. 6.5 L-I characteristics of a 38 μm long laser with coated mirrors. The same laser with uncoated mirror has a threshold current of 22 mA.

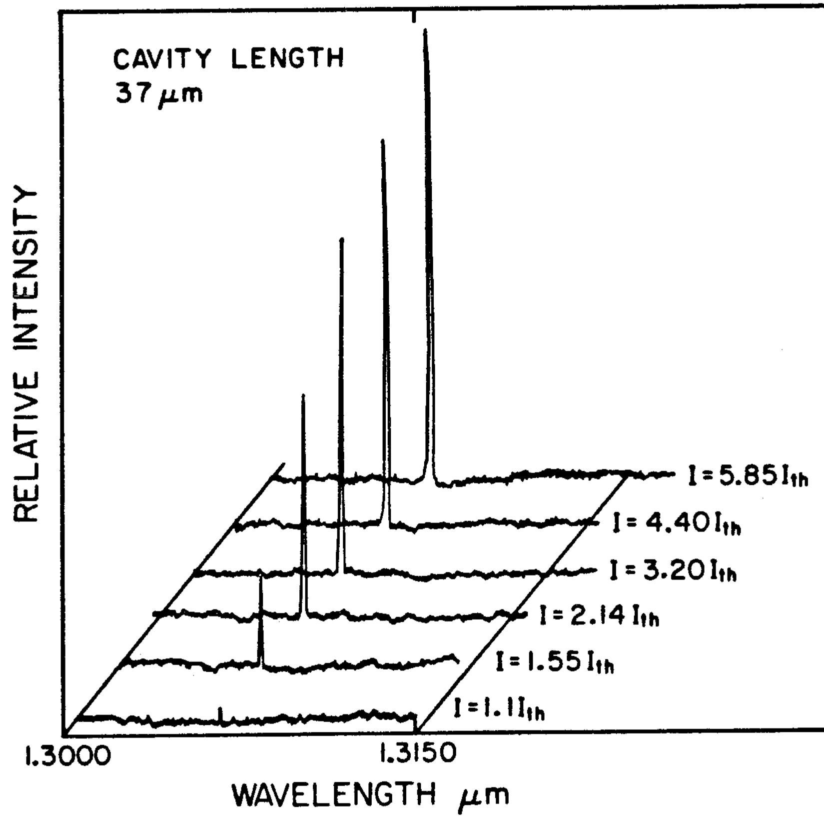

Fig. 6.6 Spectral behavior of a 37 μm cavity length laser with coated mirrors.

Appendix 6-1 : Small signal analysis of rate equations

The rate equations describing the electron and photon density are:

$$\frac{dn}{dt} = \frac{J}{qd} - A(n - n_{om})S - \frac{n}{\tau_s} \tag{3}$$

$$\frac{dS}{dt} = \Gamma A(n - n_{om})S - \frac{S}{\tau_p} \tag{4}$$

For steady state, $\frac{\partial n}{\partial t} = \frac{\partial S}{\partial t} = 0$, thus $n=\bar{n}$ and $S=\bar{S}$, the steady state values. As gain is clamped over threshold, $\bar{n} = n_{TH}$ after threshold is reached. Therefore, for $S \geq 0$, equation 4 becomes :

$$\Gamma A n_{TH} = \frac{1}{\tau_p} + \Gamma A n_{om} \tag{A-1}$$

this is substituted in the steady state version of equation 3 to give the threshold condition

$$J_{th} = \frac{qd}{\tau_s}\left(\frac{1}{\Gamma \tau_p A} + n_{om}\right) \tag{A-2}$$

which is equation 12.

For modulation purpose, we perform a small signal harmonic perturbation of n and S about their steady state values, then equations 3,4 give:

$$\frac{\partial \Delta n}{\partial t} = -A\Delta n\bar{S} - A(\bar{n} - n_{om})\Delta S - \frac{\Delta \bar{n}}{\tau_s} \tag{A-3}$$

$$\frac{\partial \Delta S}{\partial t} = \Gamma A \Delta n \bar{S} \tag{A-4}$$

To determine the natural oscillation frequency (thus relaxation frequency) of this coupled system, we let

$$\Delta n \sim \Delta n_o e^{\alpha t}$$

$$\Delta S \sim \Delta S_o e^{\alpha t}$$

then we obtain

$$\alpha = -\zeta \pm i\sqrt{A^2(\bar{n} - n_{om})\bar{S}\Gamma - \zeta^2} \tag{A-5}$$

where ζ is given in equation 7. The real part of α gives the natural damping while the imaginary part determines the relaxation oscillation frequency :

$$f_c = 2\pi(\Gamma A^2(\bar{n} - n_{om})\bar{S} - \zeta^2)^{\frac{1}{2}} \tag{A-6}$$

then equation 6 results (upon substituting equation A-2 into the steady state version of equation 3 to solve for $A(n - n_{om})\bar{S}$).

References

1. A. Yariv, "Quantum Electronics", second edition, Chapter 6, John Wiley and Sons Inc., New York, (1975).

2. U. Koren, Z. Rov-Noy, A. Hasson, T. R. Chen, K. L. Yu, L. C. Chiu, S. Margalit and A. Yariv, to be published in Appl. Phys. Lett., 1983.

3. K. Lau, N. Bar-Chaim, I. Ury, Ch. Harder and A. Yariv, to be published in Appl. Phys. Lett.

4. H. Y. Kressel, J. K. Butler, "Semiconductor Lasers and Heterojunction LEDs," Academic Press, New York (1977).